Università degli Studi di Padova

DIPARTIMENTO DI FISICA E ASTRONOMIA

Corso di Laurea Magistrale in Fisica

Investigation of principal reactive pathways in CO_2 plasmas by numerical techniques

Laureando:
Luca Vialetto
Matricola 1127895

Relatore:
Dr. Gianluigi Serianni

Correlatore:
Prof. Dr. Ing. Ursel Fantz
Dr. Emile Carbone

Controrelatore:
Dr. Mosè Mariotti

Anno Accademico 2016–2017

Abstract

The emission of carbon dioxide is one of the main current environmental challenges due to its impact on the climate. Additionally, the intermittent character of renewable energy sources imposes a need of *energy storage*. The main idea to tackle these problems is to convert temporary electrical energy surplus into chemical fuels that are advantageous in terms of high energy density. In this framework, at IPP-Garching, a new group called *Plasma for Gas conversion* (P4G) has started in February 2017 with the aim of studying the possibility of converting CO_2 into chemicals fuels that can be easily transported and stored using the current distribution systems. Central in the approach is the use of a plasma to store energy in chemical bonds and enhance the overall conversion. Progress in the understanding the underlying physics and chemistry can only be done by significant support from modelling and simulations.

The study presented in this thesis has been performed in IPP-Garching during the summer semester period of the academic year 2016-2017, in the framework of the Erasmus+ exchange between University of Padova and Ludwig-Maximilians-Universität of Munich.

In *Chapter 1* a brief introduction about CO_2 conversion is presented. Particular focus will be dedicated on the utilization of a plasma as a medium to ease chemical reactions. An overview of both physical and technological aspects is introduced.

Chapter 2 provides an overview on plasma chemistry global models explaining both physical assumptions and numerical implementation in the software PLASIMO.

The rich chemistry implemented in a CO_2 model leads to difficulties both in the interpretation of data and in the computational load. For this reason, two parts are presented in this thesis. The first one deals with studying a simplified version of a 0-D CO_2 kinetic model, while the second part present an analysis and characterization of numerical reduction techniques useful to reduce the chemistry and reactions considered.

In *Chapter 3* the role of neutral heavy particle interactions in the CO_2 dynamics are studied. Some hints about thermal quenching are highlighted in order to improve the conversion efficiency. Moreover, a study of oxygen dynamics is presented by comparing the oxygen chemistry present in the CO_2 model with a state-of-the art complete oxygen model. Some hints on carbon chemistry are also presented.

In *Chapter 4* an analysis of a CO_2 kinetic model is given. A simplified CO_2 kinetic model, in which excited levels are neglected, is studied by means of steady-state calculations with fixed electron density and temperature. This Chapter presents also results from pulsed calculations that aim on highlighting the principal pathways in both high power density and low power density regime. In conclusion, the effect of adding electronically and vibrationally excited states is highlighted.

The implementation of a numerical reduction method called Principal Component Analysis on plasma chemistry models is the focus of the second part of the thesis. Starting from benchmarking results from literature, the final aim was to compare linear and nonlinear methods that are useful to handle the intrinsic complexity of plasma chemistry systems. Results of these methods and suggestions for future improvements are given in *Chapter 5* and *6*.

In the *Conclusion* the main results are summarized together with possible future improvements and experimental techniques useful to benchmark the model.

Sommario

L'emissione di anidride carbonica è una delle principali sfide ambientali attuali per l'impatto sul clima. In aggiunta, l'intermittente disponibilità di energia da risorse rinnovabili impone il bisogno di un deposito di energia. La principale idea per affrontare questi problemi è di convertire l'intermittente energia elettrica prodotta in surplus in combustibile chimico che è vantaggioso dal punto di vista di un'elevata densità di energia. In questo contesto, presso IPP-Garching, un nuovo gruppo chiamato *Plasma for Gas conversion* (P4G) ha iniziato l'attività di ricerca da Febbraio 2017 con lo scopo di studiare la possibilità di convertire CO_2 in combustibile chimico che può essere facilmente trasportato e immagazzinato usando l'attuale sistema di distribuzione. Fondamentale in questo approccio è l'utilizzo di un plasma per immagazzinare energia in legami chimici e aumentare la conversione totale. Un progresso nella comprensione della fisica e chimica in questi processi può essere fatto solo tramite un significativo contributo da attività modellistiche e simulazioni.

Lo studio presente in questa tesi è stato effettuato a IPP-Garching durante il secondo semestre dell'anno accademico 2016-2017, nel contesto dello scambio Erasums+ tra l'Università di Padova e la Ludwig-Maximilians-Universität di Monaco di Baviera.

Nel *Capitolo 1* è presentata una breve introduzione riguardo la conversione di CO_2. Particolare attenzione verrà dedicata all'utilizzo di un plasma come mezzo per incrementare le reazioni chimiche. È presentato inoltre una panoramica su aspetti fisici e tecnologici.

Nel *Capitolo 2* è presentata una descrizione riguardo modelli globali in chimica del plasma con particolare attenzione su assunzioni fisiche e implementazione numerica nel software PLASIMO.

La ricca chimica implementata nel modello di CO_2 porta a difficoltà sia per l'interpretazione dei dati che per il costo computazionale. Per questa ragione, due parti sono presentate in questa tesi. La prima riguarda lo studio di una versione semplificata di modello cinetico 0-D di CO_2, mentre la seconda parte presenta un'analisi e caratterizzazione di tecniche numeriche utili per la riduzione della chimica e reazioni considerate.

Nel *Capitolo 3* è studiato il ruolo delle interazioni tra specie neutre nella dinamica di CO_2. È sottolineata, inoltre, l'importanza di processi termici per incrementare l'efficienza di conversione. In aggiunta, uno studio sulla dinamica dell'ossigeno è presentata tramite il confronto tra la chimica dell'ossigeno presente nel modello di CO_2 e quella presente in un modello completo di ossigeno. Sono presentati, inoltre, spunti riguardo la chimica del carbonio.

Nel *Capitolo 4* è presente un'analisi riguardo un modello cinetico di CO_2. Inizialmente è stato studiato un modello cinetico semplificato di CO_2, in cui i livelli eccitati sono stati trascurati, tramite calcoli steady-state in cui sono fissate densità e temperatura elettronica. Questo capitolo presenta inoltre risultati riguardo calcoli per plasmi modulati ad impulsi che hanno lo scopo di rivelare le reazioni principali sotto l'effetto di elevata o ridotta densità di potenza. Infine, è discusso l'effetto dell'aggiunta di livelli eccitati elettronici e vibrazionali.

L'obiettivo della seconda parte della tesi è l'implementazione di un metodo numerico di riduzione chiamato Analisi delle Componenti Principali applicato a modelli di chimica del plasma. Inizialmente è presentato un confronto con risultati noti in letteratura e in seguito è sviluppato un confronto tra metodi lineari e non-lineari che sono utili per affrontare la complessità intrinseca presente in sistemi di chimica del plasma. Nel *Capitolo 5* e 6 sono presentati i risultati di questi metodi e suggerimenti per sviluppi futuri.

Nelle *Conclusioni* sono riassunti i risultati principali, possibili miglioramenti futuri nel settore e a tecniche sperimentali utili per un benchmark del modello.

Contents

1 Introduction **1**
- 1.1 Production of CO_2 neutral fuels . . . 1
- 1.2 Power to Gas . . . 2
- 1.3 Why plasma? . . . 3
  - 1.3.1 Electrolysis and plasmolysis . . . 3
  - 1.3.2 Non-equilibrium nature of plasmas . . . 5
- 1.4 State of the art technology . . . 7

2 Description of the model **11**
- 2.1 Global model for plasma chemistry . . . 11
- 2.2 Numerical implementation . . . 17
- 2.3 Stepwise Approach . . . 20

I Principal pathways in CO_2 plasmas **23**

3 Test of the model **25**
- 3.1 Influence of heavy particle collisions . . . 25
  - 3.1.1 Comparison with thermodynamic model . . . 26
  - 3.1.2 CO loss fraction . . . 30
- 3.2 Hints on carbon chemistry . . . 32
- 3.3 Hints on oxygen chemistry . . . 33

4 Analysis of CO_2 kinetic model **43**
- 4.1 Steady-state calculations . . . 43
  - 4.1.1 Influence of electron density . . . 44
  - 4.1.2 Influence of electron temperature . . . 47
  - 4.1.3 Influence of gas temperature . . . 49
- 4.2 Pulsed Calculations . . . 50
  - 4.2.1 High power density . . . 52
  - 4.2.2 Low power density . . . 55
- 4.3 Influence of vibrational kinetics . . . 57

II Numerical Reduction Techniques **63**

5 Linear Principal Component Analysis **65**
5.1 Aim and assumptions 66
5.2 PCA on plasma chemistry 69
5.3 Characterisation of the method 75

6 Nonlinear Principal Component Analysis **79**
6.1 Nonlinear regression 80
6.1.1 Aim and assumptions 80
6.1.2 Application of the method 82
6.2 Kernel Principal Component Analysis 85
6.2.1 Aim and assumptions 86
6.2.2 Application of the method 90
6.3 Discussion and Next Steps 91

7 Conclusions **93**

CHAPTER 1

Introduction

A resource-efficient Europe is the flagship initiative of the Europe 2020 Strategy, with the CO_2 emissions control issue as its backbone activity [1] [2]. Within this framework, the main idea of this study is to investigate a novel approach that aims to convert biogas (i.e. CO_2 and CH_4) into chemicals and fuels. The fuel produced can be easily transported and stored using the current distribution systems. Central in the approach is the use of plasma to store energy in chemical bonds. This approach is compatible with the intermittency of the available sustainable energy sources. In addition, CO_2 recycling can be a possible contributor to a solution for reducing the anthropogenic emissions of greenhouse gases (GHG) into the atmosphere.

1.1 Production of CO_2 neutral fuels

To make the electricity generation *carbon neutral* and thereby holding back the carbon emissions, renewable energy systems (i.e. wind and solar) have the best potential because of their zero carbon emissions. However, a constant level of power production with wind and solar energy cannot be achieved due to *temporal* and *spatial* mismatch between production and demand. The main actual disadvantage is that these fluctuations of the power generation by renewable energy sources demand both high-capacity distribution systems as well as intermittent source possibilities. On the other hand, renewable energy production may be located in areas with limited transport capacities. In this framework, a different approach is needed that provides a sustainable system which can be integrated in the actual existing grid system. According to [3], three important requirements have to be fulfilled for the choice of the optimal technology:

- High storage capacity.
- High storage efficiency.
- Flexible site-specific modifiability.

Pumped hydro storage, for example, provides high storage energy efficiency (i.e. around $70\% - 80\%$) but limited storage capacities which will be not suitable for higher share of renewable energy. On the contrary, all these three parameters are well covered by *chemical storage*. Within this category, a *Power to Gas* scheme (P2G) has been developed [3] that aims to split feedstock CO_2 and H_2O into synthesis gas, a mixture of CO and H_2. This method is described in the following Section.

1.2 Power to Gas

The main idea of *Power to Gas* scheme (P2G) is to introduce renewable energy into the existing chemical energy infrastructure by synthesis of chemicals from CO_2 that are easy to transport and store. The basic starting process is the CO_2 splitting that can be described by process (1.1):

$$\mathbf{CO_2} \rightarrow \mathbf{CO} + \frac{1}{2}\mathbf{O_2} \tag{1.1}$$

In this category, another process has to be mentioned that is the so called *dry reforming* of methane. This process (1.2) utilises CO_2 and CH_4 to produce syngas (i.e. a mixture of H_2 and CO) that can then be converted into methanol.

$$\mathbf{CO_2} + \mathbf{CH_4} \rightarrow 2\mathbf{CO} + 2\mathbf{H_2} \tag{1.2}$$

The main advantages of this last process is the production of high purity syngas and the fact that the reaction consumes two different types of GHG. However, current studies are ongoing to tackle the principal limitations due to the presence of a sustinable catalyst and the higher temperatures required. Moreover, one of the obstacles for utilizing CO_2 as feedstock to industrial processes is that CO_2 is a highly stable molecule. Consequently, a substantial input of energy and often catalysts are necessary for its chemical conversion. Studies to optimize the CO_2 conversion are ongoing and this will be the main topic of the present thesis. The schematization of P2G method can be seen in Fig.(1.1). The necessary CO_2 can be derived from exhaust or process gases of industrial production processes or fossil power plants. The splitted CO_2 (and H_2O) synthesize to methane. The produced methane is called *synthetic gas* (i.e. syngas) and plays a central role in the production of hydrocarbons, including methanol, diesel and dimethyl ether. CO_2 neutral fuel cycle is established by powering the conversion step by renewable energy and recapture CO_2 emitted after combustion. Thus, the overall process described includes two steps: a first *P2G scheme* that converts and stores excess electricity by wind/solar into hydrocarbon based fuels and a second step called *Carbon Capture and Utilization* (CCU) that aims to recapture and reuse the CO_2 emitted by burning these fuels.

According to [5], an important advantage of the P2G−CCU scheme is the use of existing infrastructures for gas and oil storage, transport and distribution, whilst mobility technology remains hydro-carbon fuel based. However, the critical step in this scheme is the conversion of feedstock CO_2 and H_2O into syngas, which forms the starting point of chemical processing to obtain methane (Sabatier) or diesel (Fischer-Tropsch).

On the technological point of view, two different methods can be differentiated depending on the conversion process of feedstock H_2O and CO_2 into fuel [6]:

- *Direct Conversion:* It converts solar photons directly into fuel. Examples of that process is photo-chemical and thermo-chemical conversion.

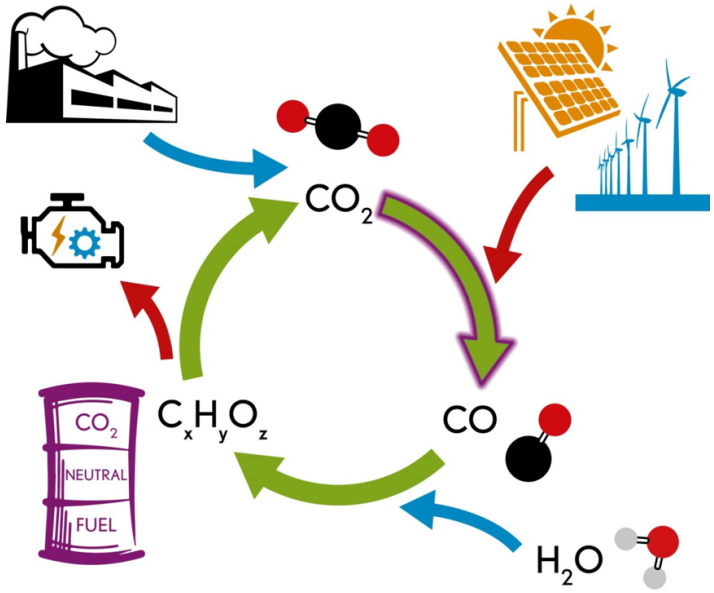

Figure 1.1: ***Schematization of Power-to-Gas (P2G) and Carbon Capture and Utilization (CCU), from [4].***

- *Indirect Conversion:* Conversion step is done indirectly indirectly through the intermediate of electricity. Example of this method are electrolysis and plasmolysis.

Because the energy efficiency is at least one order of magnitude higher (i.e. around $18-20\%$ for the overall process) with respect to the direct methods, this study will focus on *indirect methods* that are presented in the next Section.

1.3 Why plasma?

In this section, the two main methods of *indirect conversion* will be presented (i.e. electrolysis and plasmolysis). According to this scenario, it will be seen that plasma sources have a great potential mainly due to the strong non-equilibrium conditions that may lead to higher energy efficiencies compared to thermal processes.

1.3.1 Electrolysis and plasmolysis

Electrolysis This method is based on the electro-chemical conversion of CO_2. In this mode, gaseous oxides such as steam and carbon dioxide are supplied to one electrode and a voltage is applied across the cell. This technique drives the electrolysis of the CO_2 by removal of an oxygen atom, which is transported as an oxide ion across the electrolyte to the other electrode where the oxide ions recombine to produce gaseous oxygen [7]. The diagram of a Solid Oxide Electrolizer Cell (i.e. SOEC) is shown in Fig.(1.2) where the net process (1.3) produces CO that can be reformed into other fuels such as methane or liquid hydrocarbons.

$$\mathbf{2CO_2 + electricity \rightarrow 2CO + O_2} \tag{1.3}$$

According to [5], even if the energy density of a SOEC is high (1 A/cm^2 at 1.5 V), it operates at relatively high temperatures (i.e. $700-800$ °C), which is not well suited to fast switching because of thermal mechanical stress and corrosion at molecular interface layers.

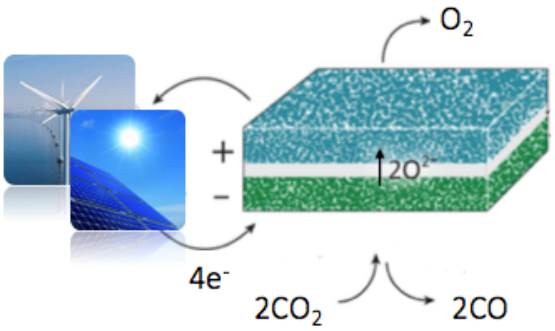

Figure 1.2: ***A scheme of a Solid Oxide Electrolyzer Cell, from [7].***

Plasmolysis The main idea of plasma chemical conversion (or *plasmolysis*) is to use a plasma to ease CO_2 splitting. The main advantages of using plasmas with respect to electrolysis can be summarized in the following:

- High power density is applied in order to produce an high concentration of chemically active species (i.e. ions, excited species, radicals, etc.) that permit to intensify chemical processes.
- High gas flow rates allow upscaling to high CO production rates at MW level, moreover the reactor is compact and does not employ scarce materials.
- Plasma allows fast switching that can follow the availability of energy surplus. The main reason for this is the *low inertia* of a plasma reactor such that the plasma can be turned off and on and the input power can be regulated quickly (in sub-second time scale, no heating of catalytic surfaces is required).

In order to understand how plasma technology can help in advancing the energy efficiency and CO_2 conversion, let's consider a simplified model. In this model, the plasma is formed by applying a power to a gas that causes breakdown (i.e. electrons, ions and other reactive species are formed). Energetic electrons that are formed can activate the CO_2 gas by electron impact processes. Moreover, the ionization degree of these plasmas (i.e. the ratio of major charged species and neutral ones) is on the order of 10^{-7}–10^{-4}. In this range, the plasma is called *weakly ionized*, such that the energy to produce the plasma is relatively low contribution in the overall energy balance. In this way, even processes like (1.1) can occur with reasonable energy consumptions. In such type of plasmas, it is possible to define a characteristic time t_r, the so called *residence time*, that the particles spend inside the reactor volume, according to the expression (1.4).

$$t_r = \frac{V}{\Phi} \tag{1.4}$$

where V is the reactor volume and Φ is the particle flow rate (usually expressed standard liters-per-minutes, then converted in m^3/s). To give some numbers: for a typical reactor with a cylindrical volume of radius 1 cm and length 10 cm, at a pressure of 20 Torr, gas temperature 300 K and particle flow rate of 5 slm, a residence time of $t_r = 9.03$ ms is calculated. Moreover, by knowing the gas density n of a plasma, it is possible to deduce the *gas density flow rate* (1.5) that represents the number of particles per seconds that are contained in a specific volume:

$$Q_n = \frac{n}{t_r} = \frac{p}{k_B T_g t_r} \tag{1.5}$$

where e is the elementary charge, p is the gas pressure, k_B is the Boltzmann constant and T_g is the gas temperature. For the case of the example before, a gas density flow rate of $Q_n = 7.13 \cdot 10^{25}$ $\mathrm{m^{-3}s^{-1}}$ is calculated. In order to calculate the energy efficiency of the process, the specific energy input (i.e. SEI) is calculated according to (1.6):

$$SEI = \frac{\rho}{eQ_n} \tag{1.6}$$

for a characteristic power density of $\rho = 1{\cdot}10^7$ $\mathrm{W/m^3}$, a $SEI = 0.88$ eV/molecule is calculated. The conversion rate of CO_2, X_{CO_2}, is calculated as (1.7):

$$X_{CO_2}(\%) = \left(1 - \frac{n_{CO_2,tot}(t_r)}{n_{CO_2,tot}(0)}\right) \cdot 100\% \tag{1.7}$$

where $n_{CO_2,tot}$ is the sum of the number densities of CO_2 and all its excited states. The energy efficiency η is then calculated from (1.8):

$$\eta(\%) = \frac{2.9\ eV}{SEI} \cdot X_{CO_2} \tag{1.8}$$

where 2.9 eV is the standard reaction enthalpy of the reaction $CO_2 \rightarrow CO{+}1/2O_2$ [8]. Results from Russian literature [9] has been demonstrated to achieve high energy efficiencies (i.e. up to 90%), but only at moderate conversion efficiencies (i.e. around 20%). Conversely, the highest conversion efficiencies were achieved at a moderate energy efficiency. These results were obtained in particular conditions at strongly sub-atmospheric pressures. At elevated pressures, the energy efficiency remain very low, typically below 10% [10].

1.3.2 Non-equilibrium nature of plasmas

Plasma are chemically active media that are created by applying energy to a gas in order to re-organize the electronic structure of the species (atoms, molecules) and to produce excited species and ions. This energy can be thermal, or carried by either an electric current or electromagnetic radiations [11]. The electric field transmits energy to the gas electrons. This energy is then transmitted from the electrons to the neutral species by collisions. These collisions can be divided into two types:

- *Elastic collisions:* that do not change the internal energy of the neutral species, but contributes only to the change of the kinetic energy.
- *Inelastic collisions:* in which high energy electrons can modify chemical bonds in molecules and the electronic structure of neutral species without heating the gas.

Depending on the type of energy supply and the amounts of energy transferred to the plasma, the properties of the plasma change, in terms of electronic density or temperature. These two parameters distinguish plasmas into different categories [11]:

- Local thermodynamic (or thermal) equilibrium plasmas (LTE).
- Non-local thermodynamic equilibrium plasmas (non-LTE).

In LTE plasmas, transitions and chemical reactions are governed by collisions and not by radiative processes. Moreover, each collisions in this plasma are described by one temperature equal for each species. In LTE, heavy particles temperature (i.e. T_h) is equal to the electronic one (i.e. T_e). These conditions are well represented by an *arc plasma* where $T_e = T_h \sim 10^4$

K and the electron density is high (i.e. $\gg 10^{21}$ m^{-3}). In fact, at higher pressures, collisions intensify and a thermal plasma is obtained where the temperatures are almost all equal. On the contrary, in low pressure plasmas (of the order of 1 mbar), the difference in temperatures can become very high and therefore a *non-equilibrium plasma* is achieved. In particular, non-LTE plasmas are characterized by an electron temperature much higher than the gas temperature, such that it can be described by a two temperature model (i.e. with $T_e \gg T_h$). In this type of plasmas, the electron density is lower (i.e. $\leq 10^{20}$ m^{-3}) such that heavy particles are moderately heated by a few elastic collisions. The purpose of the current researches is, thus, to find the optimal condition to obtain a non-equilibrium character in the case of a CO_2 plasma[1].

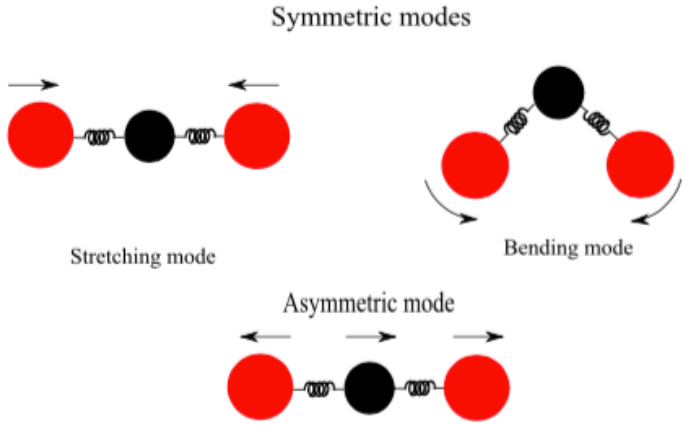

Figure 1.3: ***Different modes of vibration of a CO_2 molecule. Red spheres represent the O atoms, while black ones represent C atoms. From [13].***

If molecules are considered, even internal vibrational and rotational degrees of freedom have to be considered. That internal modes can be populated by inelastic collisions. In particular, considering a CO_2 plasma, three primary mechanisms are responsible for the vibrational energy exchange between different modes or degrees of freedom:

- *VV relaxation:* this process is responsible for exchange o vibrational energy among two molecules in the same mode of vibration.
- *VV' relaxation:* this process is responsible for losses of vibrational energy among two modes of vibration of the same molecule.
- *VT relaxation:* with this process the vibrational energy is lost to translational degrees of freedom.

As shown in Fig.(1.4), since CO_2 is a polyatomic molecule, different modes of vibration has to be considered that can be populated by inelastic collisions (see Chap. 4). These modes can be divided into *symmetric modes* of vibration, which are further divided into *symmetric stretch mode* and two degenerate *bending modes*, and *antisymmetric mode* of vibration. A key to obtain high energy efficiency is to create a thermodynamic non-equilibrium condition between vibration and translational/rotational energy distribution of the molecule by channeling the energy mainly into the asymmetric stretch mode[2] [9]. In this way, CO_2 splitting proceeds

[1]The non-equilibrium character of plasmas was for a long time best realised by low pressure plasmas, but now atmospheric pressure plasmas are emerging as an attractive alternative and generated a huge interest over the last decade. The non-equilibrium character of these plasmas can be controlled by large gas flows or by short pulsed excitation assuring strong cooling mechanisms or combinations of both [12].

[2]Symmetric modes have lower cross sections in the range of energy of interests (i.e. between 0.4 and 2 eV).

according to the stepwise reactions (1.9). CO_2 molecule in ground state (i.e. $^1\Sigma^+$) are excited by electron impact vibrational excitation of the lowest vibrational level. Higher vibrational states are gradually populated by vibrational-vibrational (VV) collisions, until the $^3B_2$ state is reached, at the point where energy level and molecular distance of the $O = CO$ bond coincide. The energy cost of this process is 5.5 eV, leading to CO and O in the ground state. This process is called *ladder climbing* and is schematically shown in Fig.(1.4).

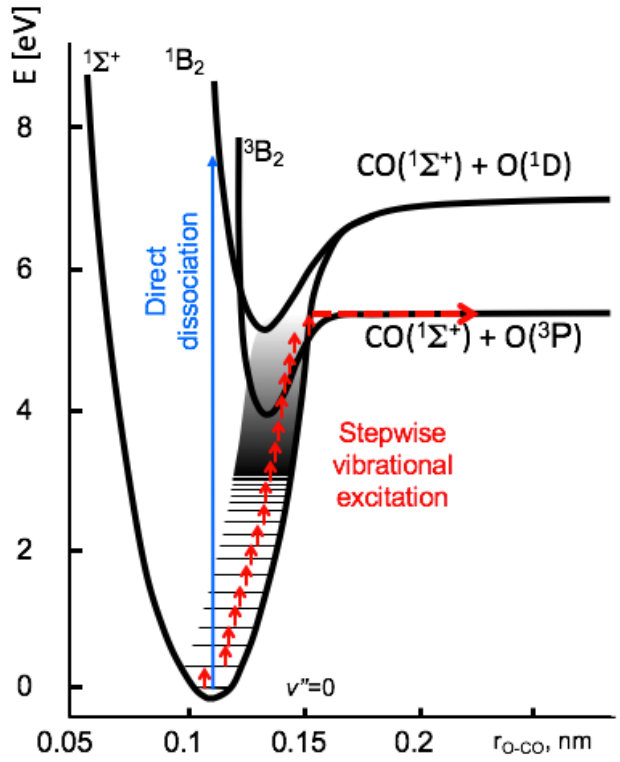

Figure 1.4: ***Potential energy diagrams (as a function of one OCO bond length). Red arrows represent a stepwise vibrational excitation, while blue arrow represent a direct dissociation.***

$$\mathbf{CO_2^*}(^1\Sigma^+) \rightarrow \mathbf{CO_2^*}(^3B_2) \rightarrow \mathbf{CO}(^1\Sigma^+) + \mathbf{O}(^3P) \tag{1.9}$$

Moreover, the oxygen atoms produced undergo secondary reactions with CO_2 producing one more CO molecule with energy cost of 0.3 eV. Since vibrational excitation leads to dissociation at energies around 5.5 eV that are significantly lower than the ones normally needed for direct electron impact processes (i.e. > 7 eV), higher energy efficiencies can be obtained.

1.4 State of the art technology

Several types of plasma source have been explored [11]. These sources differ from each other mainly for the geometry and coupling power methods that lead to different energy efficiencies and conversion. In this thesis, particular focus will be paid to two types of plasma sources (i.e. *Dielectric Barrier Discharges* and *Microwave sources*).

Dielectric Barrier Discharges The DBD device is composed by two electrodes in cylindrical or plane geometry. The gap is limited to a few millimetres wide and a plasma gas flow

in the gap. A sinusoidal or pulsed power source ignite the discharge that can present either *homogeneous* or *filamentary modes*, depending on the nature of the gas, the electrodes, the pressure and the electrodes gap [14]. Despite the simple design, this type of source can be easily scaled up to industrial applications while operating at atmospheric pressure. Conversion efficiencies up to 35% were measured [15]. However, opposite trends of CO_2 conversion and energy efficiency are reported as a function of the SEI, such that the higher conversion efficiency corresponds to a lower value of energy efficiency of a few %. This dependence is shown in Fig.(1.5) and it is due to the high reduced electric field (i.e. typically greater than 200 Td) that is applied and limit intrinsically the achievement of energy efficiencies higher than 10%.

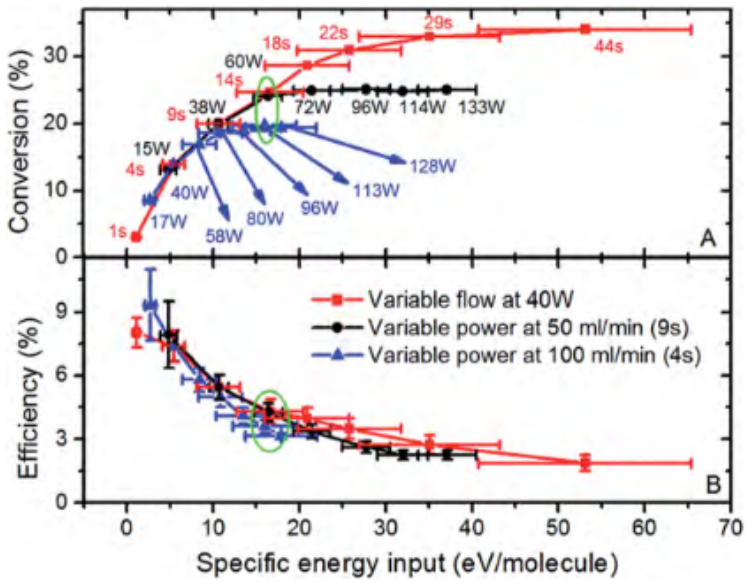

Figure 1.5: ***Measured CO_2 conversion (A) and energy efficiency (B) in a DBD reactor, as a function of the specific energy input (SEI). From [15].***

Microwave Sources In this configuration, microwaves are guided along the system and transmit energy to the electrons and heavy particles. After several elastic collisions, the electrons gain enough energy to undergo inelastic processes of excitation and ionization. As example, a scheme of a microwave source used in Stuttgart is shown in Fig.(1.6) and it consists of:

- A MW power source (i.e. power supply, magnetron, etc.).
- The microwave is supplied to the resonator via a rectangular waveguide from the magnetron.
- Wave guides and tuning system are used to achieve the ignition of the plasma by the resonator. During this operation, the resonance frequency of this resonator has to perfectly match the frequency of the microwave provided by the used magnetron. The microwave discharge operates usually at a frequency of 915 MHz or 2.45 GHz.
- The plasma is ignited and confined in a MW transparent tube (e.g. a quartz tube[3]).

[3]The permittivity of the quartz tube also affects the resonance frequency. Since it is greater than one, the volume of the cylindrical resonator is virtually enlarged which leads to a lower resonance frequency.

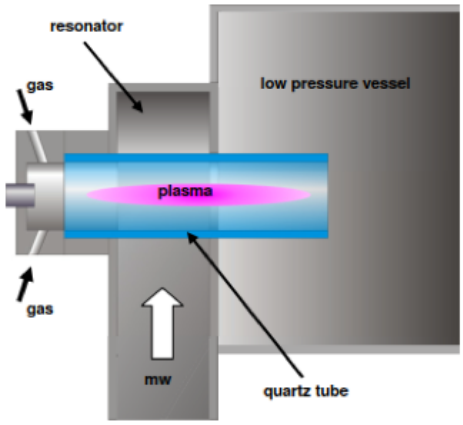

Figure 1.6: ***Discharge with resonant cavity.***

MW plasma have been demonstrated to be the most suitable solution to obtain high energy efficiency and CO_2 conversion due to the low reduced electric field present in the microwave plasma (typically around 50 Td) that is most appropriate for vibrational excitation of CO_2. Moreover, microwave discharges can be sustained in non-equilibrium conditions at high SEI. Just to give an example, a microwave discharge can be sustained in CO_2 at a frequency of 2.45 GHz, power of 1.5 kW, pressure from 50 to 200 Torr, flow rate of 0.15 to 25 l/min, while keeping an SEI from 0.2 to 2 eV/mol and a specific power up to 500 W/cm^3 [9]. In addition, Recent studies [9] reported the highest efficiency for a microwave plasma (i.e. around 90%), even if this was achieved under specific conditions (i.e. supersonic gas and reduced pressure around $100 - 200$ Torr). However, recently huge interest is emerging concerning atmospheric pressure plasmas that can be an attractive alternative. In order to control the non-equilibrium nature of atmospheric plasmas several studies are ongoing. The two most promising methods involve plasma control by large gas flows or by short pulsed excitation assuring strong cooling mechanisms or combinations of both.

Effect of flow According to [16], the effect of gas flow affects the plasma extent. In particular, the extent of the plasma has been demonstrated to be reduced by increasing the gas flow at fixed input MW power. The benefits of high flow rates are typically exploited in atmospheric (or high pressure) MW plasmas with the utilization of a converging-diverging nozzle where the the gas flows from a high pressure to a lower pressure. As shown in Fig.(1.7), the gas enters the converging section at a much lower velocity and, during passage of the gas through the nozzle, there will be a rapid transformation of thermal energy to kinetic energy. This kinetic energy will give rise to a very high gas velocity after discharging from the nozzle [17].

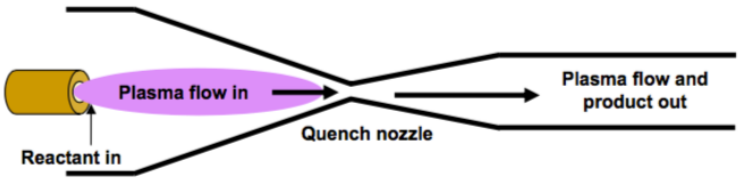

Figure 1.7: ***Schematic of plasma fast quench reactor with nozzle technology, from [17].***

When the gas accelerates through the nozzle throat, the temperature of the gas will simultaneously drop rapidly. This rapid temperature quenching freezes the equilibrium products of

a high temperature gas phase reaction, thus preserving the maximum product yield. Recent studies [5] showed an increased energy efficiency up to 50% with a nozzle placed after the plasma.

Vortex stabilized plasma Interesting applications for a stabilization of a plasma are the forward and reverse vortex flow. As shown in Fig.(1.8), in *forward-vortex* configuration, the swirl generator is placed upstream with respect to discharge, whereas in *reverse-vortex* configuration the outlet of the plasma is directed along the axis to the swirl generator side. According to [9], reverse-vortex configurations are demonstrated to be effective for increasing conversion efficiency. In fact, in this configuration it is expected that cold incoming gas moves at first by the walls providing cooling and insulation and only after that, it goes to the central plasma zone and becomes hot.

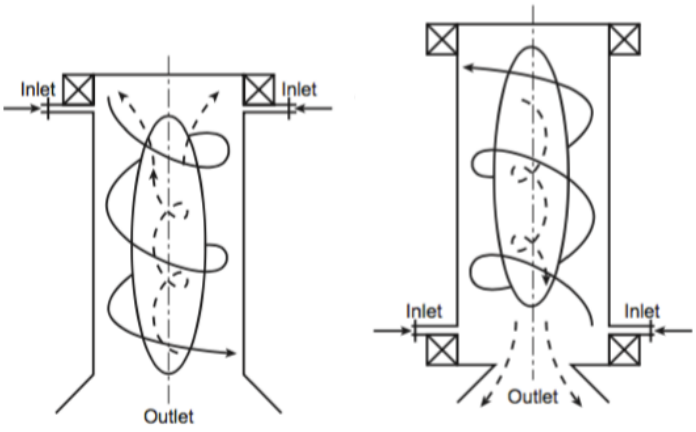

(a) Forward vortex configuration.

(b) Reverse vortex configuration.

Figure 1.8: ***Plasma stabilization with a forward vortex (left) and reverse vortex (right) configuration, from [9].***

Effect of pulsing Recent studies [18] showed a benefit of pulsed system where the power is transferred preferentially to excited levels leading to dissociation. Benefit of pulsing are recognized to be beneficial for an accumulation effect of excited species. Determination of an optimal duty cycle for pulsed mode is matter of timescales. In fact, in the discharge very different timescales are present, ranging from the fast electronic excitation (i.e. in the order of ns) to the slow neutral gas dynamics (i.e. in the order of ms to s).

CHAPTER 2

Description of the model

In this Chapter a first introduction on Global Models is presented starting from the physical point of view and focusing on the numerical implementation on the software PLASIMO. These models calculate the volume-averaged plasma quantities such as the particle densities and the electron temperature that are deduced from particle balance equations and an electron energy balance equation integrated over the plasma volume. These type of models have become popular tools for of chemists and spectroscopists in the last two decades since they have proven to be predictive [19], within a few multiplicative factors, and they are widely used to study discharges of many types due to the possibility of implementing complex chemistry and plasma processes.

2.1 Global model for plasma chemistry

The general framework of the global model that will be introduced here is schematized in Fig.(2.1). From this diagram it is possible to see that there is a gas inlet of CO_2 molecules and an electrical power source that create some plasma with a certain electron temperature and density. These molecules are dissociated by the plasma to create neutral radicals (i.e. C and O), molecules (i.e. CO and O_2), positive and negative ions and some excited species (i.e. in the electronic or vibrational excited states). All these species can undergo secondary reactions which create a wide variety of plasma species. In this bulk plasma, transport is mainly determined by diffusion processes. There is also transport to the sheath, where positive ions are transported to the surface and negative ions are trapped inside the plasma. Moreover, with the substrate itself there are also surface interactions that change the composition of the plasma. The resulting species are then pumped out through the exhaust.

In order to describe this complex system, a statistical approach is needed. This is introduced by defining a *distribution function* $f(\vec{r}, \vec{v}, t)$ such that, once multiplied by the infinitesimal volume $d\vec{r}d\vec{v}$, it gives the number of particles at time t that are contained in the phase space volume[1] centred in $\vec{r}$ and $\vec{v}$. Actually, there is a distribution function for each species s such

[1] Phase space is a 6-D space with three dimensions in velocity and three dimensions in configuration space.

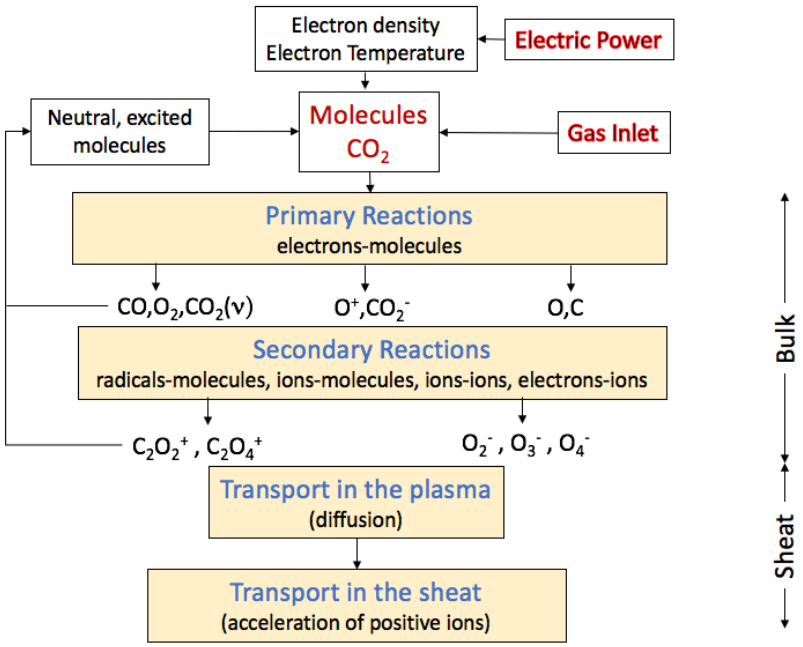

Figure 2.1: ***General scheme of a plasma chemistry model.***

that their evolution in time in the phase space volume is defined by the so called *Boltzmann equation* (2.1):

$$\frac{\partial f_s}{\partial t} + \vec{v}_s \cdot \vec{\nabla}_x f_s + \frac{\vec{F}_s}{m_s} \cdot \vec{\nabla}_u f_s = \left(\frac{\partial f_s}{\partial t}\right)_C \tag{2.1}$$

where $\vec{F}_s$ is the force field, m_s is the mass of the particles, $\vec{\nabla}_x f_s$ and $\vec{\nabla}_u f_s$ are the spatial and velocity derivative of the distribution function f_s. The term on right hand side of (2.1) is the so called *collision operator* which takes into account elastic and inelastic processes such that it gives the evolution of the distribution function due to collisions. The equations used in model comes from the moments of Boltzmann equation that are defined by integrating (2.1) over the velocity component of the phase space. In particular, global models include particle balance equations and an electron energy balance equation that are integrated over the plasma volume. In order to define the set of equations, some important *approximations* are made about the plasma considered such that:

- Plasma is *homogeneous* (i.e. its quantities do not significantly differ spatially compared to their volume average) so all spatial derivatives are zero. This means that there is no *transport* (in configuration space) considered in the model
- Electrons are first in getting energy from electric fields, because of their low mass and high mobility. So that they transmit the energy to all other plasma components. In this way it is assumed that all input power is directly coupled to the electrons
- The power deposition is approximated by an averaged value over the plasma volume
- In this model it is assumed that gas temperature is fixed, thus only energy balance for electrons is solved

A more detailed description is given in many classical physics textbooks, such as [20]

If transport is neglected, the zero*th* moment of Boltzmann equation (2.1) deals with conservation of mass (or particles) and it is defined as (2.2):

$$\frac{\partial n_s}{\partial t} = S_s \tag{2.2}$$

where S_s is the net source term that takes into account all the chemical reactions that create or destruct the particles. The particle balance equations (2.2) determine the volume-averaged densities except for the electrons, the density of which is computed from the quasi-neutrality requirement. According to [21], if a reaction j is considered, which can be written as:

$$\sum_s \alpha_{j,s} X_s \rightarrow \sum_s \beta_{j,s} X_s \tag{2.3}$$

where X_s represents a species s, $\alpha_{j,s}$ and $\beta_{j,s}$ are the stoichiometric coefficients of the reactions. For the generic reaction (2.3), the source term of equation (2.2) is generally expressed as (2.4) with a summation of the reaction rates R_j, with j the specific reaction considered:

$$S_{net,s} = \sum_{j=1}^{n} \left(\beta_{j,s} - \alpha_{j,s}\right) R_j \tag{2.4}$$

where the rates R^j are given by (2.5):

$$R_j = k_j(T_e, T_h) \prod_s n_s^{\nu_{js}} \tag{2.5}$$

where the product runs over all species s with densities n_s and ν_{js} is the stoichiometric coefficient for the j reaction. In this expression, k_j is the rate coefficient for the jth reaction that can be constant or temperature dependent. In this respect, the source terms (2.4) depend on the species densities and on the rate coefficients of every reaction. For calculating the rate coefficients, the electron energy balance equation (2.6) (i.e. from the second moment of Boltzmann equation) is coupled to the continuity equation and provides the time evolution of the mean electron energy density ϵ:

$$\frac{\partial \epsilon}{\partial t} = P_{input}(t) - Q_{elas} - Q_{inelas} \tag{2.6}$$

where $P_{input}(t)$ is the input power density that can be time dependent and it is defined externally. Q_{elas} and Q_{inelas} are the net energy losses from elastic and inelastic processes respectively that are calculated according to (2.7) and (2.8):

$$Q_{elas} = \sum_{j,elas} \frac{3}{2} k_B (T_e - T_g) \frac{2m_e}{m_s} R_j \tag{2.7}$$

$$Q_{inelas} = \sum_{j,inelas} U_{th,j} R_j \tag{2.8}$$

where the summations in (2.7) and (2.8) run over all elastic and inelastic processes respectively, $\mathrm{U}_{th,j}$ is the threshold energy of reaction j, T_g the gas temperature and m_e/m_i the ratio of electron mass over the mass of the colliding species [21].

The goal of the model is to solve simultaneously the species density balance (2.2) and the electron energy balance (2.6) as a function of time. For this purpose, the model needs as an input the rate coefficients of all reactions as a function of energy. As shown in (2.9), if

processes involving electrons are considered, the rate coefficients k_j are determined by the convolution of a cross section with the electron energy distribution function (EEDF) [21], at least for binary processes[2].

$$k_j = \int_{\epsilon_{th}}^{\infty} v(\epsilon)\sigma_j(v)f(\epsilon)d\epsilon \tag{2.9}$$

where ϵ is the mean electron energy, $v(\epsilon)$ the velocity of the electrons, $\sigma_j(v)$ the cross section of collision j, ϵ_{th} the threshold energy of the collision and $f(\epsilon)$ is the electron energy distribution function (EEDF). For the calculation of the EEDF, the Boltzmann solver BOLSIG+ was used [22]. In particular, if the EEDF is described by the Maxwell-Boltzmann distribution function[3], the mean electron energy density ϵ is proportional to the electron temperature via (2.10):

$$\epsilon = \frac{3}{2} n_e k_B T_e \tag{2.10}$$

where k_B is the Boltzmann constant. On the contrary, when all the reacting species are *heavy*, or non-electronic, there is usually a presumption that the reacting species have a Maxwell-Boltzmann distribution of energies with a common temperature T, and the rate constant may then be expressed as a parametric function of this temperature. The form usually chosen is of the extended *Arrhenius type* [23]:

$$k_j(T) = AT^B exp(-C/T) \tag{2.11}$$

where A, B and C are constants.

Input chemistry The input chemistry used is taken from Koelman et al. [21] who adapted the chemistry from the works of Kozak and Bogaerts [8]. The species, both in ground state and in excited states, are included in the model are given in Tab.(2.1).

Table 2.1: ***Plasma species included in CO_2 chemical model.***

CO_2 Model: input species
Molecules
CO_2, CO, O_2, O_3
Charged Species
CO_2^+, CO_4^+, CO^+, $C_2O_2^+$, $C_2O_3^+$, $C_2O_4^+$
C^+, C_2^+, O^+, O_2^+, O_4^+
CO_2^-, CO_3^-, CO_4^-, O^-, O_2^-, O_3^-
O_4^-, e^-
Radicals
C_2O, C, C_2, O
Excited Species
$CO_2(e_1)$, $CO_2(e_2)$, $CO_2(\nu_a \dots \nu_d)$, $CO_2(\nu_1 \dots \nu_{21})$
$CO(e_1)$, $CO(e_2)$, $CO(e_3)$, $CO(e_4)$, $CO(\nu_1 \dots \nu_{10})$
$O_2(e_1)$, $O_2(e_2)$, $O_2(\nu_1 \dots \nu_3)$

[2] Ternary processes typically are convenient representation of a chain of binary processes involving transient intermediate states.

[3] This is the distribution function of the electron (and ions) once the thermal equilibrium between them is attained.

The list of electronically excited species included is reported in Tab.(2.2) together with the notation given by Aerts [18] and the identification based on the cross sectional data. As referred in Koelman et al. [21], some states represent the sum of various excited states. Moreover, according to Phelps database [24] and Lowke [25], the 7 eV threshold process of CO_2 excitation is considered as a dissociative channel, while the electronic excitation is limited to a process with energy threshold of 10.5 eV. For species in the electronic ground state but

Table 2.2: ***Identification of electronically excited states included in the CO_2 model.***

Model Notation	Aerts Notation	States Identification	Threshold Energy [eV]	Reference
$CO_2(e_1)$	$CO_2(^1\Pi_g)$		7.0	[24]
$CO_2(e_2)$	$CO_2(^1\Delta_u)$		10.5	[24]
$CO(e_1)$	$CO(A^3\Pi)$	$CO(a^3\Pi)$	6.22	[24]
$CO(e_2)$	$CO(A^1\Pi)$	$CO(A^1\Pi)$	7.90	[24]
$CO(e_3)$	$CO(A^3\Sigma)$, $CO(D^3\Delta)$, $CO(E^3\Sigma)$, $CO(B^3\Sigma)$	$CO(a'\ ^3\Sigma^+)$	6.80	[24]
$CO(e_4)$	$CO(C^1\Sigma)$, $CO(E^1\Sigma)$, $CO(E^3\Sigma)$, $CO(I^1\Sigma)$, $CO(D^1\Sigma)$	$CO(C^1\Sigma^+ + E^1\Pi)$	10.60	[24]
$O_2(e_1)$	$O_2(a^1\Delta)$ and $O_2(b^1\Sigma)$	$O_2(A^1\Delta_g)$	0.977	[26]
$O_2(e_2)$	$O_2(B^3\Sigma)$ and higher triplets	$O_2(B^1\Sigma_g{}^+)$	1.627	[26]

vibrationally excited, the energy of the corresponding vibrational states are calculated via the anharmonic oscillator approximation, as given in [8]. For example, the CO_2 molecule exhibits vibrations in three main modes (i.e. symmetric stretching, bending and asymmetric stretching). In this model, species that represent the asymmetric vibrationally excited states of the CO_2 molecule are denoted as $CO_2\nu_i$ with $\nu = 1, \ldots, 21$, while $CO_2\nu_\alpha$ with $\alpha = a, \ldots, d$ represent collections of symmetric vibrational modes. The effective energy levels of CO_2 vibrational states included in the model are presented in Tab.(2.3). Only vibrational levels that are assumed to be important for CO_2 dissociation are included. In particular, since theoretical background [9] concludes that the asymmetric stretch mode provides the most important channel for dissociation, thus asymmetric mode levels of CO_2 up to a dissociation energy of 5.5 eV are taken into account.

The reaction set included for electrons, ions, neutrals and excited species is reported in Appendix A. As referred in [8], most electron impact reactions are described by cross sections in Tab.(1) and (2). The electron attachment and electron-ion recombination reactions are given in Tab.(3) and are characterized by rate constants. Moreover, neutral species reactions

Table 2.3: ***Vibrational levels of CO_2 included in the model. The levels denoted by letters represent symmetric modes of vibration, while the levels denoted by numbers correspond to asymmetric modes. Energies are taken from [8].***

Model notation	States	Energy (eV)
CO_2	(0 0 0)	0.00
$CO_2(\nu_a)$	(0 1 0)	0.08
$CO_2(\nu_b)$	(0 2 0) + (1 0 0)	0.17
$CO_2(\nu_c)$	(0 3 0) + (1 1 0)	0.25
$CO_2(\nu_d)$	(0 4 0) + (1 2 0) + (2 0 0)	0.33
$CO_2(\nu_1)$	(0 0 1)	0.29
$CO_2(\nu_2)$	(0 0 2)	0.58
$CO_2(\nu_3)$	(0 0 3)	0.86
$CO_2(\nu_4)$	(0 0 4)	1.14
$CO_2(\nu_5)$	(0 0 5)	1.43
$CO_2(\nu_6)$	(0 0 6)	1.70
$CO_2(\nu_7)$	(0 0 7)	1.97
$CO_2(\nu_8)$	(0 0 8)	2.24
$CO_2(\nu_9)$	(0 0 9)	2.51
$CO_2(\nu_{10})$	(0 0 10)	2.77
$CO_2(\nu_{11})$	(0 0 11)	3.03
$CO_2(\nu_{12})$	(0 0 12)	3.29
$CO_2(\nu_{13})$	(0 0 13)	3.55
$CO_2(\nu_{14})$	(0 0 14)	3.80
$CO_2(\nu_{15})$	(0 0 15)	4.04
$CO_2(\nu_{16})$	(0 0 16)	4.29
$CO_2(\nu_{17})$	(0 0 17)	4.53
$CO_2(\nu_{18})$	(0 0 18)	4.77
$CO_2(\nu_{19})$	(0 0 19)	5.01
$CO_2(\nu_{20})$	(0 0 20)	5.24
$CO_2(\nu_{21})$	(0 0 21)	5.47

are presented in Tab.(ref) and reactions with charged species are reported in Tab.(5), (5) and (5). In conclusion, reactions that involve vibrational energy exchange are reported in Tab.(2.3). Due to a lack in rate coefficients for charge exchange reactions with electronically excited species, a scaling law is adopted and suggested in [21]. This scaling is reported to be as:

$$k = k_0 \frac{E_i^2}{(E_i - E_e)^2} \tag{2.12}$$

with k_0 the ground state rate coefficient, E_i the ionization potential of the excited species and E_e its excitation energy. Furthermore, since there is little rate coefficients data available in literature for energy exchange between vibrational levels, a scaling law is needed as well. The SSH (Schwartz, Slawsky and Herzfeld) theory is adopted and described in details in [9]. Cross sections for excitation into higher asymmetric mode vibrational levels are scaled as well using the *Fridman approximation* [9] to obtain the cross section σ_{nm} for excitation from $CO_2(\nu_n)$ to $CO_2(\nu_m)$ as:

$$\sigma_{nm} = exp\left(\frac{-\alpha(m-n-1)}{1+\beta n}\right)\sigma_{01}(\epsilon + E_{01} - E_{nm}) \tag{2.13}$$

where σ_{01} is the cross section for excitation from the ground state to $CO_2(\nu_1)$, $E_{01} = E_0 - E_1$ and $E_{nm} = E_n - E_m$ are the corresponding threshold energies for excitation. Thus, this approxiamtion shifts the cross sections according with two parameters α and β. In this model α is set to 0.5 for CO_2 and 0.6 for CO, while β is fixed at 0, according to [8]. Vibrational excitation can also lower the energy barrier for chemical reactions between neutral species. To account this effect, the following general formula for rate coefficients is used:

$$k(E_v, T) = A_0 exp\left(-\frac{(E_a - \alpha E_v)}{T}\right) \tag{2.14}$$

where E_a is the activation energy of the reaction, E_v is the energy of the vibrational level and α a parameter determining the efficiency of lowering the energy barrier of the reaction considered. The value for α is taken according to the *Fridman-Macheret α model* [9] (see Tab.(4)) and depends on reactions considered. For example, for the most important dissociation reaction (N1) a value of 0.8 is used.

2.2 Numerical implementation

In this thesis, the platform PLASIMO was used to unravel principal pathways in CO_2 plasmas. In this part, a general overview on the structure of this software is done, focusing on numerical aspects, inputs and outputs of the model.

The PLASIMO (i.e. **PL**asma **SI**mulation **MO**del) code is a toolbox that provides support for the numerical simulation of plasma sources of various degrees of equilibrium [27]. It was written in C++ and developed in the Eindhoven University of Technology in the groups of *Plasma and Material Processing* (PMP) and *Elementary Procecess of Gas discharges* (EPG) of the department of Applied Physics. The main feature of this code is that it is *modular*, meaning that it is designed as a collection of modules that can be combined together to form a new model. Examples of such models are those for calculating the gas temperature, the chemical composition of a Local Thermodynamic Equilibrium (LTE) mixture or the flow field [28]. The advantage of this configuration is that these specific modules can be combined to form larger models. The main focus of this thesis is about Global Models in order to investigate the principal pathways in a CO_2 discharge. The general structure of these type of models can be seen in Fig.(2.2).

This general structure can be schematized in three main blocks:

- **Governing Equations:** it includes the *particle balance equations* (2.2) and *electron energy balance equation* (2.6) that are solved simultaneously.
- **External Parameters:** those are external inputs defined by the user, such as: *input power density* and *control parameters* (that allows, for example, to set some constant densities or temperatures or to use the quasi-neutrality condition)
- **Chemistry:** it includes all the *species densities* and *reactions* involved. Moreover it is possible to define the *initial conditions* (such as initial densities and temperatures). This part takes into account all the *reaction rates coefficients* as inputs (taken from literature or calculated from a database)

Once solved the corresponding particle balance (2.2) and electron energy balance equations (2.6), the following *outputs* are obtained:

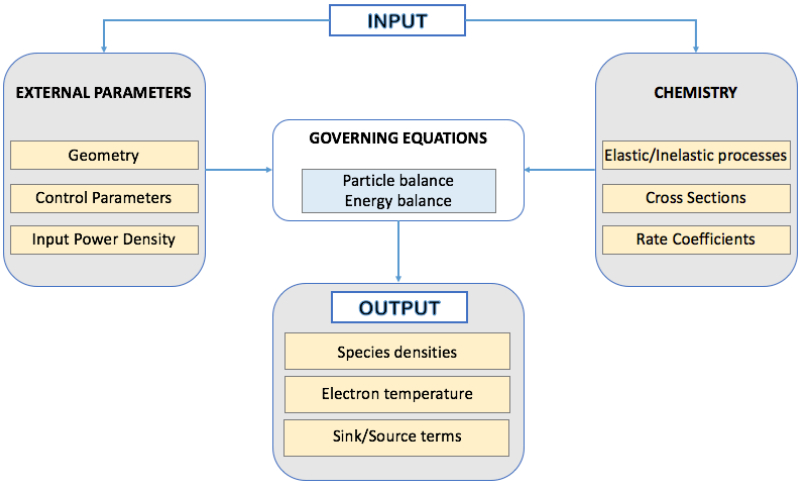

Figure 2.2: ***General structure of a Global Model in Plasimo.***

- Time evolution of species densities and electron temperature (i.e. gas temperature is fixed during simulation time)
- Source terms (2.4) of the particle balance equation for each species and reaction rates
- Sinks and sources (2.7) (2.8) of the energy balance equations due to elastic and inelastic processes

In this Section, the first two main blocks are described concerning governing equations and their numerical implementation in PLASIMO and the external input parameters, while the chemistry was already introduced in Sec.(2.1).

Governing Equations The equations included in the Global Model used in this work are introduced in Sec.(2.1). These equations consider balance processes that lead to the evolution of specie densities and electron temperature in time. Following the approach of [29], on the point of view of numerical implementation, the balance equation for all species densities can be implemented in a vector equation (2.15):

$$\frac{\partial \mathbf{n}(t)}{\partial t} = \mathbf{S}(\mathbf{n}(t)) \tag{2.15}$$

where $\mathbf{n}(t)$ is a vector containing all species densities and $\mathbf{S}(\mathbf{n}(t))$ is the corresponding source vector that depends on the densities of the other species. In general, the source terms are determined through a summation of all reaction rates that are weighted by the corresponding stoichiometric coefficient. This procedure can now be expressed using a more convenient matrix-vector multiplication to derive the source vector $\mathbf{S}$, according to (2.16):

$$\mathbf{S} = \mathbf{WR} \tag{2.16}$$

where $\mathbf{W}$ is the stoichiometric matrix whose rows refer to the species and columns to the reaction rates and $\mathbf{R}$ is a vector of rates (one per reaction). In the same way source and sink terms of the electron energy balance equation (2.6) can be constructing starting from the calculation of the rates vector $\mathbf{R}$. In this formulation, the backward processes are not included and must be defined either by including it explicitely or by applying detailed balancing. The following steps are performed once the simulation has started:

1. Calculate the rate vector **R**
2. Calculate the source vector **S** from (2.5) for the particle balance equations
3. Calculate the source and sink terms for the electron energy balance equation

The result of this calculation will be a vector of species densities and the electron energy density as a function of time. Just as the densities and electron energy densities, the rates of each reactions are stored at each time steps so the dominant reactions can be analyzed.

Solver The resulting vectors aforementioned at each time step are provided to a solver that calculates the values for the next time step. The particular choice of solver is made depending on the numerical characteristic of the problems. In general, the *stiffness* of the problem define of type of differential equations for which certain numerical methods are unstable, unless the step size is extremely small. Thus, it is very important to use a solver that solves stiff equations efficiently without an excessive computational load for the simulation. Numerous solvers are available to handle this specific type of problems. In particular, in this version of PLASIMO the solver used is called **L**ivermore **S**olver for **O**rdinary **D**ifferential equations, with **A**utomatic method switching (LSODA) [30]. This solver classifies the problem based on the previous time step, then automatically choses the optimal algorithm based on the maximum time step[4]. Usually a maximum time step of 1 s is used, absolute and relative tolerances are set to $1{\cdot}10^{-8}$ s.

External input parameters Several number of options can be specified by the user before performing the simulations. These options can be defined directly in the input files or through a Grafical User Interface (GUI) that facilitates the implementation. The main external parameters that can be set are:

- *Species List* and *Reaction List* are usually defined externally by including a file where each species is characterized by a unique name, while each reactions has a correspondent format and is associated to a rate coefficient (that are calculated from an Arrhenius form or implemented through a lookup table as a function of electron energy)
- *Input Power Density* can be included as a lookup table in an external file by defining the power as a function of time. The application of a constant power density is also possible within the model
- *Other Options* are possible such as it is possible to add a species to a constant density, in this way the source term for that species will be set to zero (i.e. it will remain at its initial value). Electron temperature can be also set as a constant (i.e. so it will be not computed from the energy balance equation), while gas temperature is already fixed by default
- *Quasi-Neutrality* can be assumed so that the electron density n_e is not solved separately but set equal to the ion density, as (2.17):

$$\sum_i (q_i n_i) - n_e = 0 \tag{2.17}$$

  where q_i is the charge of the ion i with correspondent density n_i.

[4]To be more precise the solver implements two different methods: Adams method for non-stiff problems and Backward Differentiation Formula (BDF) for stiff problems. The solver automatically switches between these two methods depending on results from the previous time steps

2.3 Stepwise Approach

The Global Model presented above include a *self-consistent* description of the plasma.

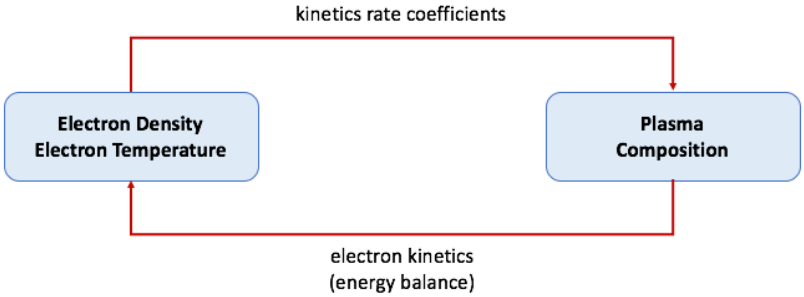

Figure 2.3: ***Self-consistent description of a plasma.***

This procedure is schematized in Fig.(2.3) and it starts with noticing that the electron temperature determines the plasma composition of species via the electron impact reactions. Moreover, once the composition is calculated (i.e. for each time step) it is possible to evaluate the electron temperature from the energy balance equation (2.6) since source and sinks terms of this equation are dependent in turn on the rates of elastic and inelastic processes, according to (2.7) and (2.8). This description is very complete since all the parameters of the plasma (i.e. except the gas temperature) are determined by solving a coupled set of balance equations. However, in order to unravel principal pathways and species in CO_2 discharges, a simplified *stepwise approach* was adopted here and presented in the following. Starting from the model presented in [21] and [8], new input files have been created and run in PLASIMO in order to study several different subsets of the model. All different subsets considered are schematized in Fig.(2.4).

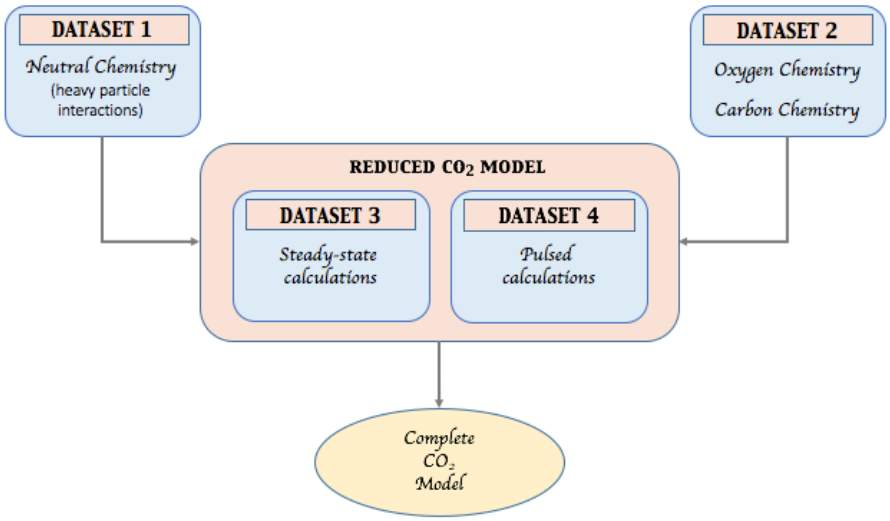

Figure 2.4: ***Stepwise approach adopted in this thesis.***

In total, four datasets are taken into account that differ between each other for the chemistry or input parameters considered:

- *Dataset 1:* It aims on studying the effect of heavy particle interactions due to change in the gas temperature of the system. In this dataset, only neutral species in their ground state are considered. Their interaction is governed by gas temperature. Understanding

the equilibration of those reactions is fundamental for explaining processes happening in afterglow phase of a pulsed CO_2 discharge.

- *Dataset 2:* It deals with studying the chemistry oxygen separately in order to unravel principal reactions and species that are (or should be) implemented for an accurate description of CO_2 discharges. In this part a comparison between a full oxygen global model and a reduced version is presented. Moreover, some hints about carbon chemistry are highlighted.
- *Dataset 3:* It aims to study the influcence of electron involving processes in neutrals and ionic species on a reduced version of CO_2 model in which excited species were neglected. Steady-state calculations were performed in which electron density and temperature were fixed as an external parameters. From those calculations it is possible to derive the equilibrium composition of species and the relevant timescales.
- *Dataset 4:* The effect of pulsing is studied in a reduced CO_2 model in which excited species were neglected. First of all, the time evolution of the electron temperature were imposed externally as input. Then, other simulations were performed in which electron temperature was calculated self-consistently by the energy balance equation (2.6). In those simulations, the effect of applying high power density (more similar to a DBD case) and low power density (for the MW case) is studied.

Module 1 and 2 are presented in Chapter 3, while *Module 3* and 4 are described in Chapter 4, together with the calculations using the complete CO_2 model that take into account even vibrational kinetics.

Furthermore, due to the huge amount of species and reactions included, in plasma chemistry it is important to determine the minimum set of relevant species in order to describe properly the system. It can be attractive to simply remove species with lower densities. However, these species can react with other species via fast reactions such that the net contribution on the chemistry will be not negligible. In order to develop a proper technique, detailed studies on CO_2 plasma chemistry are of fundamental importance. In addition, *numerical reduction techniques* can be applied to determine a smaller dataset that takes into account the essence of the system. The implementation of some of these numerical methods (i.e. like *Principal Component Analysis*) will be presented in Chapter 5 and 6 together with the application on different plasma chemistry datasets.

Part I

Principal pathways in CO_2 plasmas

CHAPTER 3

Test of the model

In order to study the full CO_2 model, a stepwise approach was taken into account that aims to find the relevant principal pathways that governs carbon and oxygen dynamics. In addition, studies of heavy particle collisions between neutrals are of fundamental importance for describing thermal (or warm) plasmas used in CO_2 splitting and/or relevant processes happening during afterglow of pulsed simulations at high pressure (i.e. 1000 mbar). Furthermore, a comparison with other models is introduced here to check the auto-consistency of the reactions implemented.

3.1 Influence of heavy particle collisions

In this section, calculations to determine the equilibrium compositions are presented for different temperatures and a fixed pressure. Those calculations are performed with a thermodynamic model that minimise the Gibbs free energy for a given composition. Results of this model will be compared with a 0-D kinetic model implemented in PLASIMO. Furthermore, considerations on CO thermal production are deduced at the end of the section.

Note: In this section all the species taken into account are considered in *thermodynamic equilibrium*. As a matter of fact, this means that all the species have the same temperature and that the chemical processes are so fast that the densities can be expressed by analytical relations of statistical mechanics. Furthermore, in this section, only interactions between neutral species are considered, meaning here that the *equilibrium* condition refers always to heavy particles.

3.1.1 Comparison with thermodynamic model

Chemical equilibrium is usually determined in two ways: one is to define *rate constants* that determine the temporal evolution of the reactions; the other is the *minimisation of free energy*. Comparison between those two methods is useful to have a correct description of the system for different values of pressure and temperatures. This comparison is done here using the NASA computer program CEA [31] [32], that calculates the equilibrium composition minimising the Gibbs free energy, and a version of 0-D kinetic model implemented on PLASIMO. Both methods will be presented in this section.

Thermodynamic CEA model As referred in literature [33], the chemical state of a system is completely determined by temperature T, total volume V and number of moles N_j for each species. Those quantities uniquely identify a number of function of state, such as internal energy U, entropy S, enthalpy H and Gibbs free energy G such that the state of the system (at any time) can be completely determined by a specific number of state variables. If one wishes to use temperature and pressure to characterise a thermodynamic state, Gibbs energy is most easily considered since temperature and pressure are usual variables for describing a chemical system. In order to give an example, let's consider a chemical reaction of the form:

$$A + B \Leftrightarrow C + D \tag{3.1}$$

where A, B, C and D in (3.1) are the chemical species considered. In order for this reactions to proceed spontaneously (either to the left or to the right), the Gibbs free energy must decrease according to the second law of thermodynamics, as described by the inequality (3.2):

$$dG = dH - TdS = Vdp - SdT \leq 0 \tag{3.2}$$

where the final equality holds for reversible processes. In those conditions, the system will relax into a state in which the concentration of various species do not change spontaneously. This can be seen in Fig.3.1 where the the equilibrium state of reaction (3.1) is the minimum of the Gibbs free energy as a function of the composition of the system.

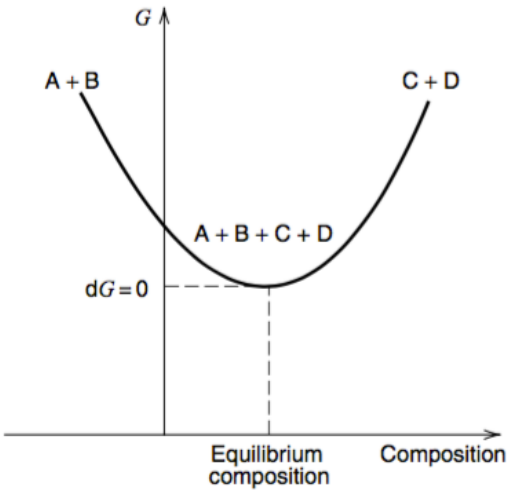

Figure 3.1: ***Schematic representation of the mimization of Gibbs free energy of the system along one reaction coordinate in the composition space, from [33].***

In this section the program used to calculate the equilibrium composition is called CEA (Chemical Equilibrium with Applications) and it was developed by the NASA Lewis Research Center [31]. This program requires two **inputs** to be run:

1. Chemical species composition (type of atoms or molecules, initial number of mole fractions, etc.)
2. Thermodynamic state variables to control and describe the equilibrium properties (i.e. two thermodynamic state functions to be chosen between Temperature, Pressure, Enthalpy, Entropy, Volume and Internal Energy)

since this model is based on thermodynamic calculations and it is *not* a kinetic model, reaction rate constants are not included. Thus, the final **output** composition of species is determined via a minimisation technique of the Gibbs free energy, as described in [31]. The following Tab.(3.1) summarises the initial input parameters used for the simulations.

Table 3.1: ***Input parameters used in the CEA program.***

Input Parameters	
Species:	CO_2, CO, C_2O, C, C_2, O, O_2, O_3
Temperature:	fixed values in the range [1000:6000] K
Pressure:	100 mbar

All the simulations were performed for a fixed pressure of 100 mbar that is a typical value for MW plasma discharges [34] and for different fixed values of temperature. The initial mole fractions of different species were set in order to have a pure CO_2 mixture as input parameter.

0-D kinetic model The kinetic model is included here to study the temporal evolution of the CO_2 composition. Such model was implemented on PLASIMO using the same **input parameters** as defined in Tab.(3.1) and run until steady-state equilibrium composition is reached. In addition of those inputs, the kinetic model requires the definition of a set of **reactions**. This set is schematised in Appendix A and it includes only heavy particle collisions between neutral species present in the model of Koelman et al. [21]. Rate coefficients of these reactions are dependent on gas temperature via their Arrhenius form.
As a matter of fact, in order to understand **CO_2 splitting processes** it is important to consider not only electronic (or vibrational) excitation processes, but even interactions between neutrals that may play a role for longer times since neutral species tends to accumulate as a results of longer lifetimes with respect to excited species. Those interactions are considered separately in this kinetic model and their importance is highlighted in the following part. In particular, the principal reaction involving CO_2 dissociation is the following (3.3):

$$\mathbf{CO_2 + O \rightarrow CO + O_2} \tag{3.3}$$

The rate of this reaction increases with the increase of input energy of the system or with the increase of gas temperature. As a consequence, this means that atomic oxygen is a relevant species driving dissociation processes during pulse-phase. In fact, as it will be shown in Chapter 4, in microwave discharges, the collisions between CO_2 and O will be crucial to improve the CO_2 conversion.
Moreover some O atoms can recombine with CO via the following reaction (3.4):

$$\mathbf{O + CO + M \rightarrow CO_2 + M} \tag{3.4}$$

where **M** can be a third body like $\mathbf{CO_2}$, $\mathbf{O_2}$ and **CO**. As pointed out in Section (3.1.2), in order to improve energy efficiency and conversion, this backward recombination reaction involving CO and O has to be minimised in the study. Other relevant pathways of oxygen have to be mentioned. Those are mostly recombination processes that leads to a formation of O_2 and O_3 as described by (3.5) and (3.6) respectively.

$$\mathbf{O + O + M \rightarrow O_2 + M} \tag{3.5}$$

$$\mathbf{O + O_2 + M \rightarrow O_3 + M} \tag{3.6}$$

The relevance of those reactions is mostly due to the formation of O_2 and O_3, whose importance in CO_2 splitting and their equilibrium compositions have to be tested experimentally.

In this section, in order to find the equilibrium composition, different simulations were performed at fixed values of gas temperature in the range from 1000 to 6000 K for a constant pressure of 100 mbar, as mentioned before. The results of this comparison can be seen in Fig.(3.2) where the relative mole fraction of species are plotted as a function of different gas temperatures. In this plot the continuous lines refers to different simulations using CEA program, while dots refer to different simulations from the kinetic model used on PLASIMO.

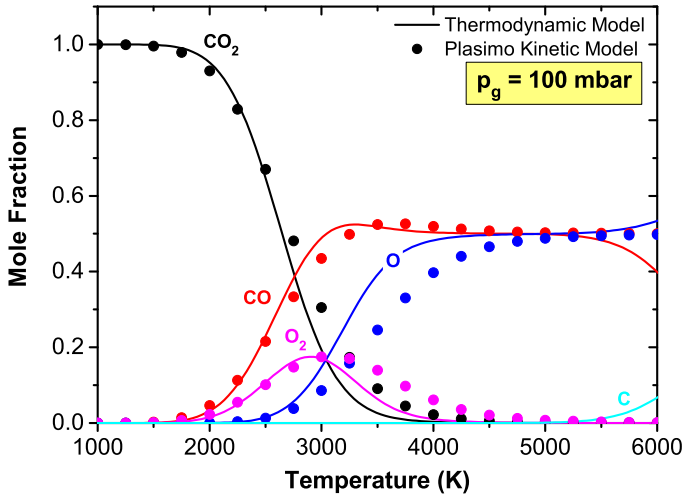

Figure 3.2: ***Calculated equilibrium composition of CO_2 mixture at 100 mbar as a function of gas temperature.***

While the equilibrium composition is directly calculated in the thermodynamic model, this is reached after a characteristic time in the kinetic model in which the reactions start to be in steady-state. This time is defined here as the *equilibration time*. Thus, the values of mole fraction of species deduced from PLASIMO and plotted in the graph before are the ones deduced after this typical equilibration time (i.e. see Fig.(3.3)). Species having mole fraction below the value of 10^{-3} were not plotted in Fig.(3.2). As can be seen in Fig.(3.2), the overall behaviour between the two models is generally comparable except some deviations mainly present in oxygen atomic and molecular species at higher temperatures (above 3000 K). Those deviations can mainly be attributed to missing backward reactions involving atomic oxygen, like the following (**??**):

$$\mathbf{O_2 + O \rightarrow O + O + O} \tag{3.7}$$

Reaction rate coefficient (3.7) is reported on [35] and [34] and it can contribute to the loss of O_2 and formation of O atoms mainly at higher temperatures. A more detailed discussion

on oxygen chemistry will be presented in Sec.(3.3) in order to point out relevant pathways. Furthermore, another relevant deviation it is present for temperatures above 5000 K in which atomic carbon starts to become relevant mostly due to thermal dissociation processes involving CO. This effect is not present in the kinetic model mostly because of the lack of balancing reactions involving C, C_2 and C_2O implemented. The importance of those species and the effect of carbon chemistry will be pointed out in Sec.(3.2) and it is relevant in order to describe thermal plasmas at higher gas temperatures (above 5000 K).

The **equilibration time** for different species is deduced from different simulations at different fixed temperature. In particular, the value for the CO species is shown in Fig.(3.3) as a function of different gas temperatures. This is the typical equilibration time even for the other species. Higher the temperature, lower the equilibration time, as shown in Fig.(3.3). This is essentially due to the increase of rate coefficients of the reactions that are strongly dependent on gas temperature. Anyway, as reported in [34], the fact that equilibration times are typically longer than residence times (that are of the order of some milliseconds) may lead the plasma composition to be not in steady-state if the plasma is thermal.

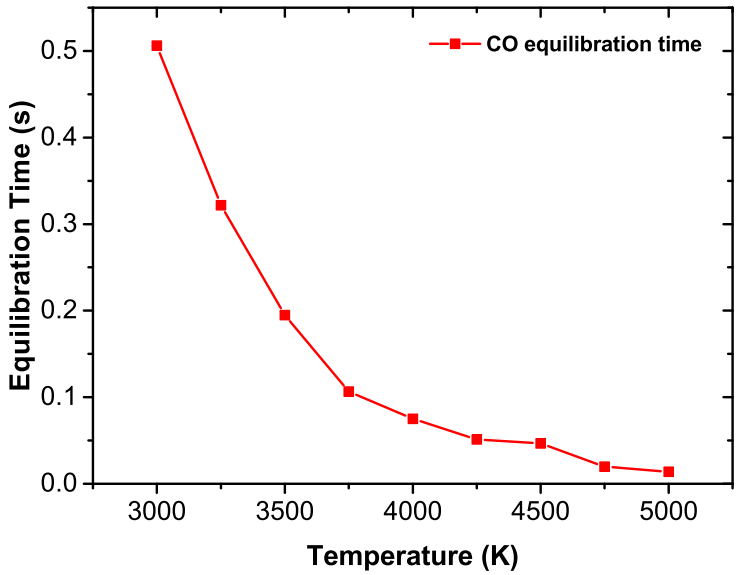

Figure 3.3: ***CO equilibration time considering for neutral collisions as a function of temperature.***

3.1.2 CO loss fraction

As mentioned in Sec.(3.1), one way to improve the CO_2 conversion is to minimise the reverse reaction between O and CO into CO_2. This section is dedicated to providing some possible answers about the way to handle this problem. In order to find a method to reduce the relevance of the recombination reaction aforementioned, different simulations were performed with PLASIMO to deduce the CO loss fraction. In these simulations, a constant profile of gas temperature is imposed until the composition reach a steady-state and then suddenly the temperature is decreased in time to 300 K. The variation of temperature in time determines the so called **cooling rate** and five different values of cooling rates were defined in the range between 10^4 and 10^8 K/s. Higher the cooling rate, faster the plasma cools down to room temperature. In these simulations, the CO loss fraction is deduced as the percentage value of CO lost after the temperature dropped to 300 K with a specific cooling rate.

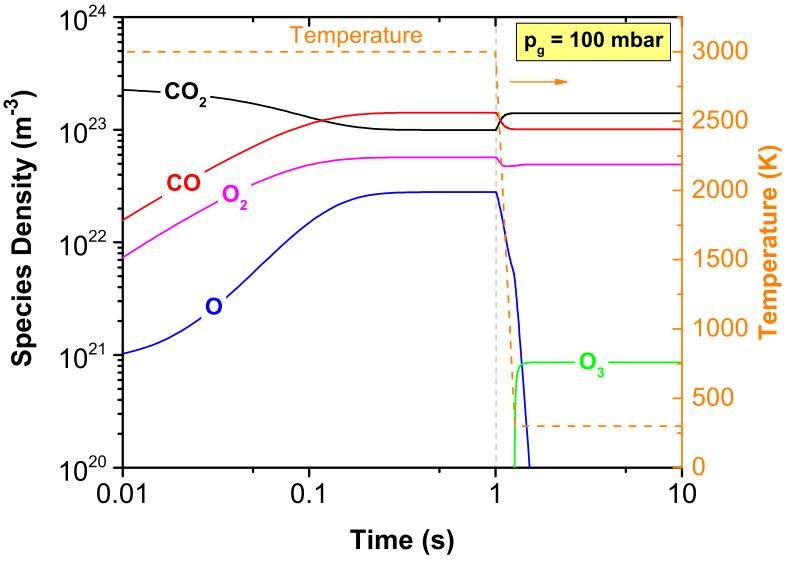

Figure 3.4: ***Densities of dominant neutral species under imposed temperature profile with a cooling rate of 10^4 K/s.***

The results of one of these simulations can be seen in Fig.(3.4). In this case, the temperature was kept constant at 3000 K until 1 s, when all the composition reach a steady-state. Dominant species like **CO**, $\mathbf{O_2}$ and **O** increase due to a dissociation processes involving $\mathbf{CO_2}$, as the one described by reaction (3.3). On the contrary, during relaxation phase (after 1 s), the atomic oxygen density abruptly decreases. This effect is mainly due to the drop of temperature that increases the rate of 3-body recombination reactions between $\mathbf{O_2}$ and **O**, leading to the formation of $\mathbf{O_3}$ as described by (3.6). Moreover, oxygen atoms can recombine into $\mathbf{O_2}$ via reaction (3.5). These effects suggest a first consideration:

> Lowering the gas temperature during pulsed-phase experiments can lead to a formation of $\mathbf{O_2}$ and $\mathbf{O_3}$ reducing the density of O atoms, which may prevent the recombination reaction (3.4) between **O** and **CO** to happen and thus improve $\mathbf{CO_2}$ conversion.

Further experimental investigation is needed to determine the equilibrium composition of O_2 and O_3. In particular, as described in [18], experimental measurements of O_3 density

would be fundamental to understand the balance of O_2 and O_3 in a CO_2 discharge. Further considerations about the effect of gas temperature during pulsing are discussed in Chapter 4.

From the same calculations performed for different cooling rates, the **CO loss fraction** was deduced, as described in the first part of this section. The percentage of CO lost for different cooling rates can be seen in Fig.(3.5a) for different initial values of gas temperatures and a fixed pressure of 100 mbar. As stated in the previous consideration, a lower gas temperature can suppress backward recombination reactions involving CO to happen leading to a lower percentage of CO lost during cooling processes. Furthermore, as can be seen at 3000 and 4000 K, higher the cooling rates lower the CO fraction lost. This indicates the need of fast quenching to happen since only at low temperatures reaction (3.4) is effectively suppressed. The calculated fraction of CO loss is clearly dependent on the initial value of gas temperature assumed due to the different equilibrium compositions between the species reached in steady-state. In fact, some species, like oxygen, are effectively dependent on temperature variations as will be shown in Sec.(4.1). Since CO losses are directly related to **CO_2 formation** by (3.4), further experimental investigations may highlight the effect of fast temperature relaxation in thermal plasmas during afterglow phase.

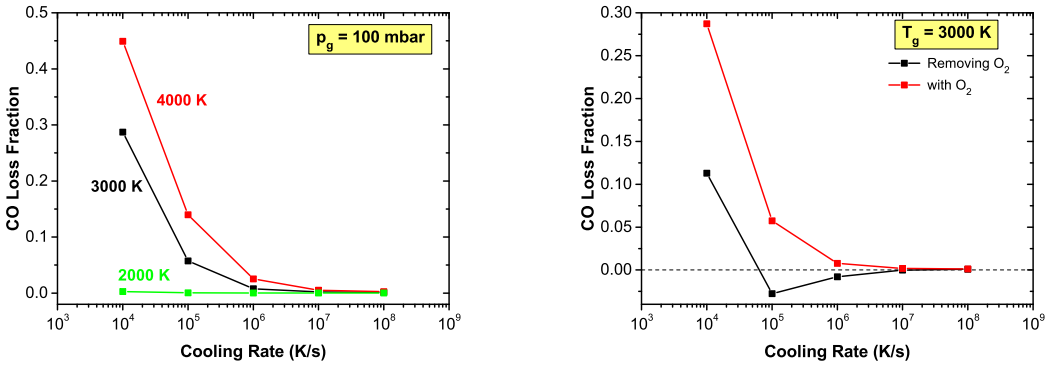

(a) CO loss fraction as a function of cooling rates.

(b) Effect of 2/3 removal of O_2 removal in CO losses.

Figure 3.5: ***CO loss fraction at different cooling rates: effect of fast quenching (left) and effect of removal of molecular oxygen before the cooling (right). In both cases a pressure of 100 mbar is assumed.***

Another way to reduce the effect of the recombination reaction (3.4) is to reduce the presence of O atoms (or O_2) available in the system, so there are not enough reactants available for the reaction to happen [36]. In Fig.(3.5b) the results of removing reactants to prevent recombination to happen is shown by studying the effect on the CO loss fraction for different cooling rates at an initial temperature of 3000 K. For these calculations, different simulations were performed removing 2/3 of the O_2 density after equilibrium conditions were reached. The CO loss fraction deduced after cooling are then compared with respect to the normal condition (the red line in Fig.(3.5b)). As can be seen from the graph, lower CO values of loss fraction are deduced when O_2 is removed from the mixture. Negative values of loss fraction obtained correspond to CO formation after cooling and are mostly due to CO_2 conversion that happens even for longer times when the temperature drops. Experimentally, the removal of O atoms or O_2 can be addressed essentially in two ways:

1. Addition of catalytic interaction (i.e. for example adding CH_4 or H_2) faster than the recombination reaction between CO and O.

2. Utilisation of solid oxide electrolyser cell (SOEC) in combination with a plasma technology in a hybrid reactor in order to capture O_2 in the plasma setup that can possibly transported away from the plasma mixture.

The first method was mainly studied numerically and experimentally by Aerts et al. [36] which describe the addition of H_2 and CH_4 leading to O_2 trapping mechanism. The second one, was performed recently with an experimental investigation by Mori and Tun [37], where they show an increase of CO_2 conversion up to 80% by removing oxygen on an hybrid DBD+SOEC reactor. However, this technology has the drawback of utilising high temperature and a limited low energy efficiency of 0.17% can be achieved, suggesting that further experimental investigation is needed for removing O_2 efficiently and improving CO_2 conversion. To summarise, in this section the effect of CO loss fraction was studied using a kinetic model implemented on PLASIMO. Focusing on neutral collisions it is possible to deduce a second consideration:

CO loss fraction can be minimised using **higher cooling rates** ($\geq 10^6$ K/s), thus lowering the rate of (3.4), or by removing reactants like $\mathbf{O_2}$. The advantage of this second method is that it can provide higher $\mathbf{CO_2}$ **conversion** at lower cooling rates.

3.2 Hints on carbon chemistry

In this section, the chemistry involving C and C_2 present in the model of Koelman at al. [21] is discussed. In particular, the following questions will be addressed:

- Which pathways lead to C-atoms increase in high temperature conditions?
- What is the role of C_2 chemistry and its relations to heavy particle species?

Suggestions for Question 1: From thermodynamic calculations (i.e. see Fig.(3.2)), it was already pointed out that C atoms are present in high temperature (above 5000 K) plasmas. In Koelman model, the main neutral reactions leading to C-atoms losses and CO production are the following (3.8) and (3.9), whose rates are taken from [38]:

$$\mathbf{C + CO_2 \rightarrow CO + CO} \tag{3.8}$$

$$\mathbf{C + O_2 \rightarrow CO + O} \tag{3.9}$$

Here some additional reactions not included in Koelman model are suggested that will take better into account the carbon dynamics. Studies on low temperature carbon nanofibers [39] suggest that disproportionation reaction (3.10) may be thermodynamically favorable in low temperature plasmas:

$$\mathbf{CO + CO \rightarrow CO_2 + C} \tag{3.10}$$

This reaction may be relevant in afterglow processes that lead to CO_2 formation due to relaxation. Moreover, reaction like (3.11) is found to be relevant in the temperature range between 10 and 8000 K:

$$\mathbf{C_2 + O \rightarrow CO + C} \tag{3.11}$$

Reaction rate coefficient of (3.11) is reported in [40] from a theoretical study of a molecular synthesis in interstellar clouds. Net result of reactions (3.10) and (3.11) is the decrease in C_2 density and the corresponding formation of C-atoms and CO_2.

Suggestions for Question 2: Experimental studies on hydrocarbon discharges and combustion flames by emission spectroscopy (OES) reveal the most prominent presence of Swan Bands ($d^3\Pi_g \rightarrow a^3\Pi_u$) of C_2, but uncertainties are still present on the influence of heavy particle interactions of emission from C_2 molecules. According to [39] and [41], emission intensity of C_2 molecules is strongly related with the presence of C_2O. In particular, in Koelman model, presence of $\mathbf{C_2O}$ is related to the following three reactions:

$$\mathbf{C + CO + M \rightarrow C_2O + M} \tag{3.12}$$

$$\mathbf{O + C_2O \rightarrow CO + CO} \tag{3.13}$$

$$\mathbf{O_2 + C_2O \rightarrow CO_2 + CO} \tag{3.14}$$

Reaction (3.12) leads to formation of C_2O, while (3.13) and (3.14) are the prevalent sink terms. From these reactions, it is possible to deduce the C_2O concentration via the relation (3.15):

$$[\mathbf{C_2O}] = \frac{k_{3.12} \cdot [\mathbf{C}][\mathbf{CO}][\mathbf{M}]}{k_{3.13} \cdot [\mathbf{O}] + k_{3.14} \cdot [\mathbf{O_2}]} \tag{3.15}$$

where $k_{3.12}$, $k_{3.13}$ and $k_{3.14}$ are reaction rate coefficient for (3.12), (3.13) and (3.14) respectively. This relation suggest that reduction of C_2O is mostly due to increase in O density when O_2 is increased. Thus, according to the model, higher concentration of O (or O_2) leads to enhancement of emission from C_2 molecules. Correlation between emission from $3p^5P$ oxygen level and $d^3\Pi_g$ state of C_2 has been recently experimentally observed from measurements of optical emission spectroscopy [42]. Moreover, according to (3.15), higher the CO concentration higher the presence of C_2O, showing that CO density and C_2 emission are thus related. Further experimental and theoretical investigations are needed to highlight production mechanisms of C_2 emission. For the sake of completeness, two more pathways has to be mentioned:

$$\mathbf{C + C + M \rightarrow C_2 + M} \tag{3.16}$$

$$\mathbf{C + C_2O \rightarrow C_2 + CO} \tag{3.17}$$

Effects of reactions (3.16) and (3.17) are studied in the framework of MW discharges [41] to explain the production of metastable C_2 levels and the origin of high-pressure bands. Analogous studies for determining the relevant pathways leading to Swan Bands will highlight the contribution of the reactions aforementioned. From this section, the following consideration can be deduced:

> Higher the oxygen (i.e. O-atoms or O_2 molecules) concentration, lower the C_2O density. Furthermore, since emission from C_2 molecules is supposed to be due to the presence of C_2O, oxygen dynamics would influence emission intensities.

Oxygen dynamics appears to be relevant driving not only dissociation processes of CO_2, but even emission from excited molecules. Thus, in the following section particular attention will be paid on the pathways governing oxygen chemistry.

3.3 Hints on oxygen chemistry

As pointed out in Sec.(3.1) and (3.2), oxygen chemistry plays a key role in driving dissociation processes of CO_2, but better understanding is needed to highlight conditions and relevant reactions. In order to do that, an oxygen plasma model was implemented on PLASIMO based on

the reaction set taken from [21] and tested against the global model developed by Kemaneci et al. [43] that was validated experimentally, in order to highlight the relevant reaction and species in an **oxygen discharge**. This comparison is aimed to answer the following questions:

- What are the dominant species in a pure oxygen discharge?
- In which timescales their evolutions happen?

In order to understand that, the effect of a square power pulse was investigated on both chemistries and is presented in the following.[1]

The **input chemistry** datasets are discussed below briefly in order to understand differences and relevant reactions implemented. The complete dataset of reactions included in the Koelman model can be found in Appendix A, while here the most relevant processes are summarised:

Note: In this section the notation **O** for atomic oxygen always refers to the ground state species $\mathbf{O}(^3\mathbf{P})$. When other different electronic excited states will be taken into account a different notation specifying the excited state will be used, while vibrationally excited states are not considered in both models.

Electron Impact Processes Cross section for *electronic excitation* of **molecular oxygen** from ground state in the model of Koelman et al. [21] are mostly taken from [24], those processes include:

$$\mathbf{e^- + O_2 \rightarrow e^- + O_2(a^1\Delta_g)} \tag{3.18}$$

$$\mathbf{e^- + O_2 \rightarrow e^- + O_2(b^1\Sigma_g^+)} \tag{3.19}$$

where $\mathbf{O_2(a^1\Delta_g)}$ and $\mathbf{O_2(b^1\Sigma_g^+)}$ refer to the first and second electronic excited states at 0.977 and 1.627 eV respectively. Higher electronic states are not included in this model. At high power density, if O atom wall recombination is negligible, the O atom density may be dominant. The latter is mainly generated by *electron impact dissociation* of O_2 (3.20) whose cross sections are taken from Itikawa database [46].

$$\mathbf{e^- + O_2 \rightarrow e^- + O + O} \tag{3.20}$$

Reaction (3.20) assumes that dissociation contributions arises mainly from fragments distribution that are consistent with 6 eV states ($\mathbf{c^1\Sigma_u^1}$, $\mathbf{A'^3\Delta_u}$ and $\mathbf{A^3\Sigma_u^+}$) to $\mathbf{O}(^3\mathbf{P})$+$\mathbf{O}(^3\mathbf{P})$ atoms. Other relevant processes to be mentioned are *ionization* and *dissociative attachment*, whose cross sections are taken from [24] and are described by (3.21) and (3.22) respectively:

$$\mathbf{e^- + O_2 \rightarrow 2e^- + O_2^+} \tag{3.21}$$

$$\mathbf{e^- + O_2 \rightarrow O^- + O} \tag{3.22}$$

Electron impact reaction with **atomic oxygen** includes mainly ionization (3.23) :

$$\mathbf{e^- + O \rightarrow 2e^- + O^+} \tag{3.23}$$

[1] The aim of this section is not to discuss a complete study on oxygen plasma discharges, but to highlight differences and principal pathways in presence of oxygen datasets. For other complete studies it is suggested to look at [33], [44], [23] and [45].

In this model, *electronic excitation* to higher O-states is not included. Although a complete set of cross sections for electron impact processes involving **ozone** does not exist [23], the ones included in the model of Koelman are mostly taken from [47]. Those include mostly processes like *dissociative attachment* and *dissociation* into O and O_2. Electronic excited states of O_3 are not included in this model since either weakly bound or dissociative.

Neutral Processes Neutral processes included are mainly interaction between O, O_2 and O_3. Those processes include *oxygen recombination* into O_2 and O_3 as described previously from (3.5) and (3.6). According to [44], process (3.5) is exothermic by some 5 eV, thus several electronic excited states can be a product of this reaction. In this work, the simplified approach was chosen to include only the single net effect of formation of O_2 in the ground state. Ozone can also react with oxygen mainly through reaction (3.24):

$$\mathbf{O_3 + O_2 \rightarrow 2O_2 + O} \tag{3.24}$$

Interaction between electronically excited states of O_2 is not directly included in the model. As discussed in Chapter 2, the form used for the expression of the rate coefficients of *heavy particles* interactions is of the Arrhenius type, assuming the species have a Maxwell-Boltzmann distribution of energy with a common temperature.

Charged Species One of the most important processes involving charged particles is the following *mutual neutralization* (3.33):

$$\mathbf{O^- + O_2^+ \rightarrow O + O_2} \tag{3.25}$$

Reaction rate coefficients of those processes are mostly taken from Gudmundsson et al. [48] and Beuthe at al. [49].

Main Input Differences This part discuss the main differences present in the chemistry between the model of Koelman et al. [21], discussed above, and the model of Kemaneci et al. [43]. It is worth noticing here that the Kemaneci model was completely built to model a MW oxygen discharge and to benchmark the results against experiements, thus a more complete set of reactions between species is included, while in the original chemistry of Koelman, especially interactions between CO and CO_2 (even including vibrational states) is taken into account. This comparison, however, is useful to understand possible limitations and improvements for future CO_2 global models taking into account only oxygen chemistry aforementioned.

The **species** considered in both models are summarised in Tab.(3.2):

Table 3.2: ***Species considered in Koelman and Kemaneci oxygen model.***

Species Considered		
	Koelman Model	**Kemaneci Model**
Neutrals Ground State	$O(^3P)$, O_2, O_3	$O(^3P)$, O_2, O_3
Electronically Excited	$O_2(a^1\Delta_g)$, $O_2(b^1\Sigma_g^+)$	$O(^1D)$, $O_2(a^1\Delta_g)$, $O_2(b^1\Sigma_g^+)$, $O_2(A^3\Sigma_u^+, A^3\Delta_u, c^1\Sigma_u^-)$
Charged Species	e^-, O^+, O_2^+, O_4^+, O^-, O_2^-, O_3^-, O_4^-	e^-, O^+, O_2^+, O^-, O_2^-, O_3^-

The main difference that can be seen from Tab.(3.2) is the presence of $\mathbf{O(^1D)}$ states and lumping of electronically excited states of molecular oxygen as $\mathbf{O_2(A^3\Sigma_u^+, A^3\Delta_u, c^1\Sigma_u^-)}$ that are included in the Kemaneci model. Furthermore, in Koelman model, $\mathbf{O_4^+}$ and $\mathbf{O_4^-}$ ions are present even if they are not dominant both in discharge and post-discharge conditions. The differences in the species considered suggest the presence of different **pathways** in the chemistry model of Kemaneci. The main differences are reported below.

1. As considered by [50], *electron impact dissociation* of O_2 is faster through the following channel that leads to the formation of $\mathbf{O(^1D)}$:

$$\mathbf{e^- + O_2 \rightarrow e^- + O + O(^1D)} \tag{3.26}$$

   According to crossed beam experiments, the channel of dissociation proceeds through optically allowed electronically excitation of O_2 ($\mathbf{B^3\Sigma_u^-}$, $\mathbf{B'3\Sigma_u^-}$ and $\mathbf{2^3\Pi_u}$), each of these excited states then dissociate to form $\mathbf{O(^3P)}$ and $\mathbf{O(^1D)}$ atoms. This channel is faster than the only process (3.20) due to 6 eV states included in the model of Koelman

2. Interactions between electronically excited states and ground states species are widely included in the model of Kemaneci. Those interactions include, for example, processes like *charge exchange*:

$$\mathbf{O^- + O_2(a^1\Delta_g) \rightarrow O + O_2^-} \tag{3.27}$$

3. *Radiative processes* that lead to de-excitation of O_2 electronical levels are included in Kemaneci model, like the following:

$$\mathbf{O_2(A^3\Sigma_u^+, A^3\Delta_u, c^1\Sigma_u^-) \rightarrow O_2} + \hbar\nu \tag{3.28}$$

4. In addition to (3.39), reaction (3.29) is included in the model of Kemaneci. This reaction leads to the formation of O_3

$$\mathbf{O_2 + O + O \rightarrow O + O_3} \tag{3.29}$$

In order to model an oxygen MW discharge, both models were run on PLASIMO. A constant input power of 250 W were imposed until 50 μs, then switched off to zero. The plasma is supposed to be confined in a volume of radius R = 7.5 mm and total axial length L = 144 mm. The gas temperature is fixed and set to 2000 K, while the time evolution of the electron temperature is determined from the electron energy balance equation. The electron density is not computed from the continuity equation, but calculated from the quasi-neutrality condition. In both models, heat transport, flow and wall interactions are neglected. A comparison between those two models can be seen from Fig.(3.6) where time resolved particle densities are shown.

- *During the pulse*, in both models, the evolution of **neutral species** is mostly determined by electron impact reaction leading to dissociation of O_2. In fact, processes like (3.18), (3.19) and (3.20) contribute to the steep increase of $\mathbf{O_2(a^1\Delta_g)}$, $\mathbf{O_2(b^1\Sigma_g^+)}$ and $\mathbf{O}$ respectively. **Ion species**, like $\mathbf{O^+}$ that is dominant during the pulse, are mainly produced by ionization processes, like (3.21).
- *After the pulse*, due to the drop of electron temperature, ion species and electrons tend to vanish. Evolution of electron density is mainly determined by the evolution of the dominant ion $\mathbf{O_2^+}$.

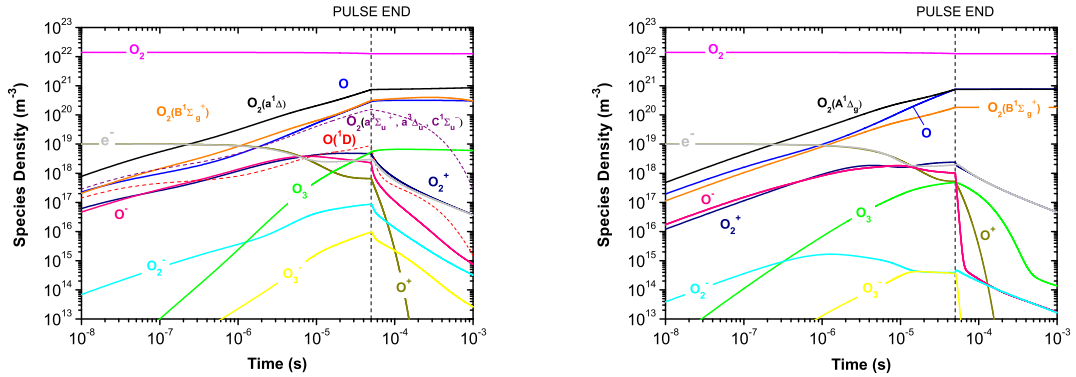

(a) Kemaneci oxygen model. **(b)** Koelman model.

Figure 3.6: ***Comparison of time evolution of densities between Kemaneci model (left) and Koelman model (right) in a power pulsed discharge of 50 μs at 250 W. Gas temperature is fixed at 2000 K and an initial pressure of 2.76 mbar is used.***

Important **differences** between the two models have to be mentioned and can be summarised by three statements and discussed in the following:

- In Koelman model, **O**-atom density is higher during the pulse-phase from 10^{-6} s (Fig.(3.6b)) with respect of Kemaneci model
- $\mathbf{O(^1D)}$ and $\mathbf{O_2(A^3\Sigma_u^+, A^3\Delta_u, c^1\Sigma_u^-)}$ are not taken into account in Koelman model. Better understanding is needed to highlight the net effect of including those species
- $\mathbf{O_3}$ density appears to be constant in the afterglow of Kemaneci model (Fig.(3.6a)), while it drops in Koelman (Fig.(3.6b))

O densities comparison Larger increase of O atomic density in Koelman model can be attributed to the higher value of electron temperature reached during the pulse. Furthermore, as will be discussed in Sec.(4.1) of Chapter 4, O-atom density is particular sensitive to variations of electron temperature. As can be seen in Fig.(3.7), in the pulse-phase of Koelman model, electron temperature reaches a peak value around 4 eV, then quickly drops to gas temperature in 0.1 μs the drops of electron density in around 1 ms, together with the dominant ion O_2^+. Steep increase of electron temperature in the model may be due to a low electron density or to an improper balance of inelastic processes included in the model.

In particular, reaction (3.30) is the main source of production of oxygen in the ^{3}P ground state, as discussed previously:

$$\mathbf{e^- + O_2 \rightarrow e^- + O + O} \tag{3.30}$$

At the same time, the second relevant contribution (according to the net rate of reactions involved) is the following dissociative attachment:

$$\mathbf{e^- + O_2 \rightarrow O^- + O} \tag{3.31}$$

As expected, in Koelman model *electron impact reactions* drive the dissociation of the main species during pulse-phase. However it is worth noticing here that other reactions have an important contribution to the dynamics, those are mainly the following *charge exchange* and *mutual neutralization*:

$$\mathbf{O^+ + O_2 \rightarrow O + O_2^+} \tag{3.32}$$

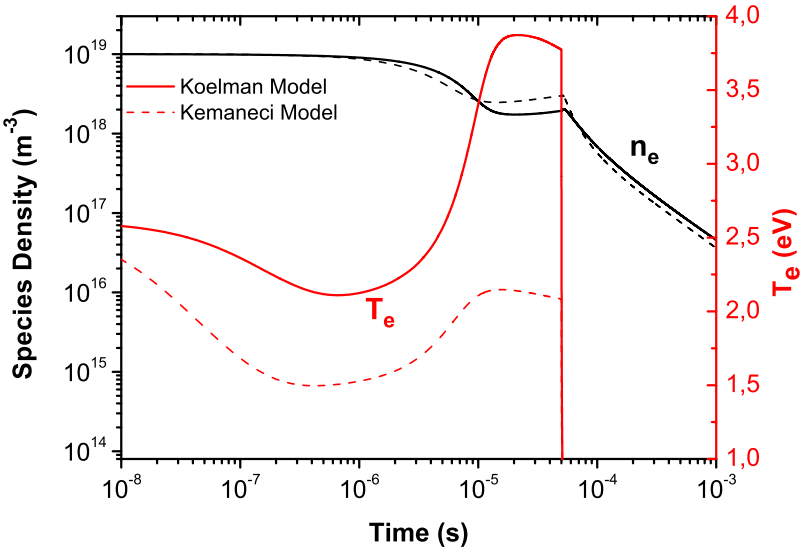

Figure 3.7: ***Time evolution of electron densities and temperatures calculated from Koelman and Kemaneci model.***

$$\mathbf{O^- + O_2^+ \rightarrow O + O + O} \tag{3.33}$$

In the same time period during pulse-phase, different pathways are present and become relevant in **Kemaneci model**. Those pathways does not involve only electron impact reactions, but the presence of $\mathbf{O(^1D)}$ is particularly relevant for oxygen dynamics. The main difference here is that electron impact dissociation of O_2 proceeds faster through the following channel leading to the formation of $O(^1D)$ whith respect to the process (3.30):

$$\mathbf{e^- + O_2 \rightarrow e^- + O(^1D) + O} \tag{3.34}$$

This process balances together with (3.32) and (3.33) between 10^{-7} and 10^{-4} s. Moreover, at the end of the pulse, interaction (3.35) between O_2 and $O(^1D)$ is dominant. The net result is a formation of O atoms in the ^3P state, but with a slower time with respect Koelman model.

$$\mathbf{O_2 + O(^1D) \rightarrow O_2 + O} \tag{3.35}$$

The following consideration can be deduced, considering oxygen dynamics:

> During pulse-phase, reaction (3.34) was demonstrated to be one of the fastest channel of oxygen production with respect to reaction (3.30). O atom production in the afterglow is most likely to be due to interaction (3.35) between O_2 and $O(^1D)$.

Electronic states of O and O_2 As seen from the discussion of the previous statement, production of $O(^1D)$ is mainly due to electron impact reaction with O_2 happening until 10^{-5} s. Here the effect of this O-metastable state and higher electronically excited states on the $\mathbf{O_2}$ **dynamics** are presented. The energy level diagram of O_2 species is presented in Fig.(3.8) based on a study of Thorsteinsson at al. [51]. In particular, in both models, electron impact excitations to $\mathbf{O_2(a^1\Delta_g)}$ and $\mathbf{O_2(b^1\Sigma_g^+)}$ states are the dominant processes involving sinks of O_2 during the pulse. However, while in Koelman formation of O atoms due to (3.30) is one of

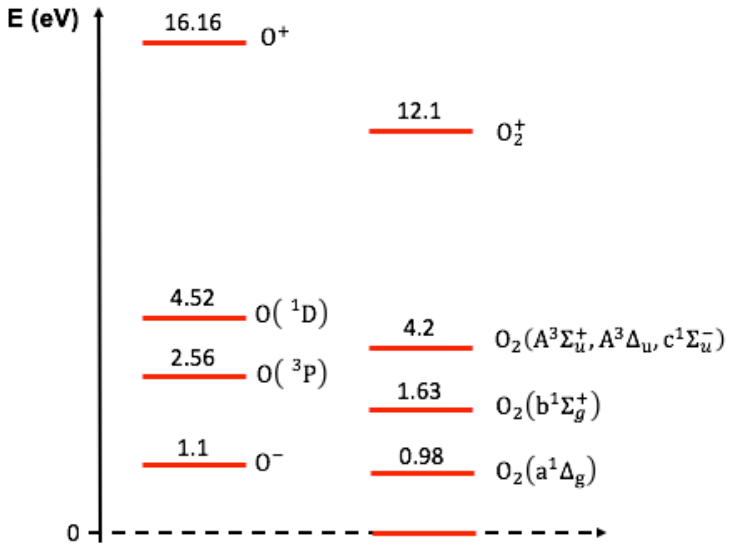

Figure 3.8: ***Energy levels of O_2 plasma species considered in Kemaneci model.***

the fastest channel, in Kemaneci model *electronic excitation reactions* to 4.2 eV metastable states is becoming relevant:

$$\mathbf{e^- + O_2 \rightarrow e^- + O_2(A^3\Sigma_u^+, A^3\Delta_u, c^1\Sigma_u^-)} \tag{3.36}$$

During afterglow, O_2 losses in Koelman model proceed with slower rate due to reaction (3.18) that is is still the dominant one. On the contrary, Kemaneci model presents a much more complex dynamics involving the presence of O_3. The main difference is that reaction like (3.18) looses importance around 10^{-3} s and *heavy particle collisions* become important sources of O_2, like it is shown by the pathways involving (3.37) followed by (3.38):

$$\mathbf{O_2 + O_2(A^3\Sigma_u^+, A^3\Delta_u, c^1\Sigma_u^-) \rightarrow 2O_2(b^1\Sigma_g^+)} \tag{3.37}$$

$$\mathbf{O_2(b^1\Sigma_g^+) + O_3 \rightarrow 2O_2 + O} \tag{3.38}$$

These considerations leads to the following conclusions:

> At high electron temperatures during pulse-phase, electronic excitation of O_2 is the dominant mechanism causing O_2 dissociation. Furthermore, presence of higher molecular excited states of oxygen can enhance the production of O_2 in the afterglow, mainly through interaction between O_3. Thus, detection of ozone species seems relevant in order to understand the principal pathways happening in the afterglow.

Ozone kinetics in the afterglow

Fig.(3.9) shows the evolution of densities of species with relative slow kinetics (O, $O_2(a^1\Delta_g)$, $O(^1D)$, O_3 and $O_2(A^3\Sigma_u^+$, $A^3\Delta_u$, $c^1\Sigma_u^-)$). Moreover, from this plot we can deduce that the time evolution of these species is long compared to the time in which the plasma is excited. This graph suggest that their densities may be relevant during afterglow. As a consequence, the chemistry during afterglow then consists predominantly of reactions between those species or it is mediated by other states that may appear transiently. In particular, comparison

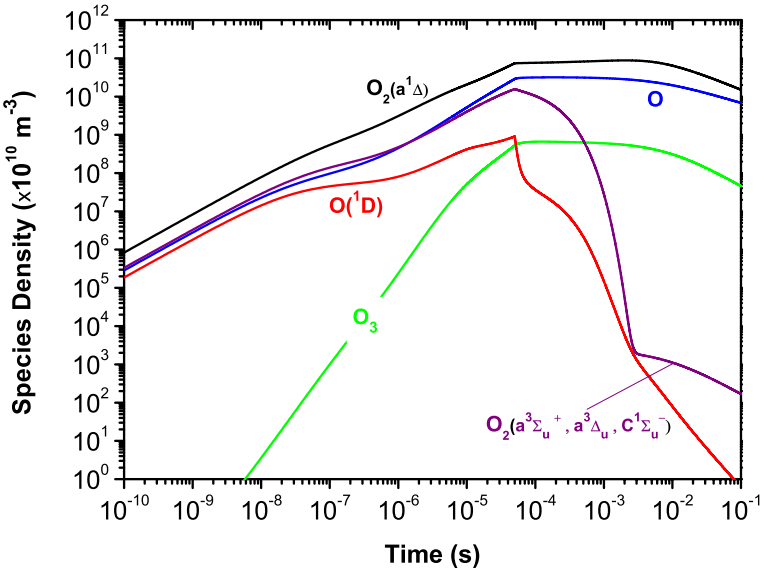

Figure 3.9: ***Densities of 5 species with relative slow kinetics, from Kemaneci model. Densities of those species fall slowly during afterglow, suggesting that their contribute in post-discharge conditions may be relevant.***

between Fig.(3.6a) and (3.6b) suggests that different pathways play a role in ozone production during afterglow. Since this species can enhance O_2 formation, as mentioned before, a correct implementation of **ozone dynamics** seems to be relevant for reactions happening in the afterglow.

During the pulse, in both models the increase of O_3 production is mainly due to the following (3.39):

$$\mathbf{O^- + O_2 \rightarrow O_3 + e^-} \tag{3.39}$$

Furthermore, in Kemaneci model, electronically excited states can enhance O_3 production at the end of the pulse via reaction (3.40):

$$\mathbf{O^- + O_2(a^1\Delta_g) \rightarrow O_3 + e^-} \tag{3.40}$$

The main differences between the two models, can be seen in the *afterglow-phase*. In Koelman, in fact, sinks of O_3 are mainly due to reaction (3.41):

$$\mathbf{O_3 + M \rightarrow O_2 + O + M} \tag{3.41}$$

On the contrary, in Kemaneci model, the dominant process regarding O_3 is mostly the source term reaction :

$$\mathbf{O_2 + O + O \rightarrow O_3 + O} \tag{3.42}$$

This reaction aforementioned is indeed not included in the model of Koelman. From these considerations, the following conclusion can be deduced:

Ozone is one neutral radical species that is likely to be important in the afterglow. In particular, when O-atoms density is large, three-body association reaction (3.42) is fast and leads to the production of O_3. Furthermore, quenching (3.38) by ozone with $O_2(b^1\Sigma_g^+)$

is fast and the density of $O_2(b^1\Sigma_g^+)$ remains small compared to the first electronically excited level of O_2.

As mentioned in [44], recent works [52] [53] suggest a more probably formation of O_3 in vibrationally excited states. These excited molecules are far more reactive than the ones in the ground state, in particular with oxygen atoms. This suggest that the net effect of those processes is a retardation of production of ozone. However, in the model considered here, a simplified approach was adopted neglecting the presence of vibrational levels. The relevance of this pathway has to be tested in future models and by experimental techniques.

CHAPTER 4

Analysis of CO_2 kinetic model

Focus of this Chapter is studying the state-to-state CO_2 kinetic model described in Chapter 2. Here a parametric study is presented, according to Sec.(2.3). First of all, steady-state calculations will be presented in order to study the dynamics of electrons that drives dissociation processes. Second, a reduced CO_2 model is run in pulsed mode in order to investigate the pulse and afterglow phases. Third approach will be the study of the full kinetic model in which electronically and vibrationally excited levels are included.

4.1 Steady-state calculations

For performing steady-state calculations, three important initial assumptions were made:

- For sake of simplicity, negative ions and excited states are *not* included: the first being a reasonable simplification, since negative ions will be seen to not influence relevantly CO_2 splitting processes. On the contrary, the effect of excited states will be discussed in Sec.(4.3).
- Gas temperature is fixed during all simulation time at a value of 600 K.
- Electron temperature and electron density are also fixed externally and not deduced from energy balance equation and quasi-neutrality condition respectively.

Sixteen different simulations have been run by fixing progressively the electron temperature at one value chosen between 1, 1.5, 2 and 2.5 eV for each different value of electron density assumed (i.e. chosen between 10^{18}, 10^{19}, 10^{20} and 10^{21} m^{-3}). The gas pressure is set at 1000 mbar, that determines an initial CO_2 density of $1.21 \cdot 10^{25}$ m^{-3} (at 600 K). Moreover, the initial neutral species densities are set at 10^{15} m^{-3}, while initial ion densities are deduced from previous running by fixing only the electron temperature until composition equilibrium is reached. All the simulations aforementioned were run until equilibrium is reached due to net balancing of reaction rates.

4.1.1 Influence of electron density

Results of calculations fixing electron temperature at 2 and 2.5 eV are shown in Fig.(4.1), where the steady-state equilibrium density of neutral species is plotted as a function of four fixed values of electron density. From those results the following observations can be deduced:

- **Statement 1:** n_e affects the increase of **O** and **C** atom densities (with almost linear dependence)
- **Statement 2:** Conversion of $\mathbf{CO_2}$ into **CO** is increased with increasing n_e
- **Statement 3:** At $n_e \geq 10^{20}$ m^{-3}, O-atom density exceed molecular oxygen density

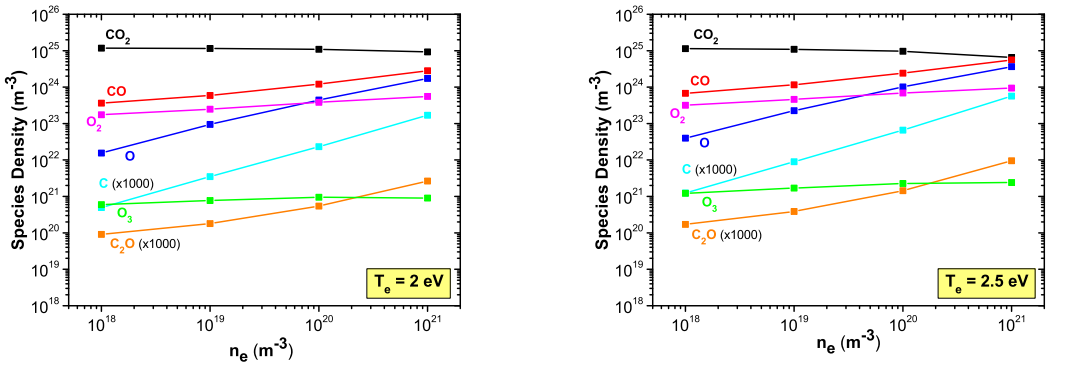

(a) Steady-state calculations at 2 eV. **(b)** Steady-state calculations at 2.5 eV.

Figure 4.1: ***Dependence of steady-state neutral densities on electron density, for fixed T_e at 2 eV (left) and 2.5 eV (right). An initial pressure of 1000 mbar was assumed together with a gas temperature of 600 K.***

Discussion of these observations is presented here, by looking at the reaction rates for production and destruction processes:

Statement 1 discussion Densities of atomic oxygen and carbon are shown to increase by three orders of magnitude in Fig.(4.1), for electron density going from 10^{18} to 10^{21} m^{-3}. Key processes for *O-production* are mainly electron impact dissociation of CO_2 (4.1) and O_2 (4.2):

$$\mathbf{e^- + CO_2 \rightarrow e^- + CO + O} \tag{4.1}$$

$$\mathbf{e^- + O_2 \rightarrow e^- + O + O} \tag{4.2}$$

C-production is mainly dominated by *dissociative ionization* (4.3) of CO_2:

$$\mathbf{e^- + CO_2 \rightarrow e^- + e^- + O_2^+ + C} \tag{4.3}$$

Even if 4 orders of magnitude lower than O-atoms density, carbon density is shown in Chapter 3 to play a relevant role in quenching processes between CO_2 and O_2 leading to formation of CO. Naturally, higher the electron density, greater the reaction rate of (4.1), (4.2) and (4.3).

Statement 2 discussion: Electron impact processes drive the CO_2 conversion through dissociation and/or ionization. In particular, even if conversion is limited by neglecting electronic and vibrational excitations, it is interesting to see which processes play a major

role. In these calculations, the rate of *dissociation* (4.1) is found to be around 5 orders of magnitude higher than *dissociative ionization* (4.4) and around 2 times more than *ionization* (4.5):

$$\mathbf{e^- + CO_2 \rightarrow e^- + e^- + CO^+ + O} \tag{4.4}$$

$$\mathbf{e^- + CO_2 \rightarrow e^- + e^- + CO_2^+} \tag{4.5}$$

In order to summarise, if we neglect electronic excitation, the following inequality governs electron impact processes that lead to CO_2 conversion at atmospheric pressure::

$$\mathbf{R_{diss} > R_{ioniz} > R_{diss\_ion}} \tag{4.6}$$

where R_{diss}, R_{ioniz} and R_{diss_ion} are the reaction rates for dissociation (4.1), ionization (4.5) and dissociative ionization (4.4) respectively.

Statement 3 discussion: As mentioned before, dissociation of CO_2 and O_2 lead to an enhancement of O-production with increasing electron density. Together with these processes, quenching (4.7) is also responsible of sinks of O_2 molecules that lead to the production of O-atoms with increasing electron density.

$$\mathbf{O_2 + C \rightarrow CO + O} \tag{4.7}$$

Moreover, three-body recombination of O-atoms through (4.8) and (4.9) is very sensitive to electron processes if O_2/O balance ratio is so strongly affected by n_e.

$$\mathbf{O + O + M \rightarrow O_2 + M} \tag{4.8}$$

$$\mathbf{O + CO + M \rightarrow CO_2 + M} \tag{4.9}$$

One idea to increase the overall conversion efficiency is to prevent those reactions to happen either by working at lower pressure where O_2 formation is decreased or by cooling down the plasma very fast (i.e. $\geq 10^6$ K/s) exploiting a nozzle effect.

Observations about carbon chemistry Studies by means of optical emission spectroscopy (OES) [54] detected strong emissions of C_2 Swan band, suggesting that atomic and molecular carbon may play a relevant role in CO_2 discharges. For this reason, a correct implementation of C_2 chemistry is necessary. In the present model, only the two reactions (4.10) and (4.11) are causes of sinks of C_2:

$$\mathbf{e^- + C_2 \rightarrow e^- + C + C} \tag{4.10}$$

$$\mathbf{e^- + C_2 \rightarrow e^- + e^- + C_2^+ + C} \tag{4.11}$$

Reaction (4.10) is the dominant channel that leads to C_2 splitting since its reaction rate is always higher than (4.10). Moreover, reactions (4.12) and (4.13) are the only sinks of the correspondent ion C_2^+:

$$\mathbf{e^- + C_2^+ \rightarrow C + C} \tag{4.12}$$

$$\mathbf{C_2^+ + C \rightarrow C_2 + C^+} \tag{4.13}$$

In particular, reaction (4.13) is the only source of C_2 molecules. Thus, by fixing electron density and temperature production and destruction processes of C_2 and C_2^+ are not balanced and will not lead to an equilibrium density. On the contrary, in pulsed calculations with lower electron density, the relative importance of (4.13) has seen to increase leading to source terms of C_2. These results suggest that a refined version of CO_2 model is needed to understand when C_2 chemistry may play a role. In this framework, implementation of reactions taken from astrochemistry [40] together with a coupled radiative model seem necessary to explain the strong molecular and atomic carbon emission.

Ions production Positive ions are also included in the model. These ions are plotted in Fig.(4.2) for a fixed electron temperature of 2 eV. Since also the electron density is fixed, quasi neutrality is not respected meaning that ionization processes continuously happen. From those calculations, it is possible to infer some informations about reaction rates of ions production in a CO_2 discharge.

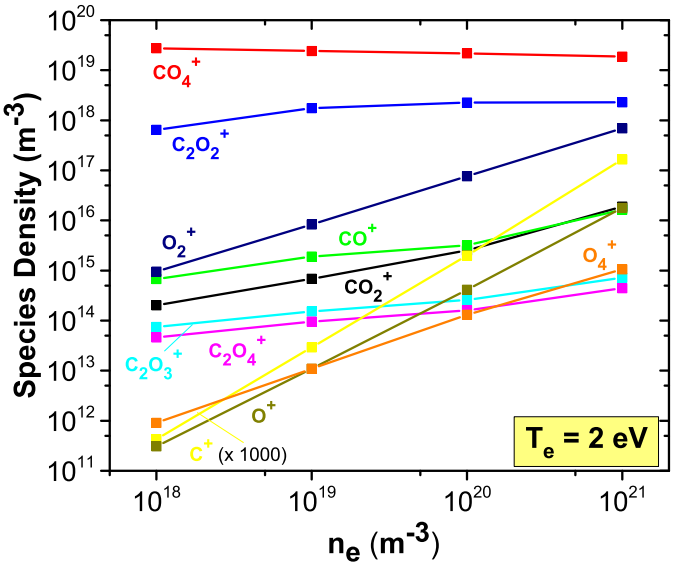

Figure 4.2: ***Dependence of ion steady-state densities on electron density at T_e = 2 eV. A pressure of 1000 mbar and T_g of 600 K was assumed.***

- Higher the n_e, more oxygen-based ions (i.e. O_4^+, O^+ and O_2^+) are produced. Densities of those ions seems to follow the inequality (4.14):

$$\mathbf{n_{O_2^+} > n_{O^+} > n_{O_4^+}} \tag{4.14}$$

Ionization processes with O_2 and O are the dominant sources of O_2^+ and O^+ respectively. However, the density of O_2^+ is higher than O^+ because of its lower ionization potential (i.e. 12.07 eV for O_2^+ against 13.62 eV for O^+, according to NIST). On the contrary, $\mathbf{O_4^+}$ ion is not produced from ionization processes since O_4 is not stable. Thus, its main production channel is the three-body reaction (4.15):

$$\mathbf{O_2^+ + O_2 + M \rightarrow O_4^+ + M} \tag{4.15}$$

Anyway, at atmospheric pressure, reaction rate of (4.15) is lower than ionization rates of O_2 and O that drive the formation of O_2^+ and O^+ respectively, meaning that O_4^+ it remains a negligible species.

- Density of $C_2O_3^+$ is slightly higher than $C_2O_4^+$ for the whole electron density range, while $C_2O_2^+$ density appears to be almost 4 orders of magnitude higher.

  Clusters of ions like $\mathbf{C_2O_2^+}$, $\mathbf{C_2O_3^+}$ and $\mathbf{C_2O_4^+}$ are related via the combination of the following pathways:

$$\mathbf{C_2O_4^+ + CO \rightarrow C_2O_3^+ + CO_2} \tag{4.16}$$

$$\mathbf{C_2O_3^+ + CO \rightarrow C_2O_2^+ + CO_2} \tag{4.17}$$

  Production of $C_2O_3^+$ is driven by reaction (4.16) that is followed by $C_2O_2^+$ production via reaction (4.17). This reaction chain is also observed in the following pulsed calculations.

- CO_4^+ is the dominant ion for the whole electron density range. This ion seems to decrease slightly with increasing electron density.

  According to theoretical studies on thermal plasmas [49], at $T_e \geq 9000$ K, $\mathbf{CO_4^+}$ is the dominant positive ion as a result of three-body reaction (4.18):

$$\mathbf{O_2^+ + CO_2 + M \rightarrow CO_4^+ + M} \tag{4.18}$$

  However, recent measurements in Bochum in He+CO_2 plasmas powered by an RF supply at atmospheric pressure, presents also high signal from $C_2O_2^+$ ion, with detected CO_2^+ and $C_2O_4^+$.

4.1.2 Influence of electron temperature

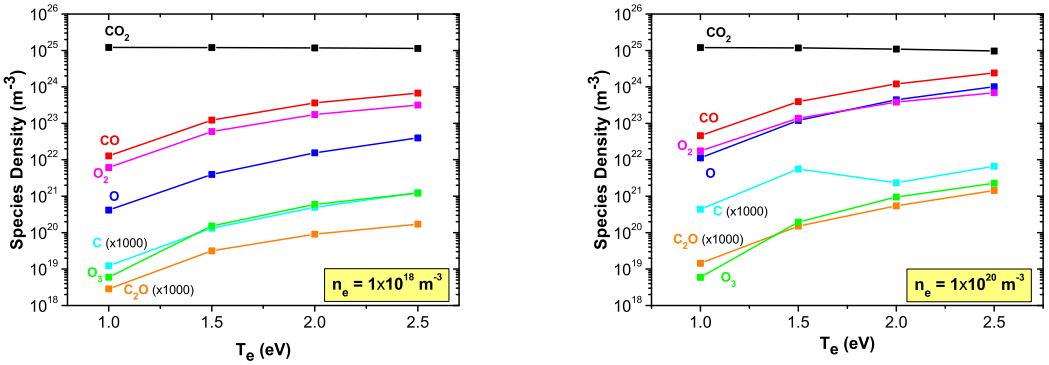

(a) Steady-state calculations at $n_e = 10^{18}$ m^{-3}. **(b)** Steady-state calculations at $n_e = 10^{20}$ m^{-3}.

Figure 4.3: ***Dependence of steady-state neutral densities on electron temperature, for fixed electron densities. Pressure of 1000 mbar and T_g of 600 K is considered.***

Fig.(4.3) shows the equilibrium densities of neutral species for different values of electron temperature and fixed electron density at 10^{18} and 10^{20} m^{-3}. In both plots, higher densities are achieved for higher electron temperature. This can be easily explained since cross sections of electron impact processes increase with electron temperature.

In Fig.(4.4) is shown the *equilibration time*[1] for CO species deduced from different simulations at different fixed values of electron density and temperature. The higher the electron temperature (or electron density), the lower the time for CO molecules to reach steady-state conditions. Values around 5 s are found at $n_e = 10^{19}$ m^{-3} and $T_e = 1$ eV, while it decreases to $2{\cdot}10^{-3}$ s for $n_e = 10^{21}$ m^{-3} and $T_e = 2.5$ eV. This is due to faster reactions that happens when

[1] As shown in Chapter 3, this is the time in which the species starts to become in equilibrium

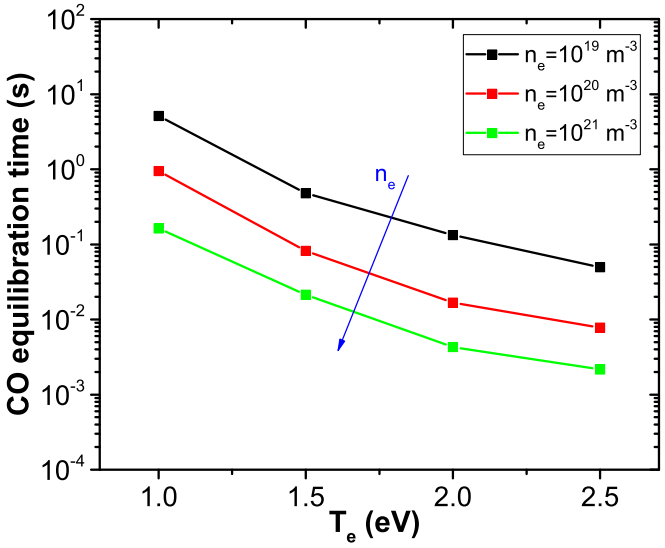

Figure 4.4: ***CO equilibration time for fixed values of electron density and temperature.***

electron temperature (or density) is increased. Typical values of electron density around 10^{19} m^{-3} and electron temperature of 2.5 eV were obtained in microwave discharges [54]. In these conditions, shorter timescales by optical emission spectroscopy are expected with respect the values reported here. This mismatch is mainly due to the missing excitation channels that are the dominant pathways in MW discharges.

Effect of electronically excited states

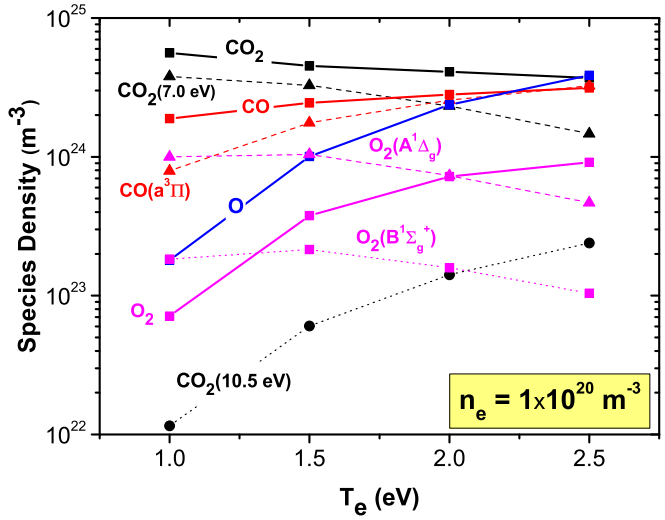

Figure 4.5: ***Equilibrium composition of dominant neutral species for fixed values of electron densities and temperature. A pressure of 1000 mbar was assumed, T_g of 600 K. Electronically excited states are here included in the calculations.***

Results of steady-state calculations including electronically excited states are reported in Fig.(4.5). In this scenario, electron-impact excitation dissociation (4.19) is seen to have the

strongest effect on CO_2 conversion.

$$\mathbf{CO_2} + \mathbf{e^-} \rightarrow \mathbf{CO_2(7eV)} + \mathbf{e^-} \tag{4.19}$$

In addition, four electronic excited states of **CO** are included but they do not have much effect, except the first one (i.e. $CO(a^3\Pi)$) whose population is enhanced while increasing the electron temperature, as expected. In addition, the presence of $\mathbf{O_2}$ excited states appears to be relevant for CO_2 dissociation. Further dissociation of O_2 creates O-atoms that can enhance the overall conversion rate. Moreover, excitation of O_2 metastable levels appears to lead population inversion. This fact suggest that some depopulation methods (i.e. radiation or detailed balancing) has to be included in the model.

4.1.3 Influence of gas temperature

Gas temperature is a crucial parameter in gaseous discharges since it determines the energy distribution of the heavy particles. As shown in Sec.(3.1.2), lowering the temperature in the afterglow with fast variations may affect positively the conversion efficiency. Moreover, according to [55], imposing a fixed gas temperature may be a strong limitation in MW discharges which are characterised by an higher temperature in the core of the discharge. In order to understand the role of gas temperature in the chemistry, steady-state calculations were performed by fixing the gas temperature at four different values (i.e. 300, 600, 1000 and 3000 K). Fig.(4.6) shows the equilibrium composition of neutral ground state species[2] for these different values of gas temperature, fixed electron density (i.e. at 10^{18} and 10^{20} m^{-3}) and fixed electron temperature at 2 eV.

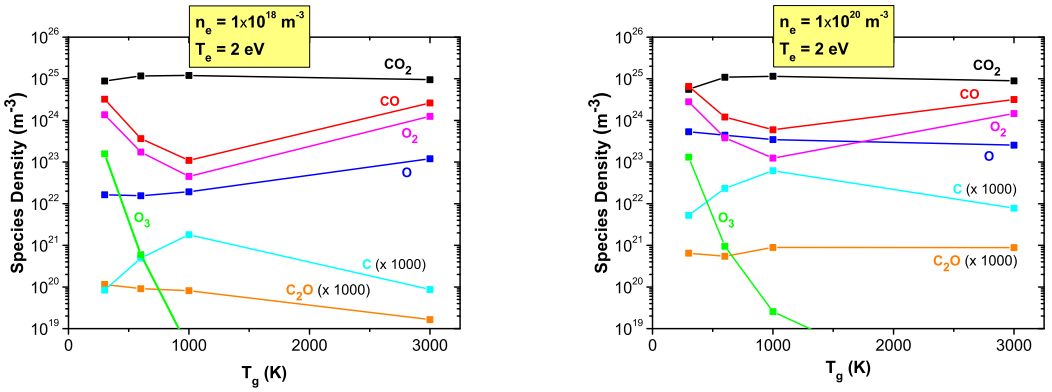

(a) Steady-state calculations at fixed $n_e = 10^{18}$ m^{-3} and $T_e = 2$ eV.

(b) Steady-state calculations at fixed $n_e = 10^{20}$ m^{-3} and $T_e = 2$ eV.

Figure 4.6: ***Dependence of steady-state neutral densities on gas temperature, for fixed n_e and T_e. Pressure of 1000 mbar is assumed and gas temperature of 600 K. Excited states are not included in these calcualtions.***

Assuming fixed electron temperature and density, the variation in the equilibrium composition for different gas temperatures is mainly due to neutral collisions whose rate coefficient is dependent on the gas temperature. Thus, analyzing the respective rates helps to infer the following considerations:

- Descreasing the gas temperature from 1000 K to 300 K leads to smaller three-body recombination rates (4.20) that form CO_2. In the same conditions, O_2 and O_3 are

[2]Note that here excited states are again neglected

produced via the enhancement of three-body reactions (4.21) and (4.22).

$$\mathbf{O + CO + M \rightarrow CO_2 + M} \tag{4.20}$$

$$\mathbf{O + O + M \rightarrow O_2 + M} \tag{4.21}$$

$$\mathbf{O + O_2 + M \rightarrow O_3 + M} \tag{4.22}$$

- At higher temperatures (i.e. $>$ 1000 K), O-atoms react back with CO_2 producing CO and O_2 again via reaction (4.23). Higher CO_2 splitting, in fact, is achieved by thermal processes like (4.23), even if the discharge will be not energy efficient

$$\mathbf{CO_2 + O \rightarrow CO + O_2} \tag{4.23}$$

4.2 Pulsed Calculations

In order to study the effect of pulsing on the CO_2 kinetic model, the following assumptions were made:

- A reduced kinetic model is considered where negative ions and excited states are neglected. However, their effect on the chemistry will be pointed out at the end of the Chapter.
- In the first simulations, time evolution of electron temperature is imposed externally as input, while in the others its value is calculated self-consistently from the energy balance equation by imposing a power density profile.
- Electron density is deduced from quasi-neutrality assumption.

Effect of electron temperature Aim of this part is to study the effect of a long pulse on a CO_2 discharge. This effect is obtained by fixing the electron temperature (i.e. at 2 eV, as shown in Fig.(4.7)) until equilibrium composition is reached. After that, T_e is dropped down to gas temperature (i.e. at 600 K) in tenths of microseconds in order to study post discharge conditions.

Initial pressure considered is again around atmospheric pressure (i.e. 1000 mbar in this case) that leads to an input CO_2 density of $1.21 \cdot 10^{25}$ m^{-3}, while the other densities are set to a value ten orders of magnitude lower. Initial electron density is set at $1.1 \cdot 10^{16}$ m^{-3} in order to fulfil the quasi-neutrality requirement.

The dynamics of CO_2 discharge can be divided in two parts: *discharge* and *post-discharge* (or afterglow) conditions that are defined by the electron temperature profile, as shown in Fig.(4.7).

1) Discharge Conditions: In this phase, electron temperature was fixed at 2 eV. The dynamics of neutral species is dominated by electron impact reactions, as already mentioned in Sec.(4.1) for steady-state calculation. In particular, electron impact dissociation of $\mathbf{CO_2}$ (i.e. (4.1)) plays the major role. This process lead to the formation of CO molecules, O and C atoms that increase with almost the same rate until about 10^{-5} s.

Time-evolution of ion densities is shown in Fig.(4.8). Since electron density is calculated from quasi-neutrality assumption, its value is around 10^{16} m^{-3} during discharge conditions.

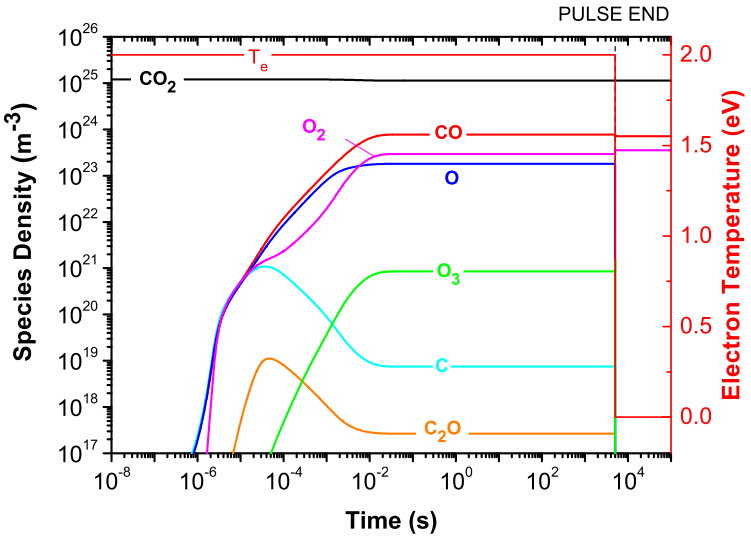

Figure 4.7: ***Time evolution of principal neutral species in CO_2 pulsed discharge with input electron temperature of 2 eV. Electron density is calculated from quasi-neutrality assumption.***

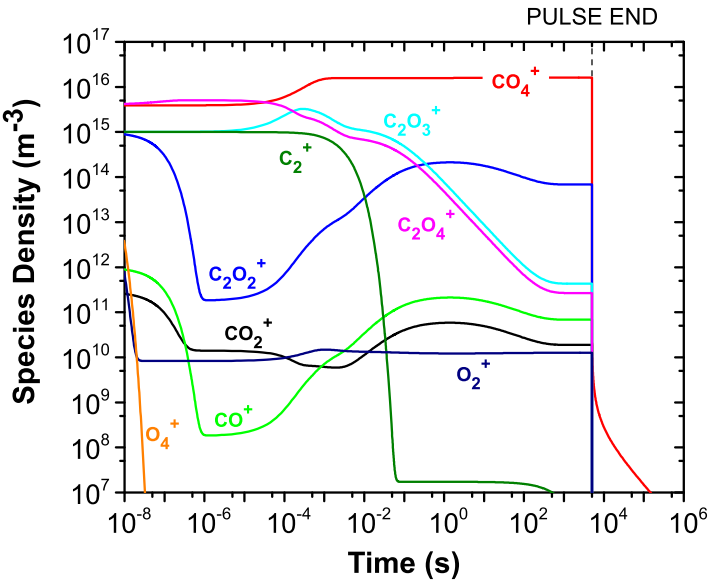

Figure 4.8: ***Evolution of ion densities for pulsed calculations at input electron temperature of 2 eV.***

For electron densities below 10^{20} at 2 eV, steady-state calculations already showed that $\mathbf{O_4^+}$, $\mathbf{C^+}$ and $\mathbf{O^+}$ species are negligible. From this model, it has been observed that O^+ and C^+ densities drop in 10^{-10} s, thus are not visible in Fig.(4.8). Principal causes of that are charge exchange reactions (4.24) and (4.25) with CO_2:

$$\mathbf{C^+ + CO_2 \rightarrow CO^+ + CO} \tag{4.24}$$

$$\mathbf{O^+ + CO_2 \rightarrow CO_2^+ + O} \tag{4.25}$$

In addition, a similar trend can be seen between clusters of ions like $\mathbf{C_2O_3^+}$ and $\mathbf{C_2O_4^+}$. As pointed out in steady-state calculations, this is mainly due to the reaction chain including (4.16) and (4.17). The net result of those reactions is the production of $\mathbf{C_2O_2^+}$, whose increase in time can be seen after 10^{-4} s. Furthermore, $\mathbf{C_2O_2^+}$ and $\mathbf{CO^+}$ ions show similar evolution trends. This behaviour is mostly due to the fact that $\mathbf{C_2O_2^+}$ is source for $\mathbf{CO^+}$ due to reaction (4.26):

$$\mathbf{C_2O_2^+ + M \rightarrow CO^+ + CO + M} \tag{4.26}$$

However, the rate of this reaction is lower than the rate of $C_2O_2^+$ formation(4.17). Furthermore, $\mathbf{CO_4^+}$ is shown to be the dominant ion of the discharge. Production of this ion is mostly due to (4.27):

$$\mathbf{O_2^+ + CO_2 + M \rightarrow CO_4^+ + M} \tag{4.27}$$

2) Post-Discharge Conditions: This part describes the afterglow phase of the pulsed simulation aforementioned (i.e. where input T_e was fixed at 2 eV). The sudden drop of electron temperature to gas temperature causes electron impact reactions to become negligible compared to heavy particle collisions. Thus densities of some neutral atoms (like **O** and **C**) and ions drop immediately after the pulse since their main source is due to electron impact dissociation and ionization processes respectively. Some small effect can be noticed from Fig.(4.7). In particular, CO_2 density increases slightly during afterglow mostly due to three-body recombination between **CO** and **O** (i.e. reaction (4.9)). This reaction is even responsible for the consequent small drop in CO density after the pulse. Furthermore, recombination of O-atoms via (4.8) is the dominant loss channel and causes a small increase in $\mathbf{O_2}$ density that stays constant during afterglow. Moreover, since $\mathbf{O_3}$ is mainly produced by (4.28), a sudden drop to 10^{11} m^{-3} is observed in the afterglow. This is mostly due to a decrease of O-atom reservoirs.

$$\mathbf{O + O_2 + M \rightarrow O_3 + M} \tag{4.28}$$

Moreover, while all ion densities drops in tenths of microseconds due to the fast drop of electron temperature, $\mathbf{CO_4^+}$ ion appears to be more stable in the afterglow. This effect suggests that *charge exchange* processes and higher *dissociative recombination* rates for this ion have to be implemented.

4.2.1 High power density

As only difference with respect the pulsed simulations above, here the electron temperature is calculated self-consistently within the model. In order to do that, a square power pulse in time of 50 μs is defined, with a maximum input power density of $2{\cdot}10^{11}$ W/m^3 during pulse phase. These conditions are more similar to a DBD case in which high reduced electric field (more than 200 Td) is applied. Initial pressure of 1000 mbar is assumed, together with a fixed gas temperature of 600 K. Electron density is still calculated from quasi-neutrality assumption, while negative ions and excited states are removed.

Neutral species Time evolution of neutral species density is shown in Fig.(4.9a) during pulsed and afterglow conditions. Since oxygen species can drive dissociation processes in CO_2 plasmas, most of results of this section are related on **oxygen dynamics** and how this is correlated with the evolution of other species.

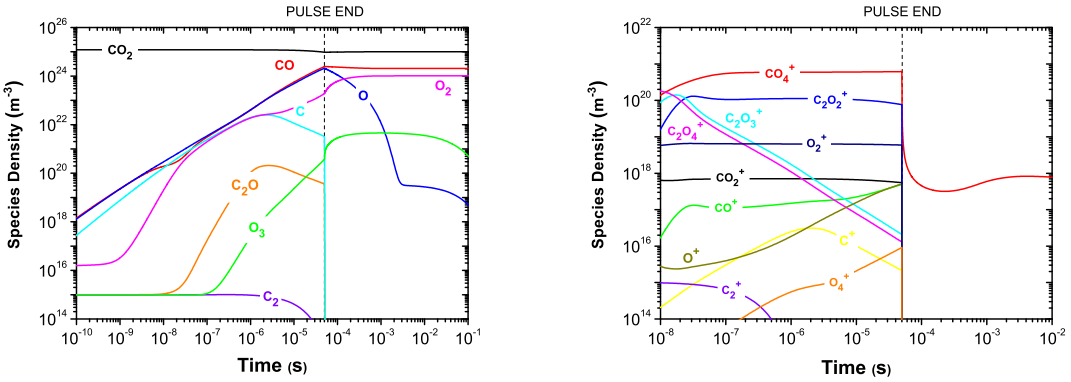

(a) Neutral species. **(b)** Ions.

Figure 4.9: ***Time evolution of neutral species (left) and positive charged ions (right) under a power pulse in time of 2·10^{11} W/m^3 (DBD conditions) for a 1000 mbar gas pressure and 600 K of gas temperature.***

During discharge conditions, the high power density applied influences the evolution of electron temperature. In particular, a steep increase of electron temperature above 7 eV is observed in the first nanoseconds during the pulse due to low electron density, then quickly settles to a constant value around 3.15 eV. For this reason, electron-impact reactions with ground state molecules dominate the chemistry during pulse-phase. Created **CO** and **O** species follow the same trend and are mainly produced by electron impact dissociation of CO_2 via reaction (4.1).

At high electron temperatures, production of **C** atoms is mostly determined by electron impact dissociation of CO that leads to the production of C and O atoms. However, the rate of this reaction is lower than the one of (4.1). The result is a net production of CO, O and C that increase with similar trends during discharge phase.
Electron temperature sharply decreases when the power is turned off and it drops to gas temperature in tenths of μs. This drop causes the competition of several processes involving oxygen that happens in different timescales. Those effects are summarized in the following:

1. **from 50 μs to 50 ms:** O-atoms recombine quickly into O_2 and O_3 due to the following reactions (4.29), (4.30) and (4.31) that happen almost with the same rate and lead to the formation of CO_2:

$$\mathbf{O + O + M \rightarrow O_2 + M} \tag{4.29}$$

$$\mathbf{O + CO + M \rightarrow CO_2 + M} \tag{4.30}$$

$$\mathbf{O + O_2 + M \rightarrow O_3 + M} \tag{4.31}$$

2. **from 50 ms to 200 ms:** ozone produced from reaction (4.31) is relatively stable, but at long enough time it dissociates via reaction (4.32):

$$\mathbf{O_3 + M \rightarrow O_2 + O + M} \tag{4.32}$$

Charged species Fig.(4.9b) shows the time evolution of the positively charged ions included in the model. From this plot, the following observations can be done:

- $\mathbf{CO_4^+}$ is the **dominant ion** during *discharge* at atmospheric pressure and $T_e > 2$ eV due to three-body reactions with O_2^+ and CO_2 (i.e. (4.18). This ion appears to be stable

in *afterglow* due to lack of charge exchange processes and its lower recombination rate implemented in the model

- Production of $\mathbf{C_2O_2^+}$ is mostly due to quenching of $\mathbf{C_2O_3^+}$ and $\mathbf{C_2O_4^+}$ with **CO**. Moreover, evolution of $\mathbf{C_2O_2^+}$ follows the same trend of $\mathbf{CO^+}$ due to reaction (4.26)
- Production of $\mathbf{O_2^+}$ and $\mathbf{CO_2^+}$ are mostly due to ionization of O_2 and CO_2 respectively. Furthermore, CO_2^+ is source of O_2^+ due to the following reaction (4.33):

$$\mathbf{CO_2^+ + O \rightarrow O_2^+ + CO} \tag{4.33}$$

Effect of negative ions In this part the effect of adding negative ions in the discharge is studied. In order to do that, different simulations were performed in the same conditions as before just adding processes that involves the presence of negative ions. The time evolution of negative charged species is shown in Fig.(4.10).

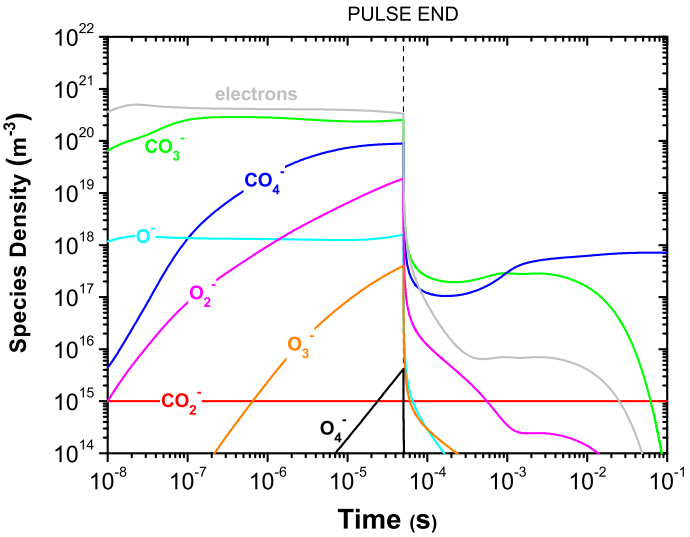

Figure 4.10: ***Evolution of electron density and negative ion densities for a 50 μs power pulse of $2{\cdot}10^{11}$ W/m^3 at 1000 mbar and 600 K of fixed gas temperature.***

The following observations can be deduced from the analysis of dominant negative ion pathways:

- $\mathbf{O^-}$ is mostly produced by *dissociative attachment* processes, like (4.34):

$$\mathbf{e^- + CO \rightarrow O^- + C} \tag{4.34}$$

- $\mathbf{CO_3^-}$ is produced mainly by *three-body association* (4.35):

$$\mathbf{O^- + CO_2 + M \rightarrow CO_3^- + M} \tag{4.35}$$

- $\mathbf{CO_4^-}$ is mainly produced by three-body collisions (4.36):

$$\mathbf{O_2^- + CO_2 + M \rightarrow CO_4^- + M} \tag{4.36}$$

According to Beuthe [49], theoretical studies on thermal plasmas show significant concentration of $\mathbf{CO_3^-}$, $\mathbf{O_2^-}$ and $\mathbf{CO_4^-}$ at T_e between 6000 K and 18000 K. Moreover, at $T_e > 12000$ K

also $\mathbf{O_3^-}$ become greater. Even if the presence of negative ions is seen to not have large effect on evolution of the other species (except to the minor ion O_4^+), it is worth mentioning here that their presence can lead to release of kinetic energy by *electron detachment* processes. In particular, if negative ions are included in the model, the electron temperature is seen to stay constant around 0.5 eV, while not relaxing to gas temperature during afterglow phase. This unphysical effect influences even the evolution of ions in the afterglow that appears still to be produced from ionization processes. More studies are needed to understand how balancing of reactions rates while including negative ions influence the evolution of electron temperature through the electron energy balance equation. In particular, one reactions should be mentioned. This is the *electron impact attachment* of O_2 (4.37), whose rate coefficient is deduced from studies of thermal electron attachment to O_2 [56] for M = O_2:

$$\mathbf{e^- + O_2 + M \rightarrow O_2^- + M} \tag{4.37}$$

Electron impact attachment reaction (4.37) is essential as it will induce a decrease in CO_2 conversion since less electrons will be available for electron impact splitting of CO_2. In conclusion, even if evolution of negative ions barely influence CO_2 conversion, more studies are needed to understand balancing processes happening in the afterglow. This understanding appears to be fundamental for a correct implementation of a self-consistent model where the electron temperature is deduced from the electron-energy balance equation.

4.2.2 Low power density

In this Section, another simulation is performed with the same input parameters as before, while reducing the input power density from $2{\cdot}10^{11}$ W/m^3 (DBD case) to 10^7 W/m^3. This latter case is more similar to the MW range of operations. A reduced CO_2 model is still applied, where excited states are not included.

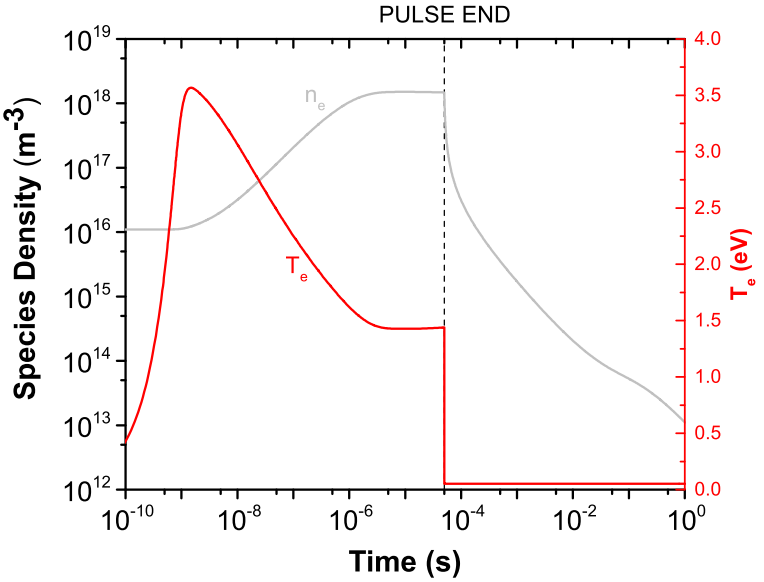

Figure 4.11: ***Evolution of electron density and temperature for a 50 μs power pulse of 10^7 W/m^3 at 1000 mbar and 600 K of fixed gas temperature.***

Electron kinetics Fig.(4.11) shows the time evolution of electron temperature and density. Electron temperature increases steeply up to 3.5 eV in the first nanoseconds, then it stabilise at a value around 1.5 eV during the pulse-phase. The steep increase is due to the electron energy balance equation that does neither take into account the presence of negative ions nor excited states. Inclusion of those species contributes to the balance of reaction rates of inelastic processes, thus lowering the value of T_e. As expected, lower value of power density with respect the DBD case leads to lower value of electron temperature. This fact influence the importance of electron-impact collisions and enhance the role of oxygen dynamics as a key driving process leading to dissociation, as shown in the next paragraph. Furthermore, electron density is calculated via quasi-neutrality assumption and it appears to increase during pulse-phase due to ionization processes. However, electron density values in the afterglow appear to be overestimated for long timescales (i.e. around some ms and later). This process is not realistic since ambipolar diffusion will take over ultimately.

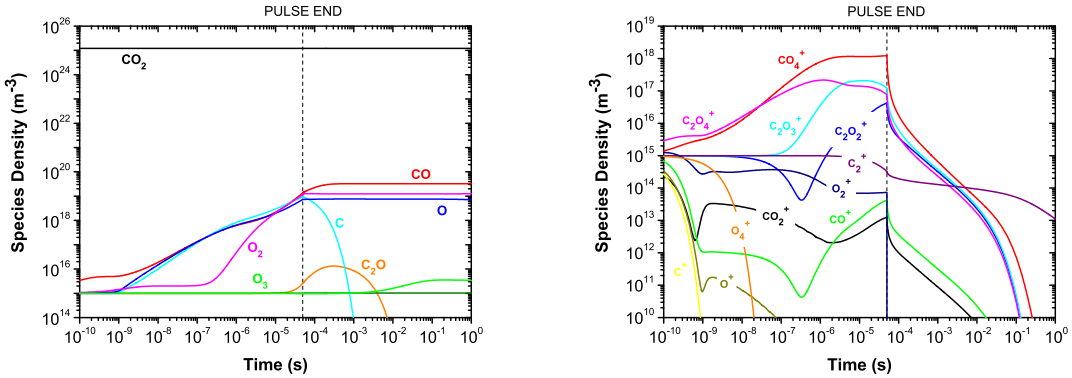

(a) Neutral species. **(b)** Ions.

Figure 4.12: ***Time evolution of neutral species (left) and positive charged ions (right) under a power pulse in time of 10^7 W/m^3 (MW conditions) for a 1000 mbar gas pressure and 600 K of gas temperature.***

Neutral dynamics *During pulse-phase*, electron impact process (4.38) is the dominant dissociative channel of CO_2:

$$\mathbf{e^- + CO_2 \rightarrow e^- + CO + O} \tag{4.38}$$

At $\mathbf{T_g = 600\ K}$, production of CO is enhanced by neutral reactions (4.39) and (4.40) involving carbon atoms:

$$\mathbf{CO_2 + C \rightarrow CO + CO} \tag{4.39}$$

$$\mathbf{O_2 + C \rightarrow CO + O} \tag{4.40}$$

Interestingly, if gas temperature is enhanced up to **2500 K** during the pulse, enhancement of reaction rate (4.41) during pulse-phase is observed with respect to the case at 600 K. Moreover, higher gas temperature during discharge leads to enhancement of production of O-atoms that improve the CO_2 conversion.

$$\mathbf{CO_2 + O \rightarrow CO + O_2} \tag{4.41}$$

In conclusion, if vibrational excitation is not relevant, higher gas temperature during the discharge lead to higher CO_2 dissociation due to increase of oxygen collisions. Moreover,

reduction of gas temperature in the afterglow with fast cooling rates, can help to reduce three-body collisions between CO and O leading to re-formation of CO_2 again.

After the pulse, balancing of interactions between CO_2 and CO still increase the production of O_2 and O. The result is that three-body recombination reactions (4.20) and (4.21) happen later than 0.1 s.

Ion dynamics Time evolution of positively charged ions are shown in Fig.(4.12b). Since the electron temperature is lower than the DBD case, presence of $C_2O_4^+$ ion is enhanced *during the pulse*, as predicted in Sec.(4.2). Production of $\mathbf{CO_4^+}$ and $\mathbf{C_2O_4^+}$ ions are mainly due to reactions (4.42) and (4.43):

$$\mathbf{O_2^+ + CO_2 + M \rightarrow CO_4^+ + M} \tag{4.42}$$

$$\mathbf{CO_2^+ + CO_2 + M \rightarrow C_2O_4^+ + M} \tag{4.43}$$

Moreover, with power density of 10^7 W/m^3 the C_2^+ density appears to stay constant during pulse and afterglow phase, as a difference with respect the DBD case before, where an higher power density of $2{\cdot}10^11$ W/m^3 was applied. This suggest the fact that in pulsed calculations, with low electron density, molecular carbon production is enhanced due to a lower reaction rates of slitting processes.

4.3 Influence of vibrational kinetics

The aim of this Section is to investigate the role of pulsing in the full kinetic CO_2 model. For doing that, two different types of discharge are considered that differ between each other for initial gas pressure and specific energy input (SEI):

- *DBD discharge:* High pressure of 1000 Torr is assumed together with high SEI up to 14 eV/molec. These assumptions are justified by the fact that DBD can easily operate at atmospheric conditions while an high reduced electric field is applied.
- *MW discharge:* Lower pressure of 20 Torr is assumed and lower values of SEI (i.e. up to 8 eV/molec) are typical with respect the DBD case.

For the following simulations, a cylindrical discharge volume is considered with radius of 1 cm and discharge length of 10 cm. Moreover, a constant fixed gas temperature is set at 400 K. If a particle flow rate of 5 slm is assumed, a residence time $t_r = 6.8$ ms and a gas density flow rate $Q_n = 7.1{\cdot}10^{25}$ m^{-3}s^{-1} are obtained from (1.4) and (1.5). In this model, even vibrational excitation is included where the corresponding de-excitation processes are defined explicitly as new reactions (so detailed balancing is not applied).

Role of pulsing Four different simulations were performed both for DBD and MW case. In both cases, a long pulse power pulse in time of 40 μs is applied, while electron temperature and density are calculated from the energy balance equation and quasi-neutrality assumption respectively. Knowing the SEI and gas density flow rate, the correspondent input power density ρ is calculated for DBD and MW cases, from (1.6). Results of these calculations are reported in Tab.(4.1).

Table 4.1: ***SEI assumed for DBD and MW case and corresponding calculated power density.***

Table 4.2: ***MW case.***

SEI (eV/molec)	ρ (W/m^3)
0.9	$1.0{\cdot}10^7$
1.75	$2.0{\cdot}10^7$
3	$3.4{\cdot}10^7$
8	$9.1{\cdot}10^7$

Table 4.3: ***DBD case.***

SEI (eV/molec)	ρ (W/m^3)
1.5	$1.7{\cdot}10^7$
3	$3.4{\cdot}10^7$
7	$8.0{\cdot}10^7$
14	$1.6{\cdot}10^8$

Fig.(4.14) shows the CO_2 conversion (i.e. calculated according to (1.7)) and its energy efficiency (i.e. calculated with (1.8)) as a function of the SEI for both the simulated discharges. CO_2 conversion around 10 % is obtained in the case of DBD, while it increases from 4 to 18

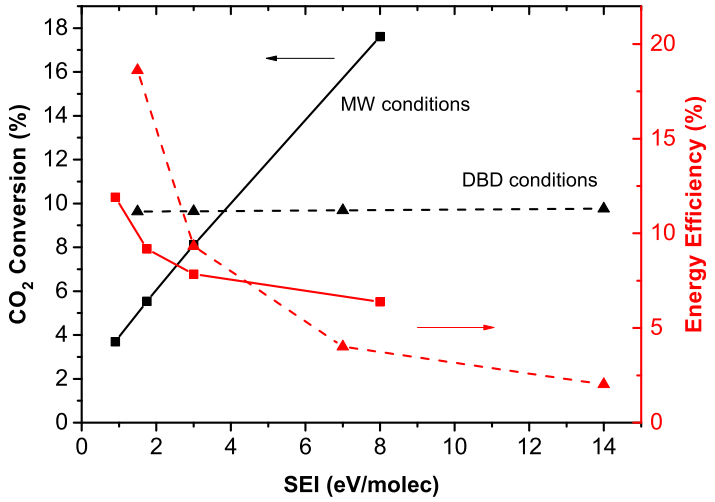

Figure 4.13: ***Total CO_2 conversion (in black) and corresponding energy efficiency (in red) as a function of the SEI for the simulated DBD and MW discharges.***

% in MW conditions even if lower SEI are assumed. This fact is mainly due to difference in pressure. In fact, at lower pressure, VT relaxation processes are less effective and VV up-pumping to higher vibrational levels can help to increase the overall conversion efficiency. In both cases, however, a CO_2 conversion below 20% is obtained. In fact, it is possible that the vibrationally excited states return to the ground state by relaxation, without resulting in CO_2 splitting. Opposite trend is observed for the energy efficiency that is always below 18% and decreases with SEI. Slightly higher values for the energy efficiency are obtained for the MW conditions fro SEI>4 eV/molec, due to the correspondent higher increase of CO_2 conversion.

Effect of excited states In order to study quantitatively how vibrational and electronic excited states influence CO_2 conversion and energy efficiency, different simulations were performed. In those simulations a pressure of 20 Torr and gas temperature of 300 K is assumed. If a flow rate of 15 slm is present in a cylindrical volume of radius 0.01 m and length 0.1 m, a residence time of 3 ms is obtained. As done in the paragraph before, assuming three

different input values of SEI, then the correspondent power density is calculated and reported in Tab.(4.4):

Table 4.4: ***Input SEI assumed and correspondent power density calculated for a 15 slm, 20 Torr, T_g=300 K and a cylindrical volume of radius 0.01 m and 0.1 length.***

SEI (eV/molec)	ρ (W/m^3)
0.1	$3.4{\cdot}10^6$
1	$3.4{\cdot}10^7$
10	$3.4{\cdot}10^8$

In these simulations, a square pulse in time of 40 μs was simulated with an initial constant power density taken from Tab.(4.4). Results are shown in Fig.(4.14) where the CO_2 conversion and energy efficiency are plotted as a function of the three different values of SEI assumed. Results obtained from the complete CO_2 model are compared with the ones ob-

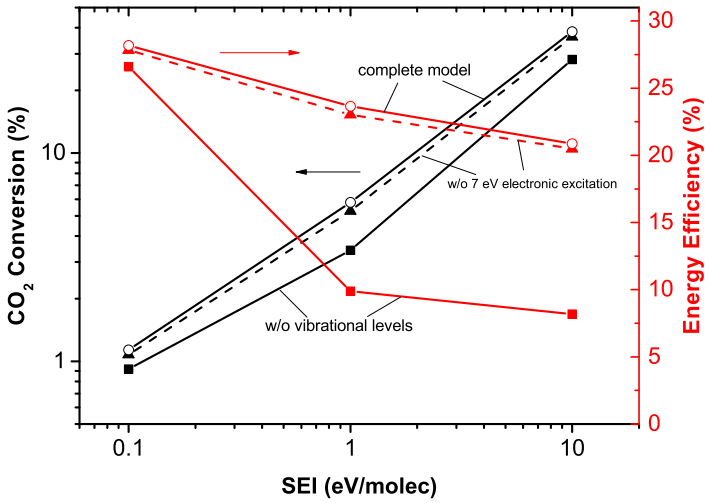

Figure 4.14: ***Total CO_2 conversion (in black) and corresponding energy efficiency (in red) as a function of the SEI for the simulated discharge. Results with the complete CO_2 model are compared with the ones obtained by removing the vibrational excited states and the 7 eV electronic excitation process. An initial pressure of 20 Torr and gas temperature of 300 K.***

tained removing the vibrational states and the ones obtained by removing only the electronic excitation channel to the 7 eV states (i.e. Phelps database [24]). All the results show an increase of the CO_2 conversion from around 1% at 0.1 eV/molec to a value around 30% at 10 eV/molec. Moreover, if vibrational levels are neglected lower CO_2 conversion and energy efficiency are obtained. This results shows that vibrational excitation processes cannot be neglected if a MW discharge is taken into account. However, still limited CO_2 conversion and energy efficiencies are obtained and far from the results in literature [9], suggesting that in this model the vibrational excitation mechanism to higher levels is limited by VV' and VT relaxation processes.

Concerning the electron impact cross section, in the current model two main processes that lead electronic excitation are considered: the first one corresponds to the excitation of an electron state with a threshold energy of 7 eV, while the second corresponds to higher excitation to 10.5 eV states (i.e. see Tab.(2.2)). The cross section of the first process are not

considered in the Itikawa database [46], which considers only a dissociation channel with a threshold energy of 12 eV. Moreover, the experimental dissociation cross section by Cosby et Helm [57] partially confirms the Itikawa cross section being, however, up to a factor 5 larger [58]. For this reason, the effect of removing the 7 eV excitation channel on the CO_2 conversion is investigated in this model. Results in Fig.(4.14) show that removing the 7 eV excitation channel, however, leads to negligible effect in the overall CO_2 conversion and energy efficiency. This means that vibrational excitation processes are dominant mechanisms in these conditions with respect electronic excitation.

Vibrational Distribution Function One of the aim of vibrational kinetics is to study the possibility of achieving vibrational distribution far from the Boltzmann one [59]. In order to study this effect, a discharge of 40 μs pulse period is applied to a MW-case (i.e. where the pressure is set at 20 Torr, $T_g = 400$ K). Results of these calculations are compared with the ones obtained by Capitelli [55] where an input reduced electric field of 50 Td is assumed. In the calculations reported here, however, a power density of $1{\cdot}10^7$ W/m^3 is used as input that is deduced from considerations above and leads to a comparable value of electron temperature and density with respect the calculations of Capitelli.

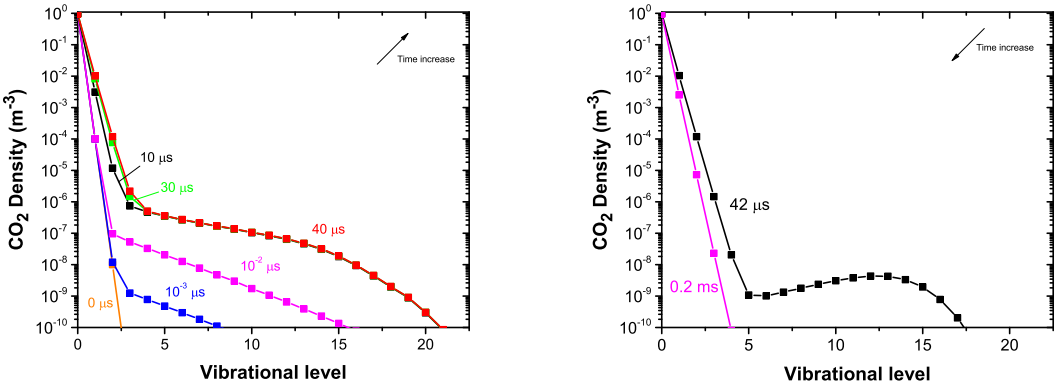

(a) Under discharge conditions.

(b) Post discharge conditions.

Figure 4.15: ***Vibrational distribution functions of the asymmetric mode vibrational levels of CO_2 in the MW case for 40 μs discharge at different times during discharge and post-discharge conditions.***

Results plotting the vibrational distribution function (i.e. vdf) of the CO_2 asymmetric mode levels are shown in Fig.(4.15) in both discharge and post-discharge conditions. During the discharge, the vdf is governed by vibrational excitation due to electron impact processes up to 10^{-2} μs, while for higher times a plateaux is formed due to VV processes that populate higher vibrational levels. As reported in [55], from 10 μs to 40 μs the long plateaux in the vdf is formed by the predominant VV rates against the VT ones. The higher energy part of the distribution ($\nu > 18$) is controlled by VT rates, which push the vdf tail to a Boltzmann one at T_{gas}. In post-discharge conditions, the VT relaxation rates increase, thus higher vibrational levels are underpopulated until Boltzmann distribution is recovered after few tenths of ms. In this case, the vdf decreases since eV processes reduce their importance as compared to VT ones because of the strong decrease of the electron density. Results of these calculations, however, show that vibrational excited levels are less efficiently populated with respect to the case of Capitelli [55]. In particular, mayor differences with respect Capitelli calculations can be seen during discharges where the vdf in Fig.(4.15a) appears to not change from 10

to 40 μs. Moreover, fast relaxation to the Boltzmann distribution in 0.2 ms is observed in Fig.(4.15b), while in Capitelli it relaxes after 1 ms. The main differences between these results are mainly due to the electon energy distribution function (EEDF) that is assumed Maxwellian in the current state model, while it is calculated self-consistently in the model of Capitelli. Different EEDF leads to a computation of different rate coefficients that influence the relative importance of VV and VT processes. Besides the method for determining rate coefficients for electron impact reactions, in PLASIMO the power density is assumed as input, while in Capitelli the reduced field is used. For this reason, a one-to-one comparison between the two models is not appropriate and only major differences are considered here. The last minor effect that can contribute to differences is the numerical precision that is assumed for the constants used in the model.

Part II

Numerical Reduction Techniques

CHAPTER 5

Linear Principal Component Analysis

In *Part I* of this thesis a description and systematic analysis of a CO_2 kinetic model is presented. This approach is based on a State-To-State description (STS) where all the different excited levels (i.e. electronic and vibrational) are treated independently as different species. Time evolution of those species is calculated via a set of partial differential equations that involve particle and energy balance conservations. However, the prodigious number of reactions and species implemented leads to high computational loads and difficulties for the data analysis and output interpretation. In order to overcome those problems, two methods have been developed to reduce the number of species equations:

1. **Reduction techniques:** it is accomplished by determining the minimum set of relevant species and dominant reaction rates in the original kinetic mechanism. An example of this category is the work presented by de La Fuente et al. [60] who proposed a methodology for the reduction of vibrational kinetics by lumping of excited levels. Moreover, a different chemical reduction technique called Intrinsic Lower Dimensional Manifolds (ILDM) was developed by Maas and Pope [61]. This technique is based on the fact that a reaction system usually includes different timescales. Since fast timescales are assumed in quasi-steady state (i.e. they are so fast that any changes in the systems occur quickly), the system can be described only by slow timescales without any significant loss of information

2. **State space parametrization:** This approach is based on the assumption that the thermodynamic state of a reacting system relaxes onto a low-dimensional manifold in chemical state space. Thus, if a set of optimal variables is identified, the whole thermochemical state can be reparametrized with a lower number of variables, which nevertheless must provide a satisfactory approximation of the system in a lower dimensional space. An example of this technique is Principal Component Analysis (PCA)[1] [62]

Both those methods have been widely applied in combustion community (e.g. by A. Parente

[1] **Note:** In this Chapter PCA will always refers to the *linear* version in which linearity is assumed between original variables and the new ones, according to *Assumption I* of Sec.(5.1). Different nonlinear techniques will be exploited in the next Chapter.

[63]) and only recent studies at Eindhoven University of Technology by Rehman et al. [64] and Peerenboom et al. [65] shine light about the possibility of applying ILDM and PCA respectively in plasma chemistry datasets. The present work focuses on the second approach. In this Chapter, according to the work of Peerenboom et al. [65], a mathematical derivation of PCA is presented followed by an application on a CO_2 kinetic model describing a plasma discharge. The aim is to develop a fundamental understanding on this numerical technique and its applicability on plasma chemistry datasets. Advantages and limitations of this method will be explained at the end of this Chapter.

In order to dispel the magic under the black-box of PCA, all the results of the analysis written here have been performed with codes written in MATLAB® and exchange of ideas and opinions with Peter Koelman and Stef Bardoel was of fundamental importance and useful for code-to-code benchmarking, thus they are here gratefully acknowledged.

5.1 Aim and assumptions

One of the primary goals dealing with multivariate data is to reduce the dimensionality of the datasets for data explorations and further processing. PCA can be successfully used for this purpose. The main aim of PCA is to map the data into a space of lower dimensionality while preserving as much of the information as possible for describing the overall dynamics of the system. In this Section, the mathematical derivation and nomenclature used in PCA are introduced. Even if a more rigorous mathematical derivation can be found in [66] and some tutorials are also available in [67], here a *step-by-step* approach is explained in order to highlight advantages/disadvantages and assumptions of the method for a correct numerical implementation.

Mathematical background PCA is a mathematical tool first introduced by Pearson [68] and used to reduce the dimensionality. Even if the link between the physical intuition and mathematics may sometimes be hard to catch, every PCA starts from a training set as **input**. In practise, a training set is composed of a sample of n *observations* of p *variables*, where p is the number of variables before reduction[2]:

$$\mathbf{X_i} = (x_{i1}, \ldots, x_{ip}) \qquad i = 1, \ldots, n \tag{5.1}$$

where $\mathbf{X_i}$ in (5.1) is a vector storing the values of the p variables for the ith observation. If you are performing an experiment or a simulation, each of the p-variables of $\mathbf{X}$ can be seen as measurements of multiple quantities (i.e. density, temperature, voltage, etc.) recorded for n different times. Generally speaking, $\mathbf{X}$ is a $n \times p$ matrix that contains all the training data that comes from experiments or simulations. Starting from this point, the aim of PCA is the following:

Aim
PCA is concerned with finding a few ($\ll p$) derived variables, called Principal Components (PCs), which nevertheless preserve most of the information present in the original data

[2]This is an approximation for a finite population even if this theory can be extended for infinite population of measures

In order to do that, PCA detects relationships among a set of *correlated* variables. If the original variables are highly correlated, it means that they are 'saying the same thing', thus some redundancy is present in the system. This redundancy may be eliminated by an appropriate *change of basis* in order to transform the original variables in a new set of uncorrelated variables called *principal components*. In its linear version, PCA makes an important assumption for finding this new set of variables:

Assumption
The new variables are *linear* combinations of the original variables. Moreover, they are *uncorrelated* (i.e. orthogonal) and derived so that the variance of one component is maximum.

This assumption vastly simplifies the problems by restricting the possible number of basis only to linear combinations of them. In practise, for a single observation of $\mathbf{X}$, $\mathbf{X_i}$, the first new variable z_{i1} is given by the linear relation (5.2):

$$z_{i1} = \mathbf{X_i a_1} \qquad i = 1, \ldots, n \tag{5.2}$$

where the vector of coefficients $\mathbf{a_1}$ is chosen to maximize the variance of z_{i1}. In addition, a normalization is superimposed such that $\mathbf{a_1^T a_1} = 1$. In the same way, a second variable z_{i2} is determined by choosing $\mathbf{a_2}$ in order to maximize the variance of z_{i2}, subject to the constraint $\mathbf{a_2^T a_2} = 1$. In addition to the normalization constraint, it is now imposed a second constraint that z_{i2} should be uncorrelated with z_{i1}, such that their covariance is zero:

$$cov(\mathbf{X a_1}, \mathbf{X a_2}) = 0 \tag{5.3}$$

Equation (5.3) is equivalent to the simpler constraint: $\mathbf{a_2^T a_1} = 0$, thus vectors $\mathbf{a_1}$ and $\mathbf{a_2}$ are taken as *orthogonal*. According to this method, the following property can be pointed out:

Property
Members of basis set are *orthogonal* and *normalized* such that linear combination of them can express any arbitrary object in the space of interest.

The procedure aforementioned can be summarized in the following points:

- PCA first select the direction along which the variance of $\mathbf{X}$ is maximized and it saves as $\mathbf{a_1}$.
- Second, it finds another direction along which the variance is maximized, however, according to the orthonormality condition, it restrict its search only to directions perpendicular to the previous one.

Numerical implementation This part focuses on the numerical aspect of PCA aiming to define a series of steps that can be followed for a correct code implementation.

1. **Construction of the training set:** The first input that has to be provided to PCA is the training set. As mentioned before, a training set is a matrix whose columns are associated with different variables (e.g. different species densities) and whose rows represent the observables (e.g. different temporal values of the same variable). All variables and observations are stored in a $n \times p$ matrix $\mathbf{X}$. Someone may argue that PCA has the drawback of depending on the availability of a data set for extracting

the PCs. However, it has been demonstrated [63] that this technique has the potential to extract the PCs from a target system and to apply them to a similar system. In this context, it is possible to say that PCA has a predictive power that is potentially attractive for plasma chemistry simulations.

2. **Data preprocessing:** Data manipulation is a determinant step of PCA since it may affect the final results, as it will be shown in Sec.(5.2). Usually, *centering* is applied by subtracting the mean of each variable calculated from all observables. The advantage of this procedure is that all the observables are converted to fluctuations, thus leaving only the relevant variations for the analysis. In addition, the centered matrix is *scaled* with an appropriate matrix of coefficients $\mathbf{D}$. The choice of this $\mathbf{D}$ matrix is essential when the elements of $\mathbf{X}$ have different units or when they span in a large range of validity (i.e. have large variance). This may be the case of temperatures that may range from room temperature to several electronvolts or densities that have a wide time evolution. After centering and scaling processes a new matrix $\widetilde{\mathbf{X}}$ is defined according to (5.4) that takes into account those manipulations of data:

$$\widetilde{\mathbf{X}} = (\mathbf{X} - \bar{\mathbf{X}})\mathbf{D}^{-1} \tag{5.4}$$

where $\mathbf{X}$ is the original matrix, $\bar{\mathbf{X}}$ contains the mean of each variable and $\mathbf{D}$ is a diagonal matrix containing the scaling coefficients for all the variables. It is worth noting that data preprocessing affects the final results of PCA such that the principal components are generally changed by scaling and they are not a unique characteristic of the system.

3. **Finding the PCs:** This step is part of the proper PCA algorithm. This algorithm proceeds first by calculating the covariance matrix $\mathbf{S}$ from (5.5), in order to measure the correlation among different variables:

$$\mathbf{S} = \frac{1}{n-1}\widetilde{\mathbf{X}}^{\mathbf{T}}\widetilde{\mathbf{X}} \tag{5.5}$$

where $\mathbf{S}$ is a square symmetric $p \times p$ matrix whose diagonal terms are the variance of a variable and the off-diagonal terms are the covariance between particular variables. Once the principal components are calculated, the off-diagonal terms should be zero such that each variable co-vary as little as possible with other variables. Therefore, removing redundancy is equivalent to *diagonalizing* $\mathbf{S}$. Recalling the eigenvector decomposition, $\mathbf{S}$ can be written as (5.6):

$$\mathbf{S} = \mathbf{A}\mathbf{L}\mathbf{A}^{\mathbf{T}} \tag{5.6}$$

where $\mathbf{A}$ is a $p \times p$ orthogonal matrix whose columns are the eigenvectors of $\mathbf{S}$ and $\mathbf{L}$ is a $p \times p$ diagonal matrix containing the eigenvalues of $\mathbf{S}$ in descending order, $l_1 > l_2 > \cdots > l_p$. In this framework, eigenvalues can be interpreted as the measures of variances of different components. According to this procedure, *principal components* (PCs) are defined as the ordered eigenvectors of $\mathbf{S}$, each of them associated with a particular eigenvalue. Once calculated the principal components, a new set of variables, $\mathbf{Z}$, can be defined in matrix form as (5.7):

$$\mathbf{Z} = \mathbf{X}\mathbf{A} \tag{5.7}$$

where $\mathbf{Z}$ is a $n \times p$ matrix of new variables usually called *PC scores*, that represent the projection of the processed data onto the PC basis.

4. **Backward transformation and reduction:** Since PCA assumes a linear transformation between variables, the original variables can be stated as a function of the PCs via the *backward transformation* (5.8):

$$\mathbf{X} = \mathbf{Z}\mathbf{A}^{-\mathbf{1}} \tag{5.8}$$

Considering only $q < p$ components, which account for the larger fraction of variance originally contained in the data, a new truncated dataset of PC scores can be defined by (5.9):

$$\mathbf{Z_q} = \mathbf{X}\mathbf{A_q} \tag{5.9}$$

Finally, original data can be expressed in a more compact form that takes into account components with larger variance by using the following *linear backward transformation* (5.10):

$$\mathbf{X_q} = \mathbf{Z_q}\mathbf{A_q^{-1}} \tag{5.10}$$

Since eigenvalues can be interpreted as variance measures, it is possible to define some criterion to determine how small q can be taken without serious information loss. One of these criteria is based on the definition of the *cumulative fraction* t_p of the total variance through (5.11):

$$t_p = \frac{\sum_{k=1}^{q} l_k}{\sum_{k=1}^{p} l_k} \tag{5.11}$$

since the eigenvalues l_k represent a measure of variance of the different components, the smallest number of q PCs is chosen in order to have a a percentage value of t_p that exceed a level of 80% or 90% with respect to the total value. Since principal components with larger variances are associated with interesting dynamics, while lower variances indicate PCs with lower auto-correlation, this approximate procedure ensures that with the reduced numbers of PCs it is still possible to describe the principal features of the system.

Fig.(5.1) represents a schematic illustration of PCA applied to data in two dimensions that presents a correlation along $Y = X$ line. As shown in those figures, the method starts from the training set illustrated in Fig.(5.1a) that is composed by a system of 250 random numbers with two variables correlated along one direction. Fig.(5.1b) shows that PCA finds the optimal change of basis in which variances of the components are maximized. Firstly, the main direction $\mathbf{a_1}$ which present most of the signal is found. Secondly, direction $\mathbf{a_2}$ is determined restricting the search only to the ones perpendicular to $\mathbf{a_1}$. Fig.(5.1c) represents the change of basis in which new data are expressed. In this case, the transformation is a simple rotation of coordinate system. Lastly, Fig.(5.1d) shows the results of the backward transformation and reduction described in Step 4. In this transformation, only one component is taken into account, thus even if some information are lost, the main dynamics of the system (i.e. along $X = Y$) is clearly identified.

5.2 PCA on plasma chemistry

This section describes the application of **PCA on global models**, following the work of Peerenboom et al. [65]. As described in the method above, PCA is a possible solution to reduce the dimensionality of a dataset by reparametrizing the chemical state space into a *lower dimensional manifold* containing the essential kinetics. The final goal of this method is to solve continuity equations only for a reduced number of PCs, thus leading to a reduction

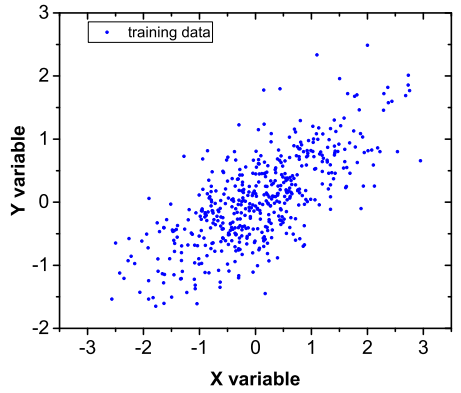

(a) Step 1: Training data.

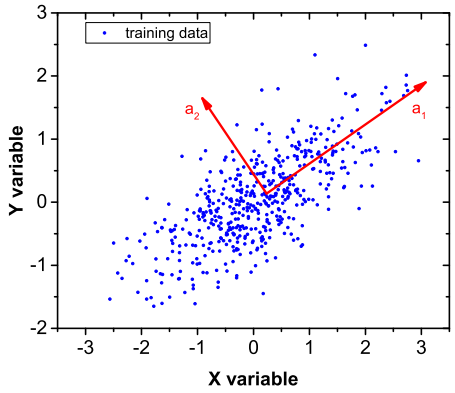

(b) Step 2: identification of the orthogonal PCs.

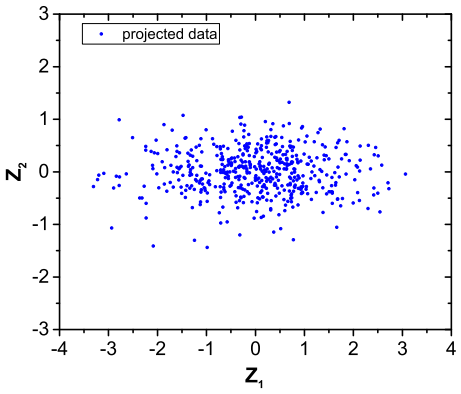

(c) Step 3: Change of basis.

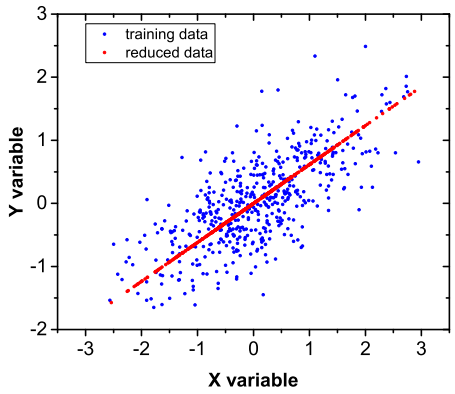

(d) Step 4: Reduced backward transformation.

Figure 5.1: ***Application of PCA method to random data correlated along one direction.***

of computational load for future applications in 2-D or 3-D models. However, in this Chapter the *input* training set is a 0-D kinetic model developed by Peerenboom et al. [65] that is particularly interesting for understanding basics assumptions and steps of the method which was implemented using MATLAB®.

Initial conditions In this case, the input training set of PCA is derived from a 0-D kinetic model that describes the time evolution of species densities in a CO_2 discharge. This model was developed in Eindhoven University of Technology to study the STS vibrational kinetics of CO_2 [65] and it was run on ZDPlaskin [69], a plasma kinetic solver that incorporates the BOLSIG+ solver for solving the electron Boltzmann equation for the calculations of rate coefficients. The species considered in the model are presented in Tab.(5.1):

In particular, only only two different charged species are considered (i.e. CO_2^+ and e^-). The electronically excited levels are denoted as $CO_2(e_i)$ with $i = 1, \ldots, n$ the progressive electronically excited state considered. Most of the focus is given on vibrational kinetics, where the first four symmetric mode levels of CO_2 are included together with the 21 asymmetric mode levels (i.e. $CO_2(\nu_a \ldots \nu_d)$ and $CO_2(\nu_1 \ldots \nu_{21})$ respectively). Moreover, the first 10 vibrational levels of CO and 4 vibrational levels of O_2 are considered in the kinetics. Input reactions

Table 5.1: ***Input species used for the kinetic CO_2 model in [65].***

Input Species
NEUTRALS
CO_2, CO, O_2, O_3
CHARGED SPECIES
CO_2^+, e^-
EXCITED SPECIES
$CO_2(e_1)$, $CO_2(e_2)$, $CO_2(\nu_a \dots \nu_d)$, $CO_2(\nu_1 \dots \nu_{21})$
$CO(e_1)$, $CO(e_2)$, $CO(e_3)$, $CO(e_4)$, $CO(\nu_1 \dots \nu_{10})$
$O_2(e_1)$, $O_2(e_2)$, $O_2(\nu_1 \dots \nu_4)$

implemented are of three types: electron-impact and heavy particle collisions involving vibrational energy exchange or formation of new neutral species. Electron impact cross sections are implemented and given as an input to the Boltzmann solver for the calculations of rate coefficients of electron impact reactions, while other reactions have an expression of rate coefficient in the typical Arrhenius form. It is worth noting here that ZDPlaskin, as a difference with the model implemented on PLASIMO does not solve the energy balance equation for electrons[3], but a routine is implemented that calculates the reduced electric field from the plasma parameters, as discussed in [21]. Fixed pressure (i.e. 100 Torr), gas temperature (i.e. 300 K), electron density and reduced electric field (i.e. 50 Td with a frequency of 2.45 GHz) were assumed for the simulations aforementioned. Seven different simulations were run with different ionization degree (i.e. different electron densities), those are: 10^{-7}, $2{\cdot}10^{-7}$, $5{\cdot}10^{-7}$, 10^{-6}, $2{\cdot}10^{-6}$, $5{\cdot}10^{-6}$ and 10^{-5}. This situation refers to an homogeneous plasma similar, in first approximation, to a microwave surfaguide discharge [70].

All the 7 different simulations aforementioned are included in the training set for the formation of the input matrix $\mathbf{X}$. This matrix is constructed such that each column is associated to the different species reported in Tab.(5.1) and each row represents different observations in time of the correspondent density. It is worth noting that in the following PCA calculations a proper time range was chosen in which the ionization degrees are constant for each simulations. Effect of steps in the ionization degree will be analyzed in Sec.(5.3).

Scaling Centering is always applied in conjunction with scaling. In this analysis five different scaling methods were used and are identifies by the following names, according to [71]:

- **Auto scaling:** it uses the standard deviation s_i such that all the elements of $\mathbf{X}$ have standard deviation equal to one. Diagonal elements D_{ii} of the scaling matrix are then defined as (5.12):

$$D_{ii} = s_i \tag{5.12}$$

- **PARETO scaling:** it scales the variables as the square root of the standard deviations, as shown in (5.13). In this case, the variables have a variance equal to the standard deviation.

$$D_{ii} = \sqrt{s_i} \tag{5.13}$$

[3]This means that electron temperature is not calculated from this model, thus is not included as a variable in the PCA procedure

- **VAST scaling:** it is an acronym of *variable stability scaling* and it is an extension of auto scaling. It is relevant for stable variables that does not show strong variations, thus have small relative standard deviation. The scaling factors are defined as (5.14):

$$D_{ii} = \frac{s_i^2}{\bar{X}_i} \tag{5.14}$$

  where $\bar{\mathbf{X}}$ contains the mean of each variables of the original input matrix (i.e. before scaling and centering).

- **Range scaling:** it uses the difference between the maximum and minimum value, as shown in (5.15). With this definition, range scaling is more sensitive to the presence of outliers since only two variables are used to estimate the scaling factors.

$$D_{ii} = max(X_i - \bar{X}_i) - min(X_i - \bar{X}_i) \tag{5.15}$$

- **Level scaling:** it uses the means of the original variables, as defined in (5.16). Like the previous scaling method, this one is also affected by the presence of outliers. Thus, compared to scaling methods based on standard deviations, it is more sensitive on species that appears with small concentrations in the datasets.

$$D_{ii} = \bar{X}_i \tag{5.16}$$

Manifold shape The task of PCA is to transform correlated species densities into uncorrelated variables called PC scores. These new variables parametrize a *low dimensional manifold* in the density-space that is governed by relaxation and fast processes, thus if a species interacts with these reactions it can be ignored in order to reduce the number of equations. It is generally possible to visually represent the manifold by plotting the scores of the first two components that are associated with larger variances. This technique can be also informative to determine the best scaling method to be applied and give information about the reconstruction error. In particular, *uniqueness* is necessary to assign a single value of species density for each couple of PCs. This means that, if the manifolds are overlapping each other, more PCs are needed to describe uniquely the density-space. In addition, *smoothness* is a key parameter to determine the best transformation that leads to a more accurate reconstruction. Manifolds for all the 7 different ionization degrees (i.e. from 10^{-7} to 10^{-5}) are plotted in Fig.(5.2) in the case of range scaling. According to the considerations above, this transformations cannot uniquely describe the system, even if the manifolds for each ionization degree can be visually separated, these are not smooth nor equally distributed. If this is the case it qualitatively means that more PCs are needed to accurately describe the chemical state space.

Reconstruction In this part, reconstruction from the PCs scores to the original densities is performed using the backward transformation (5.10). Fig.(5.3) shows a comparison between original densities (i.e. from the kinetic model) and reconstructed ones for the asymmetric stretch mode of CO_2 and a constant ionization degree of 10^{-6}, range scaling was used for both plots. Solid red lines represents original densities, while the black dots are the reconstructed ones using 5 and 10 PCs. As expected from the considerations above, increasing the number of PCs leads to better reconstruction, even if Fig.(5.3b) shows that more than 10 PCs are needed for an accurate reconstruction of densities for times below 10^{-5} s.

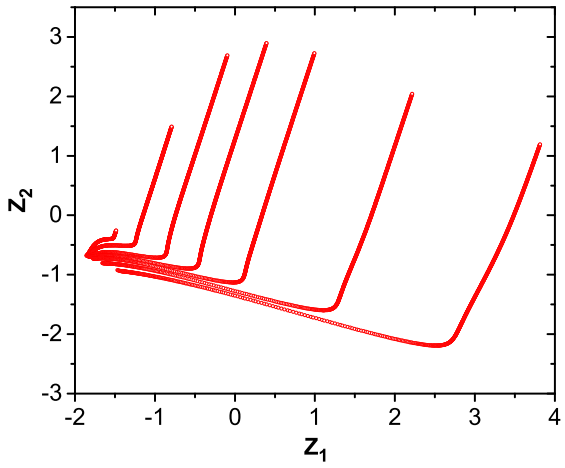

Figure 5.2: ***Manifold shape using range scaling. Different manifold are associated to different simulations in which the ionization degree was fixed.***

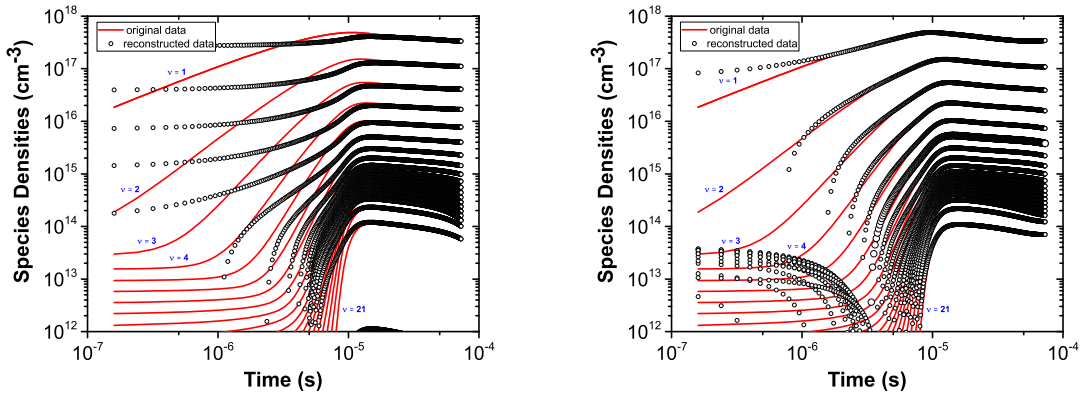

(a) 5 PCs. **(b)** 10 PCs.

Figure 5.3: ***Reconstruction of densities of asymmetric mode levels of CO_2 with 5 and 10 PCs. Range scaling was applied.***

Log-Transformation From considerations above, it is evident that a new method has to be found to improve the reconstruction using a lower number of PCs. In this paragraph a possible solution is presented in the form of log-transformation. This is an *a-priori* transformation applied by taking the logarithm of all species densities in the original matrix, before scaling and centering is applied. The numerical advantage of this method is the decrease of the dynamic range of the datasets, thus a reduction of gradients in species densities. The results of applying this log-transformation are evident looking at the manifold shapes. A comparison between the manifold shapes deduced with different scaling methods (and log-transformation) are shown in Fig.(5.4).

Moreover, results of density reconstruction using 5 and 10 PCs, *range* scaling and a *log-transformation* are shown in Fig.(5.5). From those figures, some considerations can be deduced:

- *Range* scaling gives better results by uniquely determining manifold shapes with less

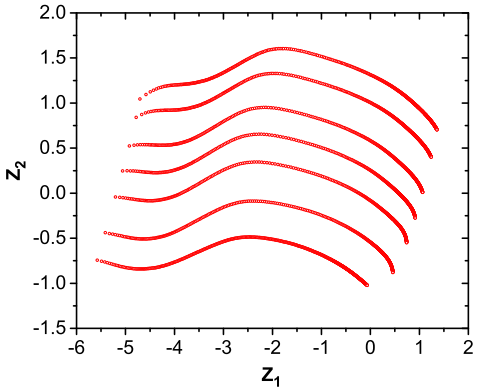

(a) Range scaling.

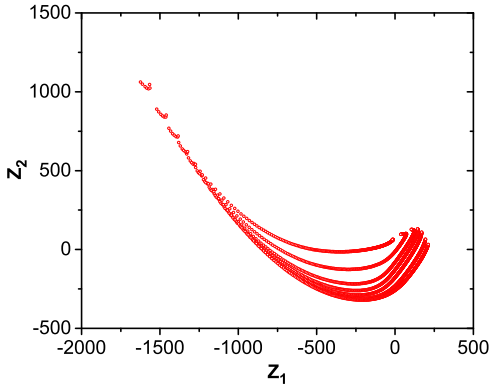

(b) VAST scaling.

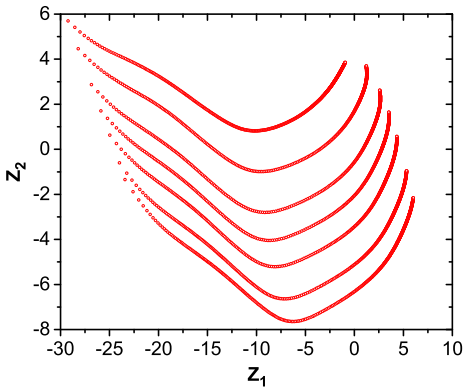

(c) Auto scaling.

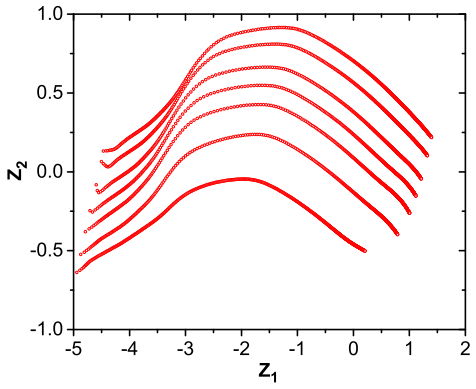

(d) Level scaling.

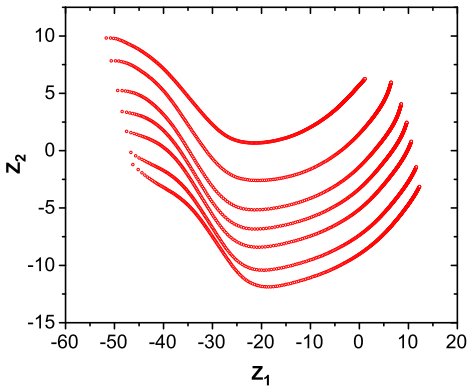

(e) PARETO scaling.

Figure 5.4: ***Manifold shapes for different scaling methods, using log-transformation.***

gradients.

- Comparing results from Fig.(5.3) and Fig.(5.5) and the correspondent manifold shapes (i.e. Fig.(5.2) and Fig.(5.4a)) it is evident that log-transformation greatly improves reconstruction results by decreasing the dynamic range of the variables.

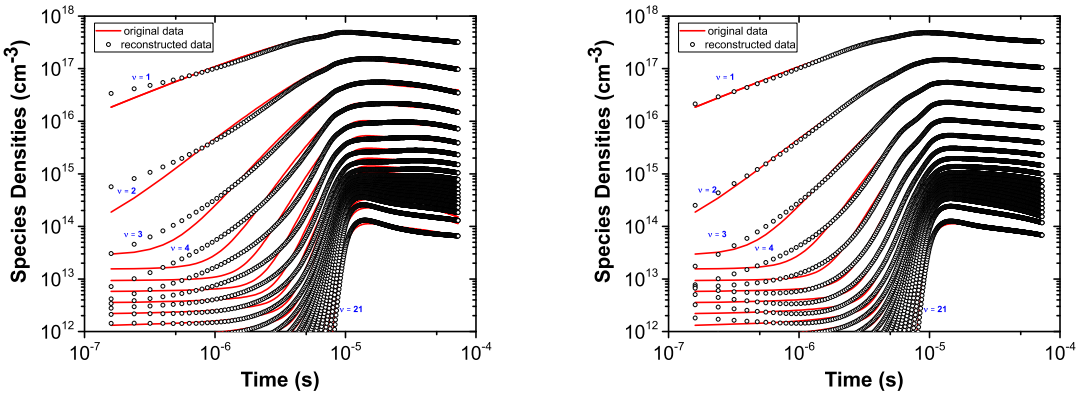

(a) 5 PCs. **(b)** 10 PCs.

Figure 5.5: ***Reconstruction of densities of asymmetric mode levels of CO_2 with 5 and 10 PCs. Range scaling and log-transformation were applied.***

Time integration Once the scores have been calculated and the number of principal components to be considered have been determined, the 0-D continuity equation can be solved for the PCs. This equation is derived in [65] and it is presented in the form (5.17):

$$\frac{\partial Z_k}{\partial t} = S_{Z_k} \tag{5.17}$$

where S_k is the source term of the kth PC for Z_k. The source terms for the principal components can be thus determined by (5.18):

$$S_{Z_k} = \sum_i a_{ik} \frac{S_{n_i}}{D_{ii}} \tag{5.18}$$

where the source term for the densities, S_{n_i}, is multiplied by the ith component of the kth PC a_{ik} and divided by the scaling factor D_{ii}. If *log-transformation* is applied the following modified formula (5.19) has to be taken into account for calculating the PC source terms:

$$S_{Z_k} = \sum_i a_{ik} \frac{S_{n_i}}{D_{ii} n_i} \tag{5.19}$$

In principle, it is possible to calculate the source terms for PC continuity equations from (5.18) or (5.19). However, it has been shown [65] [72] that even small errors in the new reconstructed densities strongly affects the accuracy of the source terms when the number of the retained PCs is decreased. This fact is due to the strong non-linearities in the source terms, thus a possible methods to handle this problem will be presented in Chapter 6.

5.3 Characterisation of the method

Sec.(5.2) was mainly focused on studying the different steps and assumptions of PCA applied on a CO_2 kinetic model. On the contrary, this Section is mostly related on discussing limitations and considerations about the method itself for future improvements.

Physical interpretation The PC scores are, by construction, linear combinations of the original variables. Therefore, their physical interpretation is usually not straightforward. In the model presented by Peeremboom et al. [65], the first two PC scores are shown to be correlated with the *CO yield conversion* and the *ionization degree* respectively. However, their interpretation in terms of physical quantities is not usually possible. For this reason, PCA generally is not useful to give insight about principal reactions or species, while it is an appropriate tool for finding a proper set of variables that describe a sub-manifold of the chemical state space.

Failures of the method Some important limitations of the method were found and one of these is underlined in this paragraph. In particular, all the simulations mentioned above are taken within a time range between $1.6{\cdot}10^{-7}$ s and $7.3{\cdot}10^{-5}$ s. This choice was appropriate to obtain better results from PCA, since a constant ionization degree (i.e. constant electron density) is present in that time range and no steep gradients on species densities are present. On the contrary, the PCA method seems to fail if the time range is extended up to the interval $2{\cdot}10^{-9}$ s $- 1.6{\cdot}10^{-4}$ s, where the electron density drops to zero. Results of reconstruction of densities using this extended time range are shown in Fig.(5.6b) for the case of range scaling and log-transformation (together the correspondent manifold shape in Fig.(5.6a)).

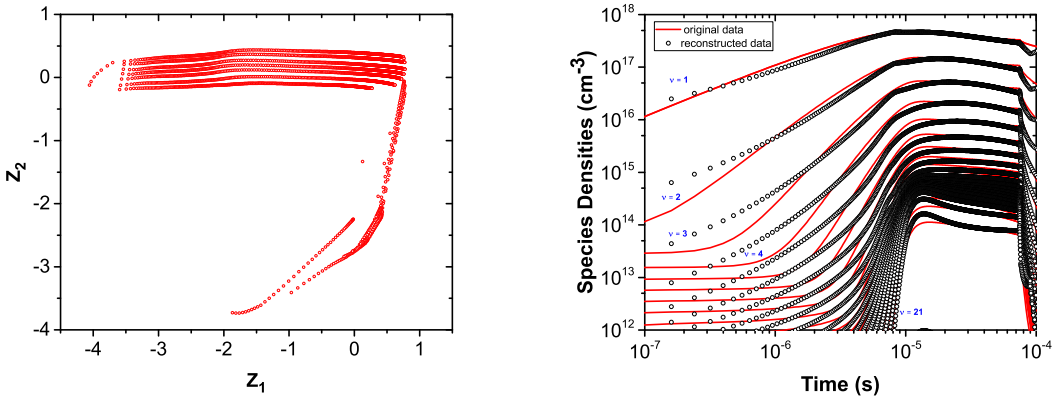

(a) Manifold. **(b)** Densities.

Figure 5.6: ***Reconstruction of densities of asymmetric mode levels of CO_2 (right) and correspondent manifold shape (left) using 10 PCs. Range scaling and log-transformation were applied.***

In Fig.(5.6b), it is possible to see that the reconstruction error of densities of asymmetric mode levels of CO_2 is enhanced. Moreover, problems of non-uniqueness in the manifold shape are found and are shown in Fig.(5.6a). These problems are mainly due to an intrinsic limit of PCA dealing with variables that present steep gradients (i.e. like the electron density on this case), since they can influence the reduction accuracy.

Future improvements According to [63], the PCA transformation can suffer from its reliance on second order statistics. In fact, the PCs are uncorrelated (i.e. their second-order product moment is zero), but they can still be highly statistically dependent. This is particularly important when relationships among the correlated variables are nonlinear, as it usually happens for a reacting system. In this case, PCA method fails and it need higher number of PCs for an accurate description. Different techniques were developed in combustion community to overcome this problem. One interesting method is known as Local

Principal Component Analysis (LPCA) and it was developed by Parente et al. [63]. Moreover, in this thesis a different approach was taken into account to overcome this problem and it is based on an extension of linear PCA to its non-linear version, which is presented in Chapter 6.

CHAPTER 6

Nonlinear Principal Component Analysis

Chapter 5 showed a complete PCA modelling approach whose principal consideration can be summarized here:

- PCs are identified according to the procedure in Sec.(5.1)
- A reduced number of PCs is selected in order to have enough accuracy with which the state variables are represented
- Continuity equations may be derived for each PCs

This procedure is schematized in Fig.(6.1) in which a backward linear transformation is applied to recover the original state variables.

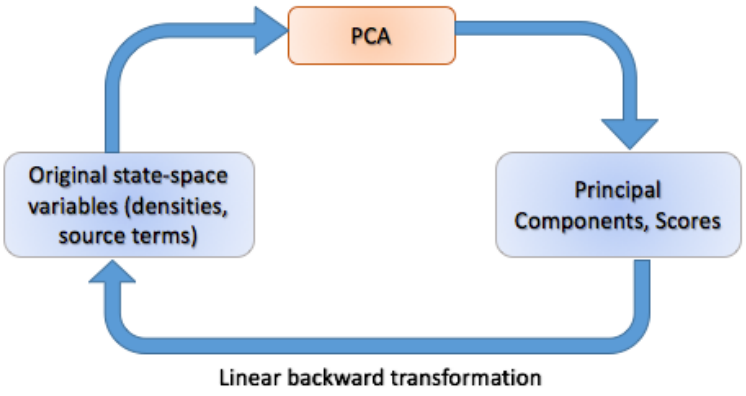

Figure 6.1: ***Schematic representation of standard PCA procedure: original state-space variables are used as input to perform PCA and to extract PCs scores. Linear backward transformation is applied to reconstruct the original variables from a reduced dataset of PCs.***

However, since high nonlinearities can be present in the system, the assumption of linearity in the PCA may be not suitable for an accurate description of the system. For this reason,

different approaches must be explored. In this Chapter, two different approaches to handle nonlinearities present in the system are proposed and applied for the first time to a simplified molecular argon plasma model. The aim is to compare different methods and suggest possible future implementations.

6.1 Nonlinear regression

In Chapter 5, studies about linear PCA showed that increasing the number of PCs will lead to more accurate reconstruction results to the detriment of the computational load. Moreover, inaccuracies on species densities will dramatically propagate on the calculation of the source terms. A recent studies [65] proposed a solution to these problems in a form of *linear interpolation* where species densities and source terms are tabulated as a function of two principal scores. In this Section, a different approach is presented using nonlinear regression to reconstruct species densities and source terms that are thus tabulated as a function of the PCs scores. The scheme of this method is shown in Fig.(6.2) , where the backward linear transformation in here substituted by the nonlinear regression to reconstruct the original dataset.

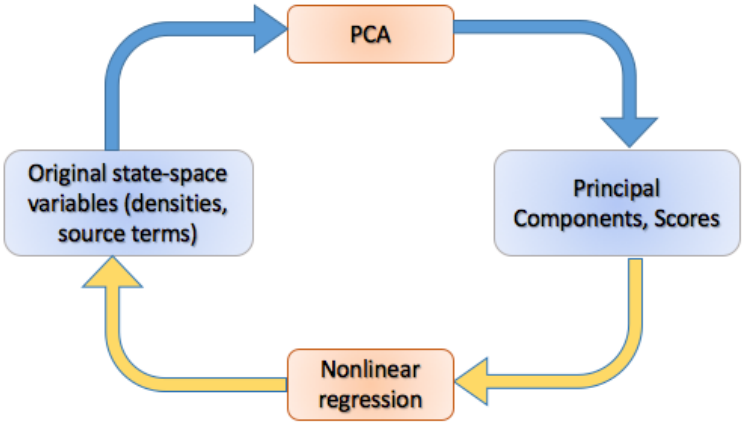

Figure 6.2: ***Schematic representation of PCA + nonlinear regression procedure: original state-space variables are used as input to perform PCA and to extract PCs scores. In this case, nonlinear regression is used to tabulate the PC scores as a function of the original variables in order to obtain better reconstruction (yellow path in figure).***

The advantage of this method is that the linear basis derived from the PC analysis allows to determine simple continuity equations, while using nonlinear functions within this basis allows capturing the nonlinearities that are always present in plasma chemistry systems.

6.1.1 Aim and assumptions

This section aims to show that source terms and species densities can be parametrized by PCs scores and tabulated *a-priori* to avoid run-time calculations. Moreover, accurate parametrization of source terms is fundamental for a successful application of PCA on plasma chemistry datasets.

The input model In this Section, nonlinear PCA methods are tested on a dataset consisting of a 0-D kinetic argon model where different non-linearities can be inserted on purpose on the system[1]. This model contains five levels [64]: the ground level (Ar), 4s metastable ($Ar(4s)^m$), 4s resonance ($Ar(4s)^r$), 4p (Ar(4p)), ion level (Ar^+). In addition molecular argon (Ar_2) and electrons are considered as input species leading to a total number of 7 species. The initial electron temperature is set at 32400 K, while the gas temperature is fixed during simulation time at a value of 300K. The gas pressure is set around 1.73 mbar and the electron density is calculated from quasi-neutrality conditions. The reactions included are mainly excitation, de-excitation and ionization processes included in Tab.(7) of Appendix B. Three different simulations were included in the training dataset for PCA input including different degrees of non-linearities in the system:

- *Simulation 1:* Non linearities in the reactions are considered by including three-body reactions. Rate coefficients are constant by fixing the electron temperature to the initial value during all simulation time.
- *Simulation 2:* Nonlinear dependence of rate coefficients on electron temperature is included by calculating the temperature run-time via the energy balance equation. Three-body reactions were removed by eliminating a species that occurs on both sides of the reaction and by multiplying the rate coefficient with the order of magnitude of the density of this species.
- *Simulation 3:* Both non-linearities in the reactions and rate coefficients discussed in Simulation 1 and 2 are considered via the inclusion of three-body reactions and evolution of electron temperature run-time.

Nonlinear MARS regression Nonlinear regression is used here to model the highly nonlinear state-space variables $\mathbf{\Phi}$ (i.e. densities or source terms) as a function of the PC scores $\mathbf{Z_q}$, as expressed generally by (6.1):

$$\mathbf{\Phi} = f_\Phi(\mathbf{Z_q}) \tag{6.1}$$

where f_Φ is the nonlinear regression function used as a model. In this Section, a specific regression method was used called Multivariate Adaptive Regression Splines (i.e. MARS) implemented in MATLAB®. The implementation of MARS present in the ARESLab package [73] was used and it is based on the method introduced by Friedman [74]. This method is able to fit local features in the curves by using β-splines. A β-spline consists of a set of fixed positions, called *knots*, and a piecewise smooth curve, called *basis function*, connecting each knot positions. The choice of this method is mainly due to three advantages:

- No assumptions are made about the specific regression function
- The method is *adaptive* so it selects the best combinations of basis functions that results in the largest reduction of the regression error.
- The method is also *multivariate* meaning that it is able to generate models based on several input variables (i.e. high dimensionality)

[1] Even if reaction rate coefficients are taken from literature [64], this is not a realistic argon model, but a simplification made in order to test the nonlinear methods in a contest where different nonlinearities are present

A fitted curve f to the data x can be represented with a linear combination of n β-splines, as referred in (6.2):

$$f(x) = a_0 + \sum_{j=1}^{n} a_j B_j(x, q) \tag{6.2}$$

where a_0 and a_j represents the different coefficients estimated by minimizing the residual sum of squares and they can be considered weights that represent the importance of the variable. Moreover, $B_j(x, q)$ is the corresponding basis function at the point x of degree q. The MARS algorithm iteratively selects a basis function that minimize the regression error until convergence is achieved. In this work, a lower order basis function (i.e. cubic) was selected to avoid overfitting of the data, while the training parameters for the fit are calculated automatically using the standard procedure implemented. A piecewise-cubic model was applied implementing a maximum large number of basis function (i.e. n is more than 100) to take into account all possible different non-linearities in the chemistry[2].

6.1.2 Application of the method

PCA is here applied to reconstruct *a-priori* both species densities and source terms. Comparison between results obtained from a standard version of linear PCA and PCA+MARS are given. It is important to notice that, in the case of linear PCA (i.e. Fig.(6.3a)), Ar and Ar_2 original and reconstructed densities are not even compatible.

Reconstruction of species densities In this part reconstruction of species densities using a coupled method of linear PCA and nonlinear MARS regression is performed as a test case for a first application. The training input dataset for PCA consists of 7 species aforementioned whose time evolution is calculated for 3 different simulations including some implicit nonlinear dependence between the variables. As expected, at least 5 PCs are required to accurately reconstruct the dataset when *range* scaling and *log-transformation* is applied. Example of species densities reconstruction for the dataset of *Simulation 3* (i.e. with nonlinearities in both rates and reactions) using 2 PCs and the backward linear transformation is shown in Fig.(6.3a). On the contrary, results applying PCA and MARS techniques are shown in Fig.(6.3b) and present a clearly enhanced reconstruction of species densities using only 2 PCs.

In order to quantify the error in representing the data in low-dimensional space parametrized by $\mathbf{Z}$, the R^2 statistic parameter is calculated, according to (6.3):

$$R^2 = 1 - \frac{\sum_{i=1}^{n}(y_i - y_i^*)^2}{\sum_{i=1}^{n}(y_i - \bar{y_i})^2} \tag{6.3}$$

where y is the original variable value, y^* is the predicted value from reconstruction, and $\bar{y}$ is the mean value of y. The values of R^2 for different species densities measure the accuracy with which the model represents the original data and are reported in Tab.(6.1).

The results of comparison between these two methods can be summarized in the following statements:

[2]Note that this is the maximum number of basis functions in the forward phase. This is arbitrary since it may not be reached by the model. The recommended value by Friedman [74] for this parameter is about two times the expected number of basis functions in the final model

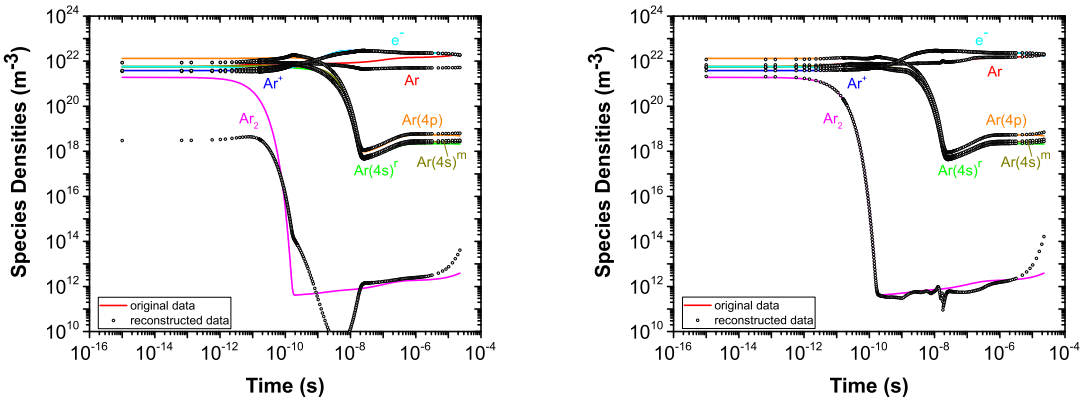

(a) Standard PCA. **(b)** PCA+MARS regression.

Figure 6.3: ***Comparison between reconstruction of species densities of Simulation 3 using standard PCA (left) and PCA+MARS (right) with 2 PCs. Range scaling and log-transformation were applied.***

Table 6.1: ***Comparison of R^2 values for the reconstruction of densities of 7 different species (of Simulation 3) using backward linear transformation implemented in standard PCA and PCA+MARS regression. In both cases log-transformation and range scaling were used.***

Species	R^2 (Standard PCA)	R^2 (PCA+MARS)
Ar	-	0.980
$Ar(4s)^r$	0.853	0.997
$Ar(4s)^m$	0.854	0.997
Ar(4p)	0.913	0.993
Ar^+	0.971	0.998
Ar_2	-	0.995
e^-	0.964	0.995

- The MARS representation gives more accurate results using a lower number of PCs than the direct PCA reconstruction (that leads sometimes to statistically incompatible results between the reconstructed model and the original one[3]).
- However, these results are obtained using high number of basis functions that is a drawback for the higher computational time required compared with Standard PCA.
- A non-constant electron temperature leads to high nonlinear dependencies in the reaction rate coefficients that influence the performance of the PCA method.

In order to study the implications of the last point, other calculations were performed adding the electron temperature as an input parameter in the original dataset. Results of these calculations are shown in Fig.(6.4a) and Fig.(6.4b) for *range* and *pareto* scaling respectively. As it can be seen from these figures, with the addition of T_e, *pareto* scaling performs better densities reconstruction than the *range* one. This is due to the fact that in this method the square root of the standard deviation is used to scale the variables so the relevance of the

[3]Reconstruction of Ar and Ar_2 using Standard PCA gives negative values of R^2 that means the model used to describe those species is incompatible with the original dataset.

temperature is enhanced with respect to the other variables of the state-space. This scaling procedure is equivalent to forcing the first PCs to align with the temperature.

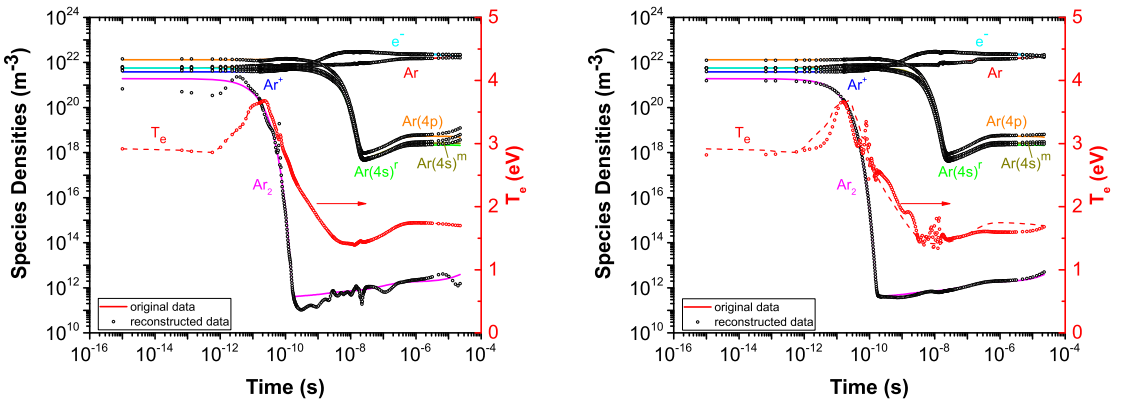

(a) PCA+MARS: range scaling. **(b)** PCA+MARS: pareto scaling.

Figure 6.4: ***Comparison between reconstruction of species densities and electron temperature (for Simulation 3) using 2 PCs with PCA+MARS method applying range scaling (left) and pareto scaling (right). Log-transformation was applied in both cases.***

In addition, another advantage of this scaling method can be seen in Fig.(6.5) where the eigenvalue magnitude for each PCs is plotted. Since high eigenvalues are measure of larger variance of the system, the first 2 PCs describe the majority of information of the dataset. This can be seen in Fig.(6.5b) for *pareto* scaling where more than 95% of the total variance is taken into account considering the firsts 2 PCs. On the contrary, "only" 90% of that is captured if *range* scaling is applied (i.e. Fig.(6.5a)). This reflects the fact that larger weights are associated with the first PCs if *pareto* scaling is applied.

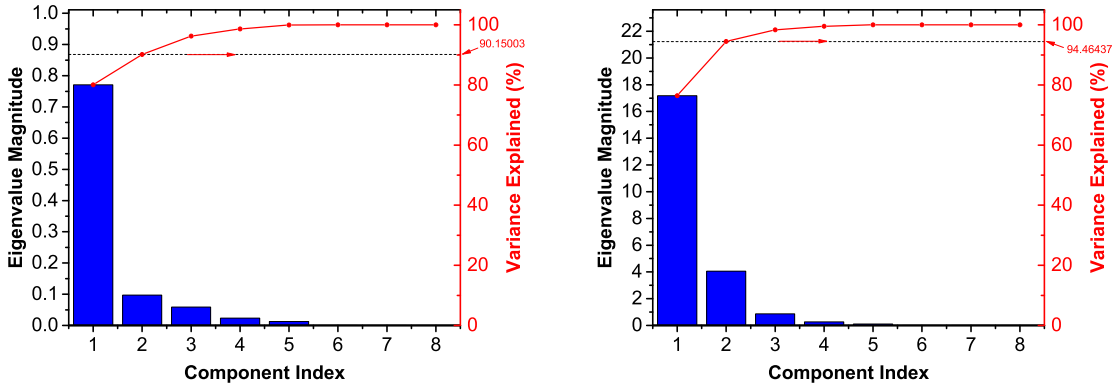

(a) PCA+MARS: range scaling. **(b)** PCA+MARS: pareto scaling.

Figure 6.5: ***Eigenvalue magnitude and correspondent variance for 8 different PCs. Range scaling (left) and pareto scaling (right) were applied in combination with log-transformation.***

Reconstruction of source terms PCs are not conserved variables[4], thus their source terms must be calculated to solve the continuity equation for the PCs scores. However, it has

[4]This is a statement that is generally valid if PC scores are deduced from the species densities that are deduced by solving a continuity equation

Table 6.2: ***Comparison of R^2 values for the reconstruction of 2 PC source terms using PCA+MARS regression for different scaling methods. Log-transformation was applied in every cases.***

PC source term	Range	Auto	Pareto	Level	Vast
S_{Z_1}	0.971	0.995	0.994	0.997	0.994
S_{Z_2}	0.993	0.989	0.996	0.996	0.997

been shown [75] that introduction of a small error in the reconstruction of the state-space variables can dramatically influence the calculations of the source terms. The error in many cases propagates exponentially due to the characteristic expression of the rate coefficients. The reason is that PCA transformation is applied on the state variables (i.e. densities, electron temperature, etc.) and it aims to find correlations between them, but it is not optimized for finding a basis function for the source terms. In addition, PC source terms $\mathbf{S_{Z_i}}$ present highly nonlinear dependence on the PC scores. For these reasons a nonlinear regression technique was used to create a model for $\mathbf{S_{Z_i}}$ as a function of $\mathbf{Z_i}$, where the training values for $\mathbf{S_{Z_i}}$ are calculated from the original dataset of species $\mathbf{X_i}$. The advantage of using this method is that approximation errors due to PCA is not propagated into the model for $\mathbf{S_{Z_i}}$. Tab.(6.2) shows the R^2 values for the regression of source terms for various scaling approaches, using 2 PCs. As the scaling greatly affects the manifold shape, it is interesting to see how it affects the ability to parametrize the source terms.

Results from Tab.(6.2) can lead to the following considerations:

- Looking at the range scaling method, PC source terms are parametrized with less accuracy than the state-space variables. This is obvious since the PCA technique is designed to find the optimal representation of these variables and this basis may not be optimal for describing the source terms.

- There is an influence of the choice of scaling on the accuracy of PC source terms. In particular, Pareto scaling gives more accurate results for reconstruction of species densities and source terms. On the contrary, Range scaling does not perform accurate results mostly due to non-linearities present in the system (e.g. variation of electron temperature).

6.2 Kernel Principal Component Analysis

Classical PCA investigates mainly the potential co-linearity between the variables. Thus it may not be completely adequate for complex data where the dependencies are nonlinear. For this reason, within the context of combustion [76] [77], recent investigations on the role of Kernel Principal Component Analysis (KPCA) as a nonlinear extension of PCA were performed. In this part of the work a version of KPCA was implemented on MATLAB® and tested on the reduced argon model aforementioned. Coupling with MARS regression was used to reconstruct the original variables, according to the scheme in Fig.(6.6).

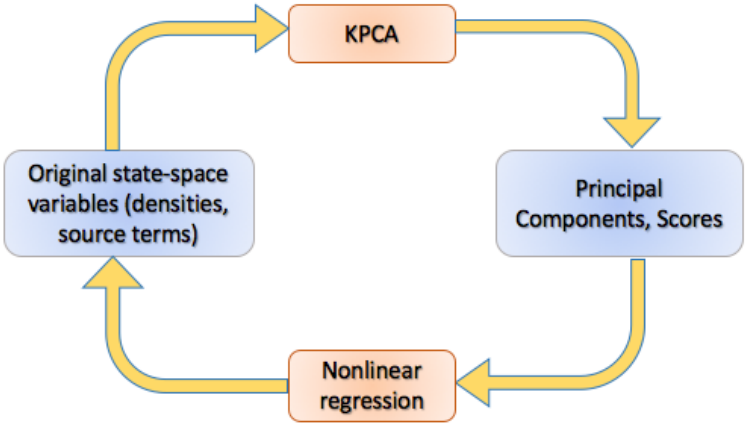

Figure 6.6: ***Schematic representation of KPCA + nonlinear regression procedure: original state-space variables are used as input to perform KPCA and to extract PCs scores in the feature space. Nonlinear regression is applied to reconstruct the original variables from a reduced dataset of PCs.***

6.2.1 Aim and assumptions

The goal of this work is to investigate whether KPCA can result in a more effective reduction of the original data while detecting non-linearity with respect to the standard linear PCA approach. The method is intuitively described here following the code implementation, while more accurate mathematical derivation can be found in [78].

Step 1: mapping in the feature space The main idea of the method is the same as PCA: it seeks to project the data onto a lower dimensional space that captures the highest possible amount of variance in the data. However, while PCA performs a linear separation, KPCA embeds the data in a higher dimensional space (i.e. called *feature space*) by a mapping function ψ and performs linear separation in that space [78]. In order to take an example, let's consider a three class problem with data $x_i \quad i = 1, 2$ in $\mathbb{R}^2$ plotted in Fig.(6.7a). These three class are represented by three concentric circles with different radii (i.e. $r_1 = 0$, $r_2 = 2$ and $r_3 = 5$ respectively), each composed by 50 points and generated from a normal random distribution (with polar angle θ uniformly distributed in $[0, \pi]$ and standard deviation equal to 0.1). Those data are clearly linearly inseparable in the input space, however they would have to be separated via a mapping from $\mathbb{R}^2$ to $\mathbb{R}^3$ (i.e. to the feature space), defined as (6.4):

$$\begin{aligned} \psi \colon X = \mathbb{R}^2 &\longrightarrow H = \mathbb{R}^3 \\ (x_1, x_2) &\mapsto (x_1, x_2, x_1^2 + x_2^2) \end{aligned} \tag{6.4}$$

In Fig.(6.7b) it is visible that a projection to an higher dimensional quadratic surface makes the problem linearly separable such that the centre can be separated with a plane. Standard PCA is now performed in the feature space in order to identify the sub-dimensional space in which the rings can be linearly separated. Final result of KPCA[5] applied in this 3-D space is shown in Fig.(6.7c) where the two datasets are completely distinguishable in the new projected space (Z_1, Z_2) and can be separated using only one component.

[5]Here Gaussian Kernel (with $\sigma = 0.99$) is applied for KPCA

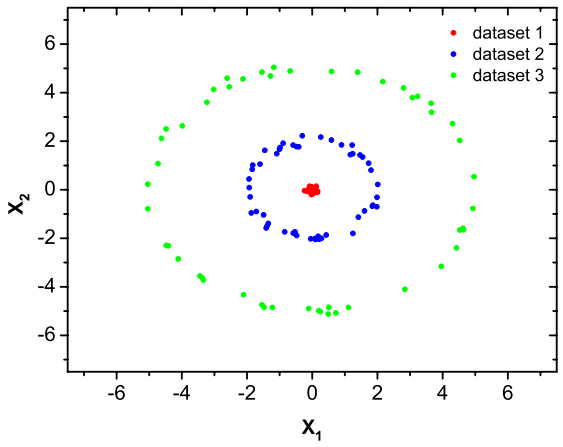

(a) Original training dataset.

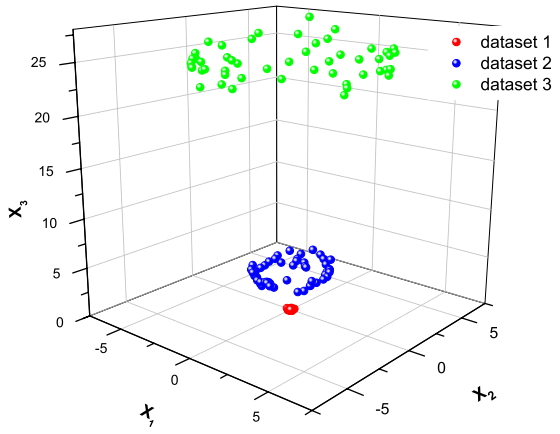

(b) Projection in 3-D feature space.

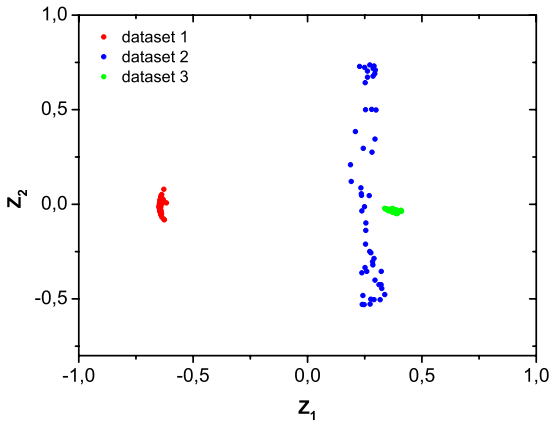

(c) Application of KPCA.

Figure 6.7: ***Original datasets (top) are mapped in an higher dimensional space (bottom left), then KPCA is applied in this 3-D space to make the problem linearly separable (bottom right).***

Step 2: choose a kernel function It has been shown that KPCA looks at linear dependencies in feature space that correspond to non-linear dependencies in the original space. However, due to high dimensionality, performing standard PCA in the new feature space can be extremely costly and inefficient. In addition, the best mapping ψ is not always known since variables can present some hidden (or non obvious) dependences between each other. Fortunately it is possible to use *kernel methods* to work in the high dimensional space without explicitly mapping into the space. This procedure is commonly known in literature as *kernel trick* and it is mathematically described in [79]. The main idea is that sometimes it is possible to compute dot-products without explicitly mapping in higher dimensional space. According to Mercer's theorem, this is done by defining the so called *kernel function* k that is calculated from the training dataset x_i. The main freedom of this procedure lies in choosing the kernel function. Some widely used kernels are the linear, polynomial and Gaussian kernels, given by:

- *Linear kernel:*

$$k(x_i, x_j) = x_i \cdot x_j \tag{6.5}$$

- *Polynomial kernel:*
$$k(x_i, x_j) = (x_i \cdot x_j + c)^d \tag{6.6}$$
where c is a constant and d is the degree of the polynomial

- *Gaussian kernel:*
$$k(x_i, x_j) = exp(- \parallel x_i - x_j \parallel^2 /(2\sigma^2)) \tag{6.7}$$
where σ is the typical gaussian parameter

The linear kernel (6.5) simply identifies the feature space with the input space. Implicitly, the polynomial kernel (6.6) maps the inputs into a feature space of dimensionality $O(D^d)$, while the Gaussian kernel (6.7) maps the inputs onto the surface of an infinite-dimensional sphere. It is worth noticing here that if the original input dataset $\mathbf{X}$ consists, for example, of different variables each of 100 observations, then the kernel function is indeed a matrix $\mathbf{K}$ of dimension 100×100. Thus the computational load cannot be negligible if large datasets are taken into account[6]. Three constrained criteria has to be mentioned for the definition of the kernel matrix:

- *Semipositive definiteness:* thus the matrix is symmetric with non-negative eigenvalues. This is necessary in order to define dot-products in the feature space.
- *Centering:* kernel matrix has to be centered in the feature space. This is important in order to interpret the eigenvalues of the kernel matrix as measures of variance along principal components in feature space. The numerical trick to implement this property is described in *Step 3*
- *Isometry:* this constraint restrict all the possible mapping by considering only transformations that preserves angles and distances in feature space

From these considerations it is immediately evident one important difference with respect standard PCA:

> While PCA is a technique that is not based on user experience, KPCA is a *parametric* analysis. It means that an a-priori knowledge on the dynamics of the system must be incorporated by the user. This is a difficulty since an optimal method to find the most appropriate kernel and parameters has to be determined, but it is also an advantage since the dynamics can be described more accurately.

An example of application of KPCA using different kernels is shown in Fig.(6.8) on a training set consisting on two concentric spheres (i.e. two classes are here considered). The total number of points considered for the entire input dataset is $N = 1000$, thus each class contains $N/2$ points distributed on a sphere of radius $r_1 = 40$ (in blue) and $r_2 = 100$ (in red). All three coordinates are perturbed by Gaussian noise of standard deviation 1. As expected, Fig.(6.8b) shows that application of standard PCA on this dataset does not reveal the nonlinear dependence between variables that is present in the original space. On the contrary, Fig.(6.8c) shows that applying KPCA with polynomial kernel (with $d = 5$ and $c = 1$) dataset 1 results clustered, while dataset 2 is scattered. The optimal results are obtained in Fig.(6.8d) with Gaussian kernel, whose datasets, after KPCA, becomes linearly separable in a 2-D space. The optimal choice of the σ parameter is discussed in [80] (and more generally in [81]) and computed automatically by the code such that σ is set to an optimal value large enough to capture only the neighbourhood information of each data point and smaller than the inter-class distance between the spheres.

[6]This aspect will be described better later in Sec.(6.3)

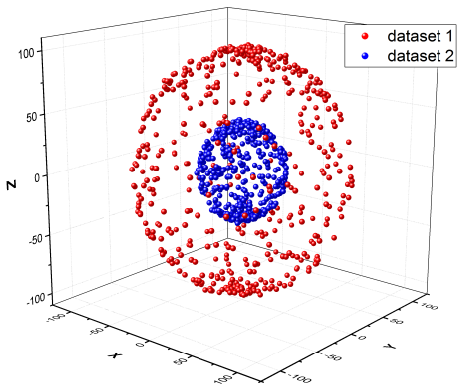

(a) Original training dataset.

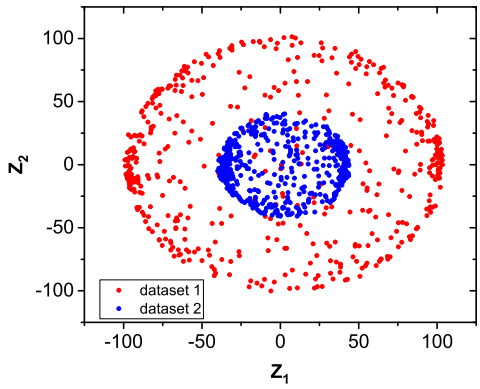

(b) Standard PCA.

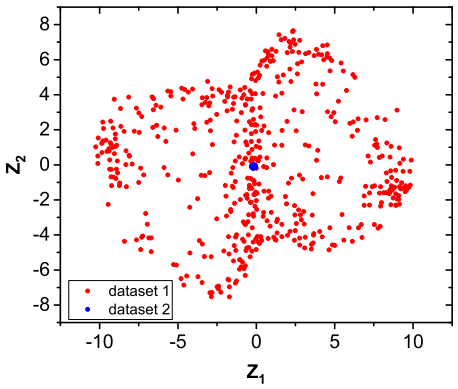

(c) KPCA: polynomial kernel ($d = 5$, $c = 1$).

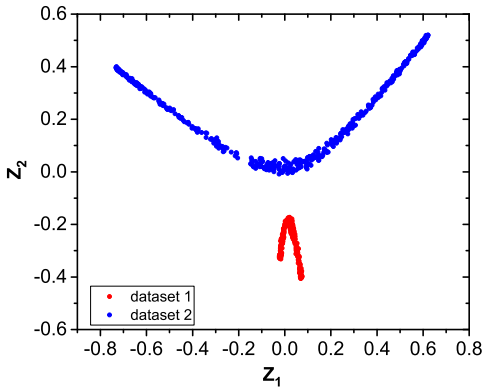

(d) KPCA: Gaussian kernel ($\sigma = 24.57$).

Figure 6.8: ***Application of standard PCA, KPCA with polynomial kernel*** *($d = 5$)* ***and KPCA with Gaussian kernel*** *($\sigma = 24.57$).*

Step 3: centering: One of the assumptions of the method is that projected data in feature space must be centered (i.e. have zero mean). Anyway it is not generally possible to center the data without knowing a-priori the mapping form. In this case, again linear algebra comes to help since it is sufficient to substitute the $N \times N$ kernel matrix $\mathbf{K}$ with the so called *Gram matrix* $\widetilde{\mathbf{K}}$ defined as (6.8):

$$\widetilde{\mathbf{K}} = \mathbf{K} - \mathbf{1}_N\mathbf{K} - \mathbf{K}\mathbf{1}_N + \mathbf{1}_N\mathbf{K}\mathbf{1}_N \tag{6.8}$$

where $\mathbf{1}_N$ is the $N \times N$ identity matrix where all elements are equal to $1/N$. The Gram matrix is generally the diagonalized form of the kernel matrix $\mathbf{K}$.

Step 4: solve the eigenvalue problem: Once the Gram matrix (of the correspondent kernel matrix) is calculated, the normal PCA procedure can be applied by computing the eigenvalues and eigenvectors of $\widetilde{\mathbf{K}}$. As described in [79], this procedure is mathematically equivalent of solving the eigenvalue problem for the covariance matrix in the feature space. Eigenvectors are then normalized by the square root of the eigenvalues. In the same way as standard PCA, only eigenvectors corresponding to larger eigenvalues are retained since the dominant eigenvalues of the kernel matrix are a measure of variance along the principal

components in feature space. Even if KPCA is just an extension of standard PCA based on linear algebra, two main differences have to be pointed out:

- KPCA is based on mapping the original manifold in higher dimensional space where PCA is performed. Thus, unlike the standard PCA procedure, this method allows the extraction of a number of PCs that can exceed the input dimension
- Being just a basis transformation, standard PCA allows to reconstruct the original dataset from a set of PCs using a backward transformation. On the contrary, in KPCA is more difficult and it is not always guaranteed that it is possible to find an exact reconstruction of the input space. This is referred in literature as the *problem of pre-image* and an analytical approximation for Gaussian kernel can be found in [80] [82].

6.2.2 Application of the method

In this section, validation of KPCA method is done by applying it to a plasma chemistry dataset in order to reconstruct species densities. In particular, the focus of this work is to determine a mapping that "unfolds" the manifold in feature space and to point out if a correct reconstruction of original state-space variables is indeed possible. In order to tabulate and reconstruct the original variables, MARS regression was coupled to the KPCA code. The input model is the reduced kinetic 0-D argon model aforementioned which considers 7 species and 3 different simulations. Since the choice of the kernel plays an important role in KPCA, two different kernels were used to reveal different types of low dimensional structure. Gaussian ($\sigma = 0.34$) and polynomial kernel ($d = 3$) were used to sample a low dimensional manifold.

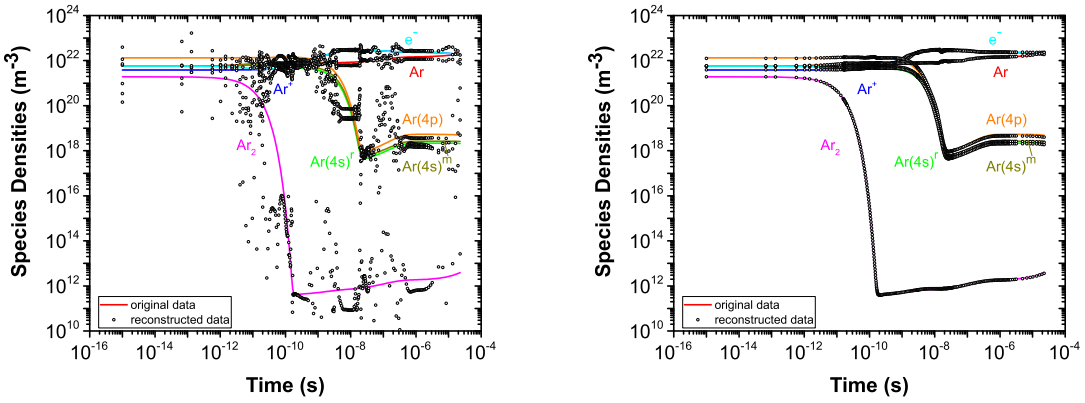

(a) Gaussian kernel ($\sigma = 0.34$). **(b)** Polynomial kernel ($d = 3$, $c = 1$).

Figure 6.9: ***Reconstruction of species densities of Simulation 3 using KPCA+MARS with Gaussian kernel (left) and polynomial kernel (right). Log transformation was applied in both cases.***

Fig.(6.9) shows the results of reconstruction of species densities of *Simulation 3* using KPCA+MARS taking into account 2 PCs and log-transformation. As a difference with respect the case before, Gaussian kernel (i.e. Fig.(6.9a)) performs badly in finding the optimal manifold in feature space. This is explained by the fact that this kernel is not suitable when steep gradients are present in the datasets. In fact, Gaussian kernel computes a nearly zero inner product (i.e. $K_{i,j} \sim 0$) in feature space for inputs x_i and x_j that do not belong to the same closely overlapping neighbourhoods. Thus, it follows that the feature vectors $\psi(x_i)$ and $\psi(x_j)$ must be nearly orthogonal. This fact is immediately visible in manifold shape of Fig.(6.10)

where the first 2 PCs are shown. As a result, the different simulations are mapped into orthogonal regions of the feature space such that, in this case, rather than unfolding the manifolds, Gaussian kernel leads to an embedding of it. For this reason, polynomial kernel clearly outperform the species densities reconstruction with respect to the Gaussian case. In fact, polynomial kernels have a very clear interpretation in terms of higher order features and are thus more suitable to take into account the dynamics of the system.

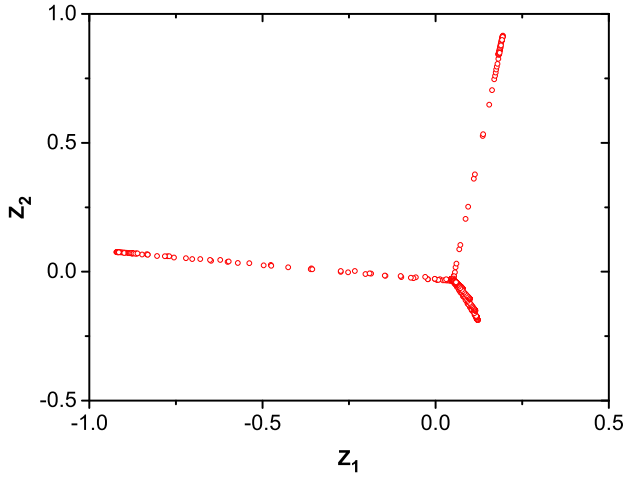

Figure 6.10: ***Manifold shape in feature space obtained from KPCA applied on the argon model. Gaussian kernel was used (with $\sigma = 0.34$). Three orthogonal directions are obtained in the manifold shape corresponding to the three different simulations included.***

6.3 Discussion and Next Steps

Nonlinear regression MARS nonlinear regression is a straightforward application to extract the state-space variables. This method is simpler as compared to other models like neural networks since it is an extension of linear methods that can model non-linearities. However, it is worth noticing here that log-transformation was always applied before using the PCA or KPCA procedure. This trick allows to a better tabulation of datasets for MARS regression that can lead even to negative densities if steep gradients are present in the data. Thus, it is important to investigate some other regression method that may lead to more accurate results without the necessity of implementing log-transformation. For this purpose, some recent works in combustion communities [76] [77] investigated the application of KPCA in combination of Associative Neural Networks (ANN) to tabulate and reconstruct the state-space variables. Moreover, some other different nonlinear regression techniques, like *Support Vector Regression* and *Gaussian Process Regression*, were suggested in [75]. Comparison between different linear and nonlinear techniques may also be useful to improve the performance of the methods in term of reconstruction and computational time. Another straightforward idea is to divide the PC state-space into clusters and to perform regression separately in each of these clusters. As a consequence a better regression will be obtained and the computational time will also be reduced.

Kernel Principal Component Analysis The choice of an optimal *kernel function* is crucial for a correct implementation of KPCA methods. In particular, in this Chapter it

was shown that Gaussian kernel performs better with synthetic random data by projecting it on a hypersphere, while polynomial kernel can handle high nonlinearities even in more complex datasets (e.g. in plasma chemistry datasets). Moreover, experience on KPCA showed that increasing the degree of the polynomial above three may lead to some problems in reconstruction of species densities accompanied by exponential increase of the computational time. For this reason, further refinements are needed in the code for an optimal *a-priori* kernel selections that can be based on learning techniques. Moreover, a fine tuning of the *parameters choice* can be implemented, following the work of [81]. Another technique to choose the proper parameters may be to test the performance of many different values on a randomly chosen subset, then using the values that perform best. This approach is known as *K-Fold Cross Validation* [78] [83]. Up to now, only the optimal choice of the σ for Gaussian kernel is implemented in the code used in this study. For conclusion, implementation of *scaling* in feature space may help to improve the manifold reconstruction (i.e. concerning smoothness and uniqueness) and to handle different state-space variables that presents larger variations in time.

Computational load Invariably, coupling of PCA (or KPCA) with MARS regression is more expensive than using linear regression from lookup tables to extract species densities and source terms, but the cost of both procedure can be completed within a maximum of half an hour per simulation using MATLAB® software and a stand-alone workstation. The main disadvantage of this method is that MARS regression needs a large amount of basis function to perform accurate results. Further studies may consider different methods aforementioned to decrease the computational time and improve reconstruction at the same time.

Future developments In this Chapter, a first application of non-linear PCA is presented and applied on a reduced argon model. The choice of this model is particularly adapted due to different non-linearities that are present in the three simulations included. However, even an extension of these methods is possible and it was tested on the larger CO_2 MW model exposed in Chapter 3 and 4. In this context, is it shown that MARS regression is a powerful technique to reconstruct species densities and source terms. This method, in combination with KPCA, may be an alternative to perform reduced simulations by solving the continuity equations only for the PCs, as suggested in [77].

CHAPTER 7

Conclusions

In recent years, studies about CO_2 conversion into chemicals and fuels are ongoing since such process can help in reducing the greenhouse gases emission while keeping a carbon-based economy. Developments of means to store solar energy in chemical bonds is the main objective of these studies. In this framework, non-equilibrium plasmas are optimal candidates as they can form chemically active species and enhance the overall CO_2 conversion. A roadmap to achieve optimal CO_2 conversion will benefit from the combined support of experimental work and modelling, which has to deal with different time and spatial scales ranging from the fast electronic excitation to the slow neutral gas dynamics. Moreover, complexity of plasma chemistry systems leads to difficulties on the interpretation of data and high computational load. Hence, in this thesis two *Parts* are developed in order to study a complex plasma chemistry system:

1. Analysis of CO_2 global model by simplification of the chemistry in order to find principal pathways in a CO_2 discharge.

2. Implementation of numerical reduction techniques in order to reduce the species and reactions considered, thus decreasing the computational time.

Part 1 focuses on a state-of-the-art CO_2 global model that is used to study the plasma dynamics. The model includes rate coefficients for each processes as input and allow deducing the time evolution of discharge species densities. Moreover, the time evolution of the electron temperature is calculated from the energy balance equation while assuming a Maxwellian energy distribution function for the electrons. One other main assumption is that the model densities and temperatures are spatially averaged, thus only their time dependence is considered. In this framework, a stepwise approach is considered that aims to study different subsystems present in the CO_2 chemistry. Within this part, Chapter 3 presents a study on neutral interactions happening in a CO_2 plasma in Local Thermodynamic Equilibrium. A comparison between a kinetic model implemented on PLASIMO and a thermodynamic model suggests that production of C-atoms is enhanced at temperatures higher than 5000 K due to thermal CO dissociation. Future implementations of the CO_2 model have to take into account this process. Moreover, balancing between forward and backward reactions lead to long

equilibration times (i.e. in the order of tenths of seconds) between neutral species suggesting that electron dynamics and excited states has to be taken into account for an appropriate description of discharge and post-discharge kinetics. In order to maximize the CO_2 conversion into CO, the backward inverse recombinations has to be minimized. Hence, in this thesis, two methods are numerically investigated to mitigate the effect of recombination and can be tested experimentally. The first idea is to reduce the rate of the recombination reactions by cooling down the plasma quickly (i.e. with a cooling rate higher than 10^6 K/s). This process lowers the recombination contribution by effect of thermal quenching. In addition, another idea is to remove some oxygen species from the plasma before cooling it down. The advantage of this technique is that higher conversion efficiencies are predicted even at lower cooling rates. Principal pathways in oxygen discharges were studied by comparing results from oxygen chemistry implemented in the CO_2 model of Koelman [21] and the Kemaneci model [43] developed to describe a microwave discharge that was already experimentally benchmarked. Comparison between those two models showed that $O(^1D)$ species have a relevant dynamics on oxygen discharge since it is mainly produced by electron impact splitting of O_2 during the pulse-phase. Since it is a metastable oxygen state, it influences the O_2 production even at longer times in the afterglow. In addition, production of ozone in the afterglow seems to be underestimated in the CO_2 model due to missing oxygen recombination reactions. Studying experimentally the equilibrium composition of O_3 and O_2 in the afterglow may help to validate the model and to highlight principal processes. Hints of carbon chemistry are presented in Chapter 3, where emission from C_2 species is suggested to be due to production of C_2O molecules. By studying the pathways involving this molecule, it is possible to deduce that its production is related with the presence of oxygen.

Chapter 4 presents a systematic study on a state-of-the art CO_2 global model, starting from a simplified chemistry, through the complete CO_2 model. Steady-state calculations are initially presented on a reduced CO_2 model in which excited states are neglected. In those calculations fixed electron density and temperature are assumed and results shows that both O and C-atoms are strongly influenced by the increase of electron temperature and density. Moreover, direct electron impact dissociation of CO_2 is found to be the dominant channel with respect ionization and dissociative ionization. Results of steady state calculations shows that the equilibration time is strongly influenced by the presence of excited states. In particular, this relaxation time is shown to decrease of one order of magnitude if electron impact excitation is considered. However, since electronic de-excitation mechanisms like spontaneous emission are not taken into account in the model, a population inversion between ground state species and electronically excited species is observed. Pulsed calculations using the reduced CO_2 model aforementioned were presented first by fixing externally the electron temperature, then by calculating it self-consistently with the electron energy balance equation (2.6). Results of pulsed calculations at high and low power density shows dominant neutral and charged species that can be checked experimentally by means, for example of mass spectrometry and laser induced fluorescence. Moreover, in all those calculations the role of oxygen dynamics is shown to be relevant. This suggest that a correct implementation of oxygen models is one key for improving the accuracy of CO_2 global models. At the end of the Chapter, results of pulsed calculations with the complete CO_2 model are shown. Comparing results of those calculations with the ones of Capitelli obtained in similar conditions, confirms that self consistent EEDF calculations are important for an accurate description of CO_2 vibrational distribution function. The CO_2 model used in this thesis seems more appropriate for describing CO_2 conversion processes happening in DBD conditions where micro-discharges of some nanoseconds are considered. Further extension of this model for describing longer pulses in the case of MW discharges has to be investigated in the future.

It is evident that current chemical CO_2 global models include complex chemical kinetics with numerous species and coupled networks of reactions. This induces challenges in the numerical implementations mostly due to the implied computational load. For this reason, *Part 2* of the thesis deals with implementing numerical reduction methods to lower the number of species. This method is called Principal Component Analysis (PCA), whose linear version is applied in Chapter 5 on a current CO_2 chemistry model, following the work of Peeremboom et al. [65]. The basic idea of this method is that the chemical state space (i.e. describing all the species and reaction rates) can be reduced to a lower dimensional manifold. The goal of PCA is thus to find an optimal parametrization of this subspace by looking into correlations in the chemistry. The intrinsic non-linear nature of the system, however, poses a serious challenge for obtaining an accurate reduction. For this reason, a nonlinear version of PCA was developed and applied to a simplified argon model that presents different nonlinearities intrinsically in the input chemistry. The choice of this reduced argon model was seen to be a good combination between a manageable model with challenging nonlinearities in the chemistry, but extension of this method to larger chemistries (i.e. like CO_2) showed promising results. Recommendations are highlighted to improve robustness and efficiency of the methods. The simulations in this thesis have all been limited to a zero dimension (i.e. no spatial components and transport are included). The nonlinear PCA method implemented, called *Kernel PCA*, was shown to provide good reconstruction by projecting the original dataset in higher dimensional space. Good accuracy is however accompanied by higher computational load with respect of PCA due to the higher dimension of the generated datasets. This fact has to be taken into account for future implementation of the method on larger models. In conclusion, all those numerical methods aim to be applied in higher dimensional 2D or 3D model in order to obtain a significant reduction of the computational time required for solving the continuity equation only for few principal components.

Appendix A

The tables presented in this Appendix A are taken from [21] and are kindly shared by Peter Koelman, PhD student in TU Eindhoven.

Table 1: ***The electron impact ionization and excitation reactions in this model, with the corresponding ID and reference from which the data originates. For the reaction ID is unchanged with respect to [8]. For an added reaction the ID ends with an additional a. Most, but not all, of the reactions are described by a cross section.***

No.	Reaction	Ref.	
X1	$\mathbf{e^- + CO_2 \rightarrow e^- + CO_2}$	[25]	a
X2	$\mathbf{e^- + CO_2 \rightarrow e^- + e^- + CO_2^+}$	[25]	a
X3	$\mathbf{e^- + CO_2 \rightarrow e^- + e^- + CO^+ + O}$	[46]	b
X4	$\mathbf{e^- + CO_2 \rightarrow e^- + e^- + C^+ + O_2}$	[46]	b
X5	$\mathbf{e^- + CO_2 \rightarrow e^- + e^- + O^+ + CO}$	[46]	b
X6 *	$\mathbf{e^- + CO_2 \rightarrow e^- + e^- + O_2^+ + C}$	[49]	d
X7	$\mathbf{e^- + CO_2 \rightarrow O^- + CO}$	[25]	b
X8	$\mathbf{e^- + CO_2 \rightarrow e^- + CO + O}$	[46]	b
X9	$\mathbf{e^- + CO_2 \rightarrow e^- + CO_2[e_1]}$	[25]	a
X10	$\mathbf{e^- + CO_2 \rightarrow e^- + CO_2[e_2]}$	[25]	a
X11	$\mathbf{e^- + CO_2 \rightarrow e^- + CO_2[v_a]}$	[25]	
X12	$\mathbf{e^- + CO_2 \rightarrow e^- + CO_2[v_b]}$	[25]	
X13	$\mathbf{e^- + CO_2 \rightarrow e^- + CO_2[v_c]}$	[25]	
X14	$\mathbf{e^- + CO_2 \rightarrow e^- + CO_2[v_d]}$	[25]	
X15	$\mathbf{e^- + CO_2 \rightarrow e^- + CO_2[v_1]}$	[25]	c
X16	$\mathbf{e^- + CO \rightarrow e^- + CO}$	[84]	a
X17	$\mathbf{e^- + CO \rightarrow e^- + e^- + CO^+}$	[85]	a
X18	$\mathbf{e^- + CO \rightarrow e^- + e^- + C^+ + O}$	[85]	b
X19	$\mathbf{e^- + CO \rightarrow e^- + e^- + O^+ + C}$	[85]	b
X20	$\mathbf{e^- + CO \rightarrow O^- + C}$	[84]	b
X20a *	$\mathbf{e^- + CO \rightarrow e^- + C + O}$	[57]	b
X21	$\mathbf{e^- + CO \rightarrow e^- + CO[e_1]}$	[84]	a
X22	$\mathbf{e^- + CO \rightarrow e^- + CO[e_2]}$	[84]	a
X23	$\mathbf{e^- + CO \rightarrow e^- + CO[e_3]}$	[84]	a

[a] The same cross section is used for the excited species.
[b] For vibrationally excited species the cross section of the ground state species is used. For electronically excited species scaling is used, which is shifting of the energy with the change of energy between the two species.
[c] The cross section is modified according to equation (4) of [8].

Table 2: ***Continue.***

No.	Reaction	Ref.
X24	$\mathbf{e^- + CO \rightarrow e^- + CO[e_4]}$	[84] [a]
X25 *	$\mathbf{e^- + CO \rightarrow e^- + CO[v_1]}$	[84] [c]
X26	$\mathbf{e^- + C \rightarrow e^- + C}$	[25]
X27	$\mathbf{e^- + C \rightarrow e^- + e^- + C^+}$	[25]
X29	$\mathbf{e^- + C_2 \rightarrow e^- + e^- + C + C}$	[86]
X30	$\mathbf{e^- + C_2 \rightarrow e^- + e^- + C_2^+}$	[86]
X31	$\mathbf{e^- + O_2 \rightarrow e^- + O_2}$	[24] [a]
X32	$\mathbf{e^- + O_2 \rightarrow e^- + O + O}$	[46] [b]
X33	$\mathbf{e^- + O_2 \rightarrow e^- + e^- + O_2^+}$	[24] [a]
X34	$\mathbf{e^- + O_2 \rightarrow e^- + e^- + O + O^+}$	[87] [b]
X35	$\mathbf{e^- + O_2 \rightarrow O^- + O}$	[24] [b]
X36	$\mathbf{e^- + O_2 \rightarrow e^- + O_2[v_1]}$	[24]
X37	$\mathbf{e^- + O_2 \rightarrow e^- + O_2[v_2]}$	[24]
X38	$\mathbf{e^- + O_2 \rightarrow e^- + O_2[v_3]}$	[24]
X39 *	$\mathbf{e^- + O_2 \rightarrow e^- + O_2[e_1]}$	[24] [a]
X40 *	$\mathbf{e^- + O_2 \rightarrow e^- + O_2[e_2]}$	[24] [a]
X41	$\mathbf{e^- + O_3 \rightarrow e^- + O_3}$	[25]
X42	$\mathbf{e^- + O_3 \rightarrow e^- + O_2 + O}$	[8]
X43	$\mathbf{e^- + O_3 \rightarrow e^- + e^- + O_2^+ + O}$	[8]
X44	$\mathbf{e^- + O_3 \rightarrow e^- + O^+ + O^- + O}$	[8]
X45	$\mathbf{e^- + O_3 \rightarrow O^- + O_2}$	[25]
X46	$\mathbf{e^- + O_3 \rightarrow O_2^- + O}$	[25]
X47	$\mathbf{e^- + O \rightarrow e^- + O}$	[25]
X48	$\mathbf{e^- + O \rightarrow e^- + e^- + O^+}$	[25]

[a] The same cross section is used for the vibrationally excited species.
[b] The cross section is modified according to equation (4) of [8] for vibrationally excited species. For electronically excited species the energy data from the LUT is shifted with the difference in energy between the species in the ground state and the electronically excited state. Consequently the threshold energy of the process equals the threshold energy in the (modified) LUT.
[c] The cross section is modified according to equation (4) of [8] for vibrationally excited species.
[d] For this reaction a rate coefficient is used, which reads:
$7.0 \times 10^{-19} T_e (1 + 1.3 \times 10^{-5} T_e) \exp(-1.5 \times 10^5 / T_e)$.

Table 3: ***Electron attachment and electron-ion recombination reactions. The reported rate coefficients have the units*** m^3/s ***or*** m^6/s***, with the gas temperature*** T_g ***in*** K ***and the electron temperature*** T_e ***in*** eV***.***

No.	Reaction	Rate coefficient	Ref
E1 *	$\mathbf{e^- + CO_2^+ \rightarrow CO[v_1] + O}$	$2.00 \cdot 10^{-11}\, T_e^{-0.5}\, T_g^{-1}$	[88, 89]
E2	$\mathbf{e^- + CO_2^+ \rightarrow C + O_2}$	$3.94 \cdot 10^{-13}\, T_e^{-0.4}$	[49]
E3	$\mathbf{e^- + CO_4^+ \rightarrow CO_2 + O_2}$	$1.61 \cdot 10^{-13}\, T_e^{-0.5}$	[49]
E4 *	$\mathbf{e^- + CO^+ \rightarrow C + O}$	$3.68 \cdot 10^{-14}\, T_e^{-0.55}$	[8]
E5	$\mathbf{e^- + C_2O_2^+ \rightarrow CO + CO}$	$4.0 \cdot 10^{-13}\, T_e^{-0.34}$	[38]
E6	$\mathbf{e^- + C_2O_3^+ \rightarrow CO_2 + CO}$	$5.4 \cdot 10^{-14}\, T_e^{-0.7}$	[38]
E7	$\mathbf{e^- + C_2O_4^+ \rightarrow CO_2 + CO_2}$	$2.0 \cdot 10^{-11}\, T_e^{-0.5}\, T_g^{-1}$	[38]
E8 *	$\mathbf{e^- + C2^+ \rightarrow C + C}$	$1.79 \cdot 10^{-14}\, T_e^{-0.5}$	[8]
E9 *	$\mathbf{e^- + O_2 + M \rightarrow O_2^- + M}$	$3.0 \cdot 10^{-42} \cdot A$ [a]	[38, 89]
E10 *	$\mathbf{e^- + O_3 + M \rightarrow O_3^- + M}$	$5.0 \cdot 10^{-43}$	[90]
E11	$\mathbf{e^- + O + M \rightarrow O^- + M}$	$1.0 \cdot 10^{-43}$	[38]
E12	$\mathbf{e^- + O_2^+ + M \rightarrow O_2 + M}$	$1.0 \cdot 10^{-38}$	[88]
E13	$\mathbf{e^- + O_2^+ \rightarrow O + O}$	$6.0 \cdot 10^{-13}\, T_e^{-0.5}\, T_g^{-0.5}$	[88, 89]
E14 *	$\mathbf{e^- + O^+ + M \rightarrow O + M}$	$2.49 \cdot 10^{-41}\, T_e^{-1.5}$	[38]
E15	$\mathbf{e^- + O_4^+ \rightarrow O_2 + O_2}$	$2.25 \cdot 10^{-13}\, T_e^{-0.5}$	[91]

[a] $A = 1$, 2/3 and 2/3 for $\mathbf{M = CO_2}$, $\mathbf{CO}$ and $\mathbf{O_2}$ respectively.

Table 4: ***The neutral-neutral interactions with the rate coefficients as they are included in the model, in units of*** m^3/s ***and*** m^6/s***. The coefficient*** α ***originates from [8], where the values are presented as estimates.***

No.	Reaction	rate	α	Ref
N1 *	$\mathbf{CO_2 + M \rightarrow CO + O + M}$	$1.81 \cdot 10^{-16} \exp(-49000/T_g)$	0.8	[92, 93]
N2	$\mathbf{CO_2 + O \rightarrow CO + O_2}$	$2.8 \cdot 10^{-17} \exp(-26500/T_g)$	0.5	[49, 93, 94]
N3 *	$\mathbf{CO_2 + C \rightarrow CO + CO}$	$\leq 1.0 \cdot 10^{-21}$		[38]
N4 *	$\mathbf{O + CO + M \rightarrow CO_2 + M}$	$8.2 \cdot 10^{-46} \exp(-1510/T_g) \cdot A$ [a]	0.0	[38, 93]
N5	$\mathbf{O_2 + CO \rightarrow CO_2 + O}$	$4.2 \cdot 10^{-18} \exp(-24000/T_g)$	0.5	[49, 93]
N6 *	$\mathbf{O_3 + CO \rightarrow CO_2 + O_2}$	$\leq 4.0 \cdot 10^{-31}$		[49, 93]
N7 *	$\mathbf{C + CO + M \rightarrow C_2O + M}$	$6.31 \cdot 10^{-44}$		[93, 95]
N8	$\mathbf{O_2 + C \rightarrow CO + O}$	$3.0 \cdot 10^{-17}$		[38, 93]
N9 *	$\mathbf{O + C + M \rightarrow CO + M}$	$2.14 \cdot 10^{-41} (T_g/300)^{-3.08} \exp(-2114/T_g)$		[49]
N10 *	$\mathbf{O + C_2O \rightarrow CO + CO}$	$9.51 \cdot 10^{-17}$		[96]
N11	$\mathbf{O_2 + C_2O \rightarrow CO_2 + CO}$	$3.3 \cdot 10^{-19}$		[38]
N12 *	$\mathbf{O + O_3 \rightarrow O_2 + O_2}$	$8.0 \cdot 10^{-18} \exp(-2056/T_g)$		[93, 96]
N13	$\mathbf{O_3 + M \rightarrow O_2 + O + M}$	$4.12 \cdot 10^{-16} \exp(-11430/T_g)$		[49]
N14 *	$\mathbf{O + O_2 + M \rightarrow O_3 + M}$	$5.51 \cdot 10^{-46} (T_g/298)^{-2.6}$		[97]
N15 *	$\mathbf{O + O + M \rightarrow O_2 + M}$	$5.2 \cdot 10^{-47} \exp(900/T_g)$		[94]

[a] $A = 2$, 1, 1 for $\mathbf{M = CO_2}$, $\mathbf{O_2}$ and $\mathbf{CO}$, respectively.

Table 5: ***The list of ion-neutral and ion-ion reactions and rate coefficients, with*** T_g ***the gas temperature in*** K ***and*** T_e ***the electron temperature in*** eV***. The rate coefficients are in units of*** m^3/s ***and*** m^6/s***. The ID corresponding to the reactions is kept the same as in [8].***

No.	Reaction	Rate coefficient	Ref
I1	$\mathbf{O_2^+ + CO_2 + M \rightarrow CO_4^+ + M}$	$2.3 \cdot 10^{-41}$	[49]
I2 *	$\mathbf{O^+ + CO_2 \rightarrow O_2^+ + CO}$	$8.1 \cdot 10^{-16}$	[49, 98]
I3 *	$\mathbf{O^+ + CO_2 \rightarrow CO_2^+ + O}$	$9.0 \cdot 10^{-17}$	[49, 98]
I4 *	$\mathbf{C^+ + CO_2 \rightarrow CO^+ + CO}$	$1.1 \cdot 10^{-15}$	[49, 98]
I5	$\mathbf{CO^+ + CO_2 \rightarrow CO_2^+ + CO}$	$1.0 \cdot 10^{-15}$	[38, 49, 88, 98]
I6 *	$\mathbf{O^- + CO_2 + M \rightarrow CO_3^- + M}$ [a]	$9.0 \cdot 10^{-41}$	[38]
I7 *	$\mathbf{O_2^- + CO_2 + M \rightarrow CO_4^- + M}$	$1.0 \cdot 10^{-41}$	[38]
I8	$\mathbf{O_3^- + CO_2 \rightarrow CO_3^- + O_2}$	$5.5 \cdot 10^{-16}$	[38, 88]
I9	$\mathbf{O_4^- + CO_2 \rightarrow CO_4^- + O_2}$	$4.8 \cdot 10^{-16}$	[38]
I10 *	$\mathbf{CO_2^+ + CO_2 + M \rightarrow C_2O_4^+ + M}$	$3.0 \cdot 10^{-40}$	[38]
I11	$\mathbf{O^+ + CO \rightarrow CO^+ + O}$	$4.9 \cdot 10^{-18}(T_g/300)^{0.5} \exp(-4580/T_g)$	[98]
I12	$\mathbf{O^- + CO \rightarrow CO_2 + e^-}$	$5.5 \cdot 10^{-16}$	[49, 98]
I13	$\mathbf{CO_3^- + CO \rightarrow CO_2 + CO_2 + e^-}$	$5.0 \cdot 10^{-19}$	[88]
I14	$\mathbf{C_2O_3^+ + CO \rightarrow CO_2 + C_2O_2^+}$	$1.1 \cdot 10^{-15}$	[38]
I15	$\mathbf{C_2O_4^+ + CO \rightarrow CO_2 + C_2O_3^+}$	$9.0 \cdot 10^{-16}$	[38]
I16 *	$\mathbf{C_2O_3^+ + CO + M \rightarrow CO_2 + C_2O_2^+ + M}$	$2.6 \cdot 10^{-38}$	[38]
I17 *	$\mathbf{C_2O_4^+ + CO + M \rightarrow CO_2 + C_2O_3^+ + M}$	$4.2 \cdot 10^{-38}$	[38]
I18	$\mathbf{C^+ + CO \rightarrow C + CO^+}$	$5.0 \cdot 10^{-19}$	[49]
I19	$\mathbf{CO^+ + C \rightarrow CO + C^+}$	$1.1 \cdot 10^{-16}$	[99]
I20	$\mathbf{O_2^+ + C \rightarrow CO^+ + O}$	$5.2 \cdot 10^{-17}$	[99]
I21	$\mathbf{O_2^+ + C \rightarrow C^+ + O_2}$	$5.2 \cdot 10^{-17}$	[99]
I22	$\mathbf{C_2^+ + C \rightarrow C_2 + C^+}$	$1.1 \cdot 10^{-16}$	[99]
I23	$\mathbf{CO_2^+ + O \rightarrow O_2^+ + CO}$	$1.64 \cdot 10^{-16}$	[99]
I24	$\mathbf{CO_2^+ + O \rightarrow O^+ + CO_2}$	$9.62 \cdot 10^{-17}$	[99]
I25	$\mathbf{CO_2^+ + O_2 \rightarrow O_2^+ + CO_2}$	$5.3 \cdot 10^{-17}$	[99]
I26 *	$\mathbf{CO_3^- + CO_2^+ \rightarrow CO_2[v_b] + CO_2[v_b] + O}$	$5.0 \cdot 10^{-13}$	[89]
I27 *	$\mathbf{CO_4^- + CO_2^+ \rightarrow CO_2[v_b] + CO_2[v_b] + O_2}$	$5.0 \cdot 10^{-13}$	[89]
I28 *	$\mathbf{CO_2^+ + O_2^- \rightarrow CO[v1] + O_2 + O}$	$6.0 \cdot 10^{-13}$	[89]
I29	$\mathbf{CO^+ + O \rightarrow CO + O^+}$	$1.4 \cdot 10^{-16}$	[99]
I30	$\mathbf{CO^+ + O_2 \rightarrow CO + O_2^+}$	$1.2 \cdot 10^{-16}$	[99]
I31	$\mathbf{C_2O_2^+ + O_2 \rightarrow CO + CO + O_2^+}$	$5.0 \cdot 10^{-18}$	[38]
I32	$\mathbf{C_2O_2^+ + M \rightarrow CO^+ + CO + M}$	$1.0 \cdot 10^{-18}$	[38]
I33	$\mathbf{C_2O_2^+ + CO_3^- \rightarrow CO_2 + CO + CO + O}$	$5.0 \cdot 10^{-13}$	[38]

[a] Multiplied by 1, 3.3, 3.3 for $\mathbf{M = CO_2, CO, O_2}$ respectively.

Table 5: ***Continued.***

No.	Reaction	Rate coefficient	Ref
I34	$\mathbf{C_2O_2^+ + CO_4^- \rightarrow CO_2 + CO + CO + O_2}$	$5.0 \cdot 10^{-13}$	[38]
I35	$\mathbf{C_2O_2^+ + O_2^- \rightarrow CO + CO + O_2}$	$6.0 \cdot 10^{-13}$	[38]
I36	$\mathbf{C_2O_3^+ + CO_3^+ \rightarrow CO_2 + CO_2 + CO + O}$	$5.0 \cdot 10^{-13}$	[38]
I37	$\mathbf{C_2O_3^+ + CO_4^- \rightarrow CO_2 + CO_2 + CO + O_2}$	$5.0 \cdot 10^{-13}$	[38]
I38	$\mathbf{C_2O_3^+ + O_2^- \rightarrow CO_2 + CO + O_2}$	$6.0 \cdot 10^{-13}$	[38]
I39 *	$\mathbf{C_2O_4^+ + M \rightarrow CO_2^+ + CO_2 + M}$	$1.0 \cdot 10^{-20}$	[38]
I40	$\mathbf{C_2O_4^+ + CO_3^- \rightarrow CO_2 + CO_2 + CO_2 + O}$	$5.0 \cdot 10^{-13}$	[38]
I41	$\mathbf{C_2O_4^+ + CO_4^- \rightarrow CO_2 + CO_2 + CO_2 + O_2}$	$5.0 \cdot 10^{-13}$	[38]
I42	$\mathbf{C_2O_4^+ + O_2^- \rightarrow CO_2 + CO_2 + O_2}$	$6.0 \cdot 10^{-13}$	[38]
I43 *	$\mathbf{O_2^+ + CO_3^- \rightarrow CO_2[v_b] + O_2 + O}$	$3.0 \cdot 10^{-13}$	[88]
I44 *	$\mathbf{O_2^+ + CO_4^- \rightarrow CO_2[v_b] + O_2 + O_2}$	$3.0 \cdot 10^{-13}$	[88]
I45	$\mathbf{CO_3^- + O \rightarrow CO_2 + O_2^-}$	$8.0 \cdot 10^{-17}$	[88]
I46	$\mathbf{CO_4^- + O \rightarrow CO_3^- + O_2}$	$1.1 \cdot 10^{-16}$	[49]
I47	$\mathbf{CO_4^- + O \rightarrow CO_2 + O_2 + O^-}$	$1.4 \cdot 10^{-17}$	[49]
I48	$\mathbf{CO_4^- + O \rightarrow CO_2 + O_3^-}$	$1.4 \cdot 10^{-17}$	[49]
I49	$\mathbf{CO_4^- + O_3 \rightarrow CO_2 + O_3^- + O_2}$	$1.3 \cdot 10^{-16}$	[38]
I50	$\mathbf{C^+ + O_2 \rightarrow CO + O^+}$	$4.54 \cdot 10^{-16}$	[99]
I51	$\mathbf{C^+ + O_2 \rightarrow CO^+ + O}$	$3.8 \cdot 10^{-16}$	[49]
I52	$\mathbf{O^+ + O_2 \rightarrow O_2^+ + O}$	$1.9 \cdot 10^{-17}(300/T_g)^{0.5}$	[49]
I53 *	$\mathbf{O_2^+ + O_2 + M \rightarrow O_4^+ + M}$	$2.4 \cdot 10^{-42}(300/T_g)^{3.2}$	[91]
I54 *	$\mathbf{O_2^- + O_2 + M \rightarrow O_4^- + M}$	$3.5 \cdot 10^{-43}(300/T_g)$	[91]
I55	$\mathbf{O^- + O_2 \rightarrow O_3 + e^-}$	$1.0 \cdot 10^{-18}$	[38]
I56 *	$\mathbf{O^- + O_2 + M \rightarrow O_3^- + M}$	$1.1 \cdot 10^{-42}(300/T_g)$	[38, 48, 91]
I57 *	$\mathbf{O^- + O_3 \rightarrow O + O_3^-}$	$5.3 \cdot 10^{-16}$	[38]
I58	$\mathbf{O^- + O_3 \rightarrow O_2 + O_2 + e^-}$	$3.0 \cdot 10^{-16}$	[100]
I59 *	$\mathbf{O_2^- + O_3 \rightarrow O_2 + O_3^-}$	$4.0 \cdot 10^{-16}$	[100]
I60	$\mathbf{O_3^- + O_3 \rightarrow O_2 + O_2 + O_2 + e^-}$	$3.0 \cdot 10^{-16}$	[38]
I61	$\mathbf{O^+ + O_3 \rightarrow O_2^+ + O_2}$	$1.0 \cdot 10^{-16}$	[91]
I62 *	$\mathbf{O^+ + O + M \rightarrow O_2^+ + M}$	$1.0 \cdot 10^{-41}$	[101]
I63 *	$\mathbf{O^- + O \rightarrow O_2 + e^-}$	$2.3 \cdot 10^{-16}$	[48]
I64	$\mathbf{O_2^- + O \rightarrow O_2 + O^-}$	$3.31 \cdot 10^{-16}$	[48, 91]
I65	$\mathbf{O_2^- + O \rightarrow O_3 + e^-}$	$1.5 \cdot 10^{-16}$	[48]
I66	$\mathbf{O_3^- + O \rightarrow O_3 + O^-}$	$1.0 \cdot 10^{-19}$	[100]
I67	$\mathbf{O_3^- + O \rightarrow O_2 + O_2 + e^-}$	$1.0 \cdot 10^{-19}$	[38]
I68	$\mathbf{O_3^- + O \rightarrow O_2^- + O_2}$	$2.5 \cdot 10^{-16}$	[38, 90]
I69	$\mathbf{O_4^- + O \rightarrow O_3^- + O_2}$	$4.0 \cdot 10^{-16}$	[91]
I70	$\mathbf{O_4^- + O \rightarrow O^- + O_2 + O_2}$	$3.0 \cdot 10^{-16}$	[91]
I71	$\mathbf{O_4^+ + O \rightarrow O_2^+ + O_3}$	$3.0 \cdot 10^{-16}$	[91]
I72 *	$\mathbf{O_2^- + O^+ + M \rightarrow O_3 + M}$	$1.0 \cdot 10^{-37}(300/T_g)^{2.5}$	[49]

Table 5: ***Continued.***

No.	Reaction	Rate coefficient	Ref
I73 *	$\mathbf{O_2^- + O^+ \rightarrow O_2 + O}$	$2.7 \cdot 10^{-13}(300/T_g)^{0.5}$	[48]
I74 *	$\mathbf{O_2^- + O_2^+ \rightarrow O_2 + O_2}$	$2.01 \cdot 10^{-13}(300/T_g)^{0.5}$	[48]
I75	$\mathbf{O_2^- + O_2^+ \rightarrow O_2 + O + O}$	$4.2 \cdot 10^{-13}$	[88]
I76 *	$\mathbf{O_2^- + O_2^+ + M \rightarrow O_2 + O_2 + M}$	$1.0 \cdot 10^{-37}(300/T_g)^{2.5}$	[49]
I77 *	$\mathbf{O_2^- + M \rightarrow O_2 + M + e^-}$	$2.7 \cdot 10^{-16}(300/T_g)^{-0.5}\exp(-5590/T_g)$	[49]
I79 *	$\mathbf{O_3^- + O_2^+ \rightarrow O_3 + O_2}$	$2.0 \cdot 10^{-13}(300/T_g)^{0.5}$	[48]
I80 *	$\mathbf{O_3^- + O_2^+ \rightarrow O_3 + O + O}$	$1.0 \cdot 10^{-13}(300/T_g)^{0.5}$	[48]
I81 *	$\mathbf{O_3^- + O^+ \rightarrow O_3 + O}$	$1.0 \cdot 10^{-13}(300/T_g)^{0.5}$	[49]
I82 *	$\mathbf{O_3^- + M \rightarrow O_3 + M + e^-}$	$2.3 \cdot 10^{-17}$	[49]
I84 *	$\mathbf{O^- + O^+ \rightarrow O + O}$	$4.0 \cdot 10^{-14}(300/T_g)^{0.43}$	[48]
I85 *	$\mathbf{O^- + O^+ + M \rightarrow O_2 + M}$	$1.0 \cdot 10^{-37}(300/T_g)^{2.5}$	[48]
I86 *	$\mathbf{O^- + O_2^+ \rightarrow O_2 + O}$	$2.6 \cdot 10^{-14}(300/T_g)^{0.44}$	[48]
I87 *	$\mathbf{O^- + O_2^+ \rightarrow O + O + O}$	$4.2 \cdot 10^{-13}(300/T_g)^{0.44}$	[48]
I88 *	$\mathbf{O^- + O_2^+ + M \rightarrow O_3 + M}$	$1.0 \cdot 10^{-37}(300/T_g)^{2.5}$	[49]
I89 *	$\mathbf{O^- + M \rightarrow O + M + e^-}$	$4.0 \cdot 10^{-18}$	[38]
I90 *	$\mathbf{O_4^- + M \rightarrow O_2^- + O_2 + M}$	$1.0 \cdot 10^{-16}\exp(-1044/T_g)$	[91]
I91 *	$\mathbf{O_4^+ + M \rightarrow O_2^+ + O_2 + M}$	$3.3 \cdot 10^{-12}(300/T_g)^4\exp(-5030/T_g)$	[91]

Table 6: ***The VV and VT reactions of CO_2, CO and O_2, with the corresponding rate coefficient, obtained from [8]. The anharmonicity parameter x_e is required when applying the VV and VT rate coefficient scaling laws.***

No.	Rate coefficient (m^3/s)	$x_e(\cdot 10^{-3})$	Ref	Note
V1	$\mathbf{CO_2v_a} + \mathbf{M} \rightarrow \mathbf{CO_2} + \mathbf{M}$ $7.14 \times 10^{-14} \exp(-177\, T_g^{-1/3} + 451\, T_g^{-2/3})$	0.0	[102]	a
V2a	$\mathbf{CO_2v_1} + \mathbf{M} \rightarrow \mathbf{CO_2v_a} + \mathbf{M}$ $4.25 \times 10^{-7} \exp(-407\, T_g^{-1/3} + 824\, T_g^{-2/3})$	3.7	[102]	b
V2b	$\mathbf{CO_2v_1} + \mathbf{M} \rightarrow \mathbf{CO_2v_b} + \mathbf{M}$ $8.57 \times 10^{-7} \exp(-404\, T_g^{-1/3} + 1096\, T_g^{-2/3})$	1.0	[102]	b
V2c	$\mathbf{CO_2v_1} + \mathbf{M} \rightarrow \mathbf{CO_2v_c} + \mathbf{M}$ $1.43 \times 10^{-11} \exp(-252\, T_g^{-1/3} + 685\, T_g^{-2/3})$	−15.6	[102]	b
V3	$\mathbf{COv_1} + \mathbf{M} \rightarrow \mathbf{CO} + \mathbf{M}$ $1.0 \times 10^{-18}\, T_g \exp(-150.7\, T_g^{-1/3})$	6.13	[103]	c
V4	$\mathbf{COv_1} + \mathbf{O_2} \rightarrow \mathbf{CO} + \mathbf{O_2}$ $3.19 \times 10^{-12} \exp(-289\, T_g^{-1/3})$	6.13	[102]	
V5	$\mathbf{O_2v_1} + \mathbf{M} \rightarrow \mathbf{O_2} + \mathbf{M}$ $1.30 \times 10^{-14} \exp(-158\, T_g^{-1/3})$	0.0	[102]	d
V6	$\mathbf{O_2v_1} + \mathbf{O_2} \rightarrow \mathbf{O_2} + \mathbf{O_2}$ $1.35 \times 10^{-18}\, T_g \exp(-137.9\, T_g^{-1/3})[1 - \exp(-2273/T_g)]^{-1}$	0.0	[103]	
V7a	$\mathbf{CO_2v_1} + \mathbf{CO_2} \rightarrow \mathbf{CO_2v_b} + \mathbf{CO_2v_a}$ $1.06 \times 10^{-11} \exp(-242\, T_g^{-1/3} + 633\, T_g^{-2/3})$	2.8	[102]	
V7b	$\mathbf{CO_2v_1} + \mathbf{CO_2} \rightarrow \mathbf{CO_2v_a} + \mathbf{CO_2v_b}$ $1.06 \times 10^{-11} \exp(-242\, T_g^{-1/3} + 633\, T_g^{-2/3})$	17.6	[102]	
V8	$\mathbf{CO_2v_1} + \mathbf{CO_2} \rightarrow \mathbf{CO_2} + \mathbf{CO_2v_1}$ $1.32 \times 10^{-16} (T_g/300)^{0.5}\, 250/T_g$	5.25	[104]	
V9	$\mathbf{COv_1} + \mathbf{CO} \rightarrow \mathbf{CO} + \mathbf{COv_1}$ $3.4 \times 10^{-16} (T_g/300)^{0.5}\, (1.64 \times 10^{-6}\, T_g + 1.61/T_g)$	6.13	[103]	
V10	$\mathbf{CO_2v_1} + \mathbf{CO} \rightarrow \mathbf{CO_2} + \mathbf{CO_2v_1}$ $4.8 \times 10^{-18} \exp(-153\, T_g^{-2/3})$	5.25; 6.13	[102]	

[a] The rate coefficient is multiplied with 1.0, 0.7 and 0.7 for $\mathbf{CO_2}$, $\mathbf{CO}$ and $\mathbf{O_2}$, respectively.
[b] The rate coefficient is multiplied with 1.0, 0.3 and 0.4 for $\mathbf{CO_2}$, $\mathbf{CO}$ and $\mathbf{O_2}$, respectively.
[c] The same rate coefficient for $\mathbf{M} = \mathbf{CO_2}$ and $\mathbf{CO}$.
[d] The rate coefficient is multiplied with 0.3 and 1.0 for $\mathbf{M} = \mathbf{CO_2}$ and $\mathbf{CO}$, respectively.

Appendix B

This section contains the reaction set that is included in the argon model, taken from [105].

Table 7: ***Reaction set included in argon model for application of non-linear PCA.***

No.	Reaction	Rate coefficient
(X1)	$Ar + e \rightarrow Ar(4s)^r + e$	$2.50 \cdot 10^{-15} T_e^{0.74} \exp(-11.56/T_e)$
(X2)	$Ar + e \rightarrow Ar(4s)^m + e$	$2.50 \cdot 10^{-15} T_e^{0.74} \exp(-11.56/T_e)$
(X3)	$Ar(4s)^r + e \rightarrow Ar + e$	$4.30 \cdot 10^{-16} T_e^{0.74}$
(X4)	$Ar(4s)^m + e \rightarrow Ar + e$	$4.30 \cdot 10^{-16} T_e^{0.74}$
(X5)	$Ar + e \rightarrow Ar(4p) + e$	$1.40 \cdot 10^{-14} T_e^{0.71} \exp(-13.20/T_e)$
(X6)	$Ar(4p) + e \rightarrow Ar + e$	$3.90 \cdot 10^{-16} T_e^{0.71}$
(X7)	$Ar(4s)^r + e \rightarrow Ar(4p) + e$	$8.90 \cdot 10^{-13} T_e^{0.51} \exp(-1.59/T_e)$
(X8)	$Ar(4s)^m + e \rightarrow Ar(4p) + e$	$8.90 \cdot 10^{-13} T_e^{0.51} \exp(-1.59/T_e)$
(X9)	$Ar(4p) + e \rightarrow Ar(4s)^r + e$	$1.50 \cdot 10^{-13} T_e^{0.51}$
(X10)	$Ar(4p) + e \rightarrow Ar(4s)^m + e$	$1.50 \cdot 10^{-13} T_e^{0.51}$
(X11)	$Ar(4s)^r + e \rightarrow Ar(4s)^m + e$	$3 \cdot 10^{-13}$
(X12)	$Ar(4s)^m + e \rightarrow Ar(4s)^r + e$	$2 \cdot 10^{-13}$
(X13)	$Ar + e \rightarrow Ar^+ + e + e$	$2.30 \cdot 10^{-14} T_e^{0.68} \exp(-15.76/T_e)$
(X14)	$Ar(4s)^r + e \rightarrow Ar^+ + e + e$	$6.80 \cdot 10^{-15} T_e^{0.67} \exp(-4.20/T_e)$
(X15)	$Ar(4s)^m + e \rightarrow Ar^+ + e + e$	$6.8 \cdot 10^{-15} T_e^{0.67} \exp(-4.20/T_e)$
(X16)	$Ar(4p) + e \rightarrow Ar^+ + e + e$	$1.8 \cdot 10^{-13} T_e^{0.61} \exp(-2.61/T_e)$
(X17)	$Ar_2^+ + e \rightarrow Ar(4s)^r + Ar$	$0.6 \cdot 10^{-12} (T_e/300)^{0.66}$
(X18)	$Ar_2^+ + e \rightarrow Ar(4s)^m + Ar$	$0.6 \cdot 10^{-12} (T_e/300)^{0.66}$
(X19)	$Ar^+ + e + e \rightarrow Ar + e$	$8.75 \cdot 10^{-39} T_e^{-4.5}$
(X20)	$Ar^+ + Ar + Ar \rightarrow Ar_2^+ + Ar$	$2.25 \cdot 10^{-43} (T_h/300)^{-0.40}$
(X21)	$Ar_2^+ + e \rightarrow Ar^+ + Ar + e$	$1.11 \cdot 10^{-12} \exp\left(-\frac{2.94-3(T_h-0.026)}{T_e}\right)$
(X22)	$Ar_2^+ + Ar \rightarrow Ar^+ + Ar + Ar$	$5.22 \cdot 10^{-16} T_h^{-1.00} \exp(-1.304/T_h)$
(X23)	$Ar(4s)^r \rightarrow Ar$	$1 \cdot 10^5$
(X24)	$Ar(4p) \rightarrow Ar(4s)^r$	$3.2 \cdot 10^7$
(X25)	$Ar(4p) \rightarrow Ar(4s)^m$	$3 \cdot 10^7$

Bibliography

[1] EC-European Commission et al. A resource-efficient europe-flagship initiative under the europe 2020 strategy. *Communication (COM (2011) 21)*, 2011.

[2] Elsje Alessandra Quadrelli, Gabriele Centi, Jean-Luc Duplan, and Siglinda Perathoner. Carbon dioxide recycling: Emerging large-scale technologies with industrial potential. *ChemSusChem*, 4(9):1194–1215, 2011.

[3] Markus Lehner, Robert Tichler, Horst Steinmüller, and Markus Koppe. *Power-to-gas: technology and business models*. Springer, 2014.

[4] Tu/e website. http://www.tue.nl/en/education/tue-graduate-school/phd-programs/phd-programs/phd-program-sustainable-energy-technology/research-groups/research-groups-applied-physics/plasma-and-materials-processing-pmp/research/research-areas/co2-neutral-fuels/. Accessed: 2017-09-02.

[5] Adelbert PH Goede, Waldo A Bongers, Martijn F Graswinckel, Richard MCM van de Sanden, Martina Leins, Jochen Kopecki, Andreas Schulz, and Mathias Walker. Production of solar fuels by CO_2 plasmolysis. In *EPJ Web of Conferences*, volume 79, page 01005. EDP Sciences, 2014.

[6] APH Goede. CO_2-neutral fuels. In *EPJ Web of Conferences*, volume 98, page 07002. EDP Sciences, 2015.

[7] Christopher Ronald Graves. *Recycling Carbon Dioxide into Sustainable Hydrocarbon Fuels: Electrolysis of Carbon Dioxide and Water*. Columbia University, 2010.

[8] Tomáš Kozák and Annemie Bogaerts. Splitting of CO_2 by vibrational excitation in non-equilibrium plasmas: a reaction kinetics model. *Plasma Sources Science and Technology*, 23(4):045004, 2014.

[9] Alexander Fridman. *Plasma chemistry*. Cambridge university press, 2008.

[10] GJ Van Rooij, DCM van den Bekerom, N den Harder, T Minea, G Berden, WA Bongers, R Engeln, MF Graswinckel, E Zoethout, and MCM van de Sanden. Taming microwave plasma to beat thermodynamics in CO_2 dissociation. *Faraday discussions*, 183:233–248, 2015.

[11] Claire Tendero, Christelle Tixier, Pascal Tristant, Jean Desmaison, and Philippe Leprince. Atmospheric pressure plasmas: A review. *Spectrochimica Acta Part B: Atomic Spectroscopy*, 61(1):2–30, 2006.

[12] Ruhr-universität bochum website. http://www.ep2.ruhr-uni-bochum.de/index.php/research/plasma-medicine. Accessed: 2017-09-07.

[13] S Ponduri. Understanding CO_2 containing non-equilibrium plasmas: modeling and experiments. 2016.

[14] Alp Ozkan. *CO_2 splitting in a dielectric barrier discharge plasma: understanding of physical and chemical aspects*. PhD thesis, University of Antwerp, 2016.

[15] Annemie Bogaerts, Tomas Kozák, Koen van Laer, and Ramses Snoeckx. Plasma-based conversion of CO_2: current status and future challenges. *Faraday discussions*, 183:217–232, 2015.

[16] Martina Leins, Sandra Gaiser, Andreas Schulz, Matthias Walker, Uwe Schumacher, and Thomas Hirth. How to ignite an atmospheric pressure microwave plasma torch without any additional igniters. *Journal of visualized experiments: JoVE*, (98), 2015.

[17] Jon D Grandy, Peter C Kong, Brent A Detering, and Larry D Zuck. Plasma processing of hydrocarbon. Technical report, Idaho National Laboratory (INL), 2007.

[18] Robby Aerts, Wesley Somers, and Annemie Bogaerts. Carbon dioxide splitting in a dielectric barrier discharge plasma: a combined experimental and computational study. *ChemSusChem*, 8(4):702–716, 2015.

[19] C Lee and MA Lieberman. Global model of Ar, O_2, Cl_2, and Ar/O_2 high-density plasma discharges. *Journal of Vacuum Science & Technology A: Vacuum, Surfaces, and Films*, 13(2):368–380, 1995.

[20] Kerson Huang. Statistical mechanics, 2nd. *Edition (New York: John Wiley & Sons)*, 1987.

[21] Peter Koelman, Stijn Heijkers, Samaneh Tadayon Mousavi, Wouter Graef, Diana Mihailova, Tomas Kozak, Annemie Bogaerts, and Jan van Dijk. A comprehensive chemical model for the splitting of CO_2 in Non-Equilibrium Plasmas. *Plasma Processes and Polymers*, 14(4-5), 2017.

[22] GJM Hagelaar and LC Pitchford. Solving the Boltzmann equation to obtain electron transport coefficients and rate coefficients for fluid models. *Plasma Sources Science and Technology*, 14(4):722, 2005.

[23] Miles M Turner. Uncertainty and sensitivity analysis in complex plasma chemistry models. *Plasma Sources Science and Technology*, 25(1):015003, 2015.

[24] AV Phelps and LC Pitchford. Technical Report# 26. *JILA Information Center Report*, 1985.

[25] JJ Lowke, AV Phelps, and BW Irwin. Predicted electron transport coefficients and operating characteristics of CO_2–N_2–He laser mixtures. *Journal of Applied Physics*, 44(10):4664–4671, 1973.

[26] LXcat IST-Lisbon database. www.lxcat.net. Retrieved on february 17, 2015.

[27] Jan Van Dijk, Kim Peerenboom, Manuel Jimenez, Diana Mihailova, and Joost Van der Mullen. The plasma modelling toolkit Plasimo. *Journal of Physics D: Applied Physics*, 42(19):194012, 2009.

[28] Manuel Jimenez Diaz. *Modelling of microwave induced plasmas*. PhD thesis, PhD Thesis, 2011.

[29] WAAD Graef. Zero-dimensional models for plasma chemistry. 2012.

[30] Alan C Hindmarsh. LSODE and LSODI, two new initial value ordinary differential equation solvers. *ACM Signum Newsletter*, 15(4):10–11, 1980.

[31] Sanford Gordon and Bonnie J McBride. NASA Reference Publication, 1311. 1994.

[32] Bonnie J McBride and Sanford Gordon. NASA Reference Publication 1311. 1996.

[33] Michael A Lieberman and Alan J Lichtenberg. *Principles of plasma discharges and materials processing*, pages 207–231. John Wiley & Sons, 2005.

[34] Niek den Harder, Dirk van den Bekerom, Richard S Al, Martijn F Graswinckel, Jose M Palomares, Floran JJ Peeters, Srinath Ponduri, Teofil Minea, Waldo A Bongers, Mauritius van de Sanden, et al. Homogeneous CO_2 conversion by microwave plasma: Wave propagation and diagnostics. *Plasma Processes and Polymers*, 14(6), 2017.

[35] Yu P Butylkin, AA Grinenko, AA Levitskii, LS Polak, NM Rytova, and DI Slovetskii. Mathematical-modeling of the kinetics of the thermal-decomposition of carbon-dioxide in an electric-arc discharge and quenching of the products. *HIGH ENERGY CHEMISTRY*, 13(6):456–461, 1979.

[36] Robby Aerts, Ramses Snoeckx, and Annemie Bogaerts. In-situ chemical trapping of oxygen in the splitting of carbon dioxide by plasma. *Plasma Processes and Polymers*, 11(10):985–992, 2014.

[37] Shinsuke Mori and Lin Lin Tun. Synergistic CO_2 conversion by hybridization of dielectric barrier discharge and solid oxide electrolyser cell. *Plasma Processes and Polymers*, 14(6), 2017.

[38] A Cenian, A Chernukho, and V Borodin. Modeling of plasma-chemical reactions in gas mixture of CO_2 lasers II. theoretical Model and its Verification. *Contributions to Plasma Physics*, 35(3):273–296, 1995.

[39] Shinsuke Mori and Masaaki Suzuki. The role of C_2 in low temperature growth of carbon nanofibers. *JOURNAL OF CHEMICAL ENGINEERING OF JAPAN*, 42(Supplement.):s249–s254, 2009.

[40] SS Prasad and WT Huntress Jr. A model for gas phase chemistry in interstellar clouds. I-The basic model, library of chemical reactions, and chemistry among C, N, and O compounds. *The Astrophysical Journal Supplement Series*, 43:1–35, 1980.

[41] P Caubet and G Dorthe. Origin of C_2 high-pressure bands observed in the products of a microwave discharge through CO. *Chemical physics letters*, 218(5-6):529–536, 1994.

[42] Federico D'Isa, private communication. IPP-Garching. 2017-09-07.

[43] Efe Kemaneci, Emile Carbone, Manuel Jimenez-Diaz, Wouter Graef, Sara Rahimi, Jan van Dijk, and Gerrit Kroesen. Modelling of an intermediate pressure microwave oxygen discharge reactor: from stationary two-dimensional to time-dependent global (volume-averaged) plasma models. *Journal of Physics D: Applied Physics*, 48(43):435203, 2015.

[44] Miles M Turner. Uncertainty and error in complex plasma chemistry models. *Plasma Sources Science and Technology*, 24(3):035027, 2015.

[45] Efe Hasan Kemaneci. *Modelling of plasmas with complex chemistry: application to microwave deposition reactors*. PhD thesis, PhD Thesis, 2014.

[46] Y Itikawa and A Ichimura. Cross sections for collisions of electrons and photons with atomic oxygen. *Journal of Physical and Chemical Reference Data*, 19(3):637–651, 1990.

[47] MA Mangan, BG Lindsay, and RF Stebbings. Absolute partial cross sections for electron-impact ionization of CO from threshold to 1000 eV. *Journal of Physics B: Atomic, Molecular and Optical Physics*, 33(17):3225, 2000.

[48] Jon Tomas Gudmundsson and EG Thorsteinsson. Oxygen discharges diluted with argon: dissociation processes. *Plasma Sources Science and Technology*, 16(2):399, 2007.

[49] Thomas G Beuthe and Jen-Shih Chang. Chemical Kinetic Modelling of Non-Equilibrium Ar-CO_2 thermal plasmas. *Japanese Journal of applied physics*, 36(7S):4997, 1997.

[50] PC Cosby. Electron-impact dissociation of oxygen. *The Journal of chemical physics*, 98(12):9560–9569, 1993.

[51] EG Thorsteinsson and JT Gudmundsson. The low pressure Cl_2/O_2 discharge and the role of ClO. *Plasma Sources Science and Technology*, 19(5):055008, 2010.

[52] DV Lopaev, EM Malykhin, and SM Zyryanov. Surface recombination of oxygen atoms in O_2 plasma at increased pressure: II. Vibrational temperature and surface production of ozone. *Journal of Physics D: Applied Physics*, 44(1):015202, 2010.

[53] Daniil Marinov, Vasco Guerra, Olivier Guaitella, Jean-Paul Booth, and Antoine Rousseau. Ozone kinetics in low-pressure discharges: vibrationally excited ozone and molecule formation on surfaces. *Plasma Sources Science and Technology*, 22(5):055018, 2013.

[54] Waldo Bongers, Henny Bouwmeester, Bram Wolf, Floran Peeters, Stefan Welzel, Dirk van den Bekerom, Niek den Harder, Adelbert Goede, Martijn Graswinckel, Pieter Willem Groen, et al. Plasma-driven dissociation of CO_2 for fuel synthesis. *Plasma processes and polymers*, 14(6), 2017.

[55] M Capitelli, G Colonna, G D'Ammando, and LD Pietanza. Self-consistent time dependent vibrational and free electron kinetics for CO_2 dissociation and ionization in cold plasmas. *Plasma Sources Science and Technology*, 26(5):055009, 2017.

[56] Hiroshi Shimamori and Richard W Fessenden. Thermal electron attachment to oxygen and van der Waals molecules containing oxygen. *The Journal of Chemical Physics*, 74(1):453–466, 1981.

[57] Philip C Cosby and Hanspeter Helm. Dissociation rates of diatomic molecules. Technical report, SRI INTERNATIONAL MENLO PARK CA, 1992.

[58] LD Pietanza, G Colonna, V Laporta, R Celiberto, G D Ammando, A Laricchiuta, and M Capitelli. Influence of electron molecule resonant vibrational collisions over the symmetric mode and direct excitation-dissociation cross sections of CO_2 on the electron energy distribution function and dissociation mechanisms in cold pure CO_2 plasmas. *The Journal of Physical Chemistry A*, 120(17):2614–2628, 2016.

[59] Mario Capitelli. *Nonequilibrium vibrational kinetics*, volume 39. Springer Science & Business Media, 2012.

[60] Javier Fernandez de la Fuente, SH Moreno, AI Stankiewicz, and GD Stefanidis. A new methodology for the reduction of vibrational kinetics in non-equilibrium microwave plasma: application to CO_2 dissociation. *Reaction Chemistry & Engineering*, 1(5):540–554, 2016.

[61] Ulrich Maas and Stephen B Pope. Simplifying chemical kinetics: intrinsic low-dimensional manifolds in composition space. *Combustion and flame*, 88(3):239–264, 1992.

[62] Harold Hotelling. Analysis of a complex of statistical variables into principal components. *Journal of educational psychology*, 24(6):417, 1933.

[63] Alessandro Parente. *Experimental and numerical investigation of advanced systems for hydrogen-based fuel combustion*. PhD thesis, Ph. D. Thesis, Università di Pisa, 2008.

[64] T Rehman, E Kemaneci, WAAD Graef, and J van Dijk. Simplifying plasma chemistry via ILDM. In *Journal of Physics: Conference Series*, volume 682, page 012035. IOP Publishing, 2016.

[65] Kim Peerenboom, Alessandro Parente, Tomáš Kozák, Annemie Bogaerts, and Gérard Degrez. Dimension reduction of non-equilibrium plasma kinetic models using principal component analysis. *Plasma Sources Science and Technology*, 24(2):025004, 2015.

[66] Christopher M Bishop. *Neural networks for pattern recognition*. Oxford university press, 1995.

[67] Jon Shlens. A tutorial on principal component analysis derivation. *Discussion and Singular Value Decomposition*, 25, 2003.

[68] Karl Pearson. Liii. on lines and planes of closest fit to systems of points in space. *The London, Edinburgh, and Dublin Philosophical Magazine and Journal of Science*, 2(11):559–572, 1901.

[69] S Pancheshnyi, B Eismann, GJM Hagelaar, and LC Pitchford. Computer code zdplaskin, university of toulouse, laplace. Technical report, CNRS-UPS-INP, Toulouse, France, 2008, http://www.zdplaskin.laplace.univ-tlse.fr, 2008.

[70] Tiago Silva, Nikolay Britun, Thomas Godfroid, and Rony Snyders. Study of CO_2 decomposition in microwave discharges by optical diagnostic methods. In *Plasma Science and Technology-Progress in Physical States and Chemical Reactions*. InTech, 2016.

[71] Alessandro Parente and James C Sutherland. Principal component analysis of turbulent combustion data: Data pre-processing and manifold sensitivity. *Combustion and flame*, 160(2):340–350, 2013.

[72] Amir Biglari and James C Sutherland. A filter-independent model identification technique for turbulent combustion modeling. *Combustion and Flame*, 159(5):1960–1970, 2012.

[73] Gints Jekabsons. ARESLab: Adaptive regression splines toolbox for Matlab/Octave. *http://www.cs.rtu.lv/jekabsons/regression.html*, Version 1.13.0, May 15, 2016.

[74] Jerome H Friedman. Multivariate adaptive regression splines. *The annals of statistics*, pages 1–67, 1991.

[75] Benjamin J Isaac, Jeremy N Thornock, James Sutherland, Philip J Smith, and Alessandro Parente. Advanced regression methods for combustion modelling using principal components. *Combustion and flame*, 162(6):2592–2601, 2015.

[76] Hessam Mirgolbabaei, Tarek Echekki, and Nejib Smaoui. A nonlinear principal component analysis approach for turbulent combustion composition space. *international journal of hydrogen energy*, 39(9):4622–4633, 2014.

[77] Hessam Mirgolbabaei and Tarek Echekki. Nonlinear reduction of combustion composition space with kernel principal component analysis. *Combustion and Flame*, 161(1):118–126, 2014.

[78] Daniel Olsson. *Applications and Implementation of Kernel Principal Component Analysis to Special Data Sets.* 2011.

[79] Bernhard Schölkopf, Alexander Smola, and Klaus-Robert Müller. Nonlinear component analysis as a kernel eigenvalue problem. *Neural computation*, 10(5):1299–1319, 1998.

[80] Quan Wang. Kernel principal component analysis and its applications in face recognition and active shape models. *arXiv preprint arXiv:1207.3538*, 2012.

[81] Md Ashad Alam and Kenji Fukumizu. Hyperparameter selection in kernel principal component analysis. 2014.

[82] Xiang Ma and Nicholas Zabaras. Kernel principal component analysis for stochastic input model generation. *Journal of Computational Physics*, 230(19):7311–7331, 2011.

[83] Jong-Min Lee, ChangKyoo Yoo, Sang Wook Choi, Peter A Vanrolleghem, and In-Beum Lee. Nonlinear process monitoring using kernel principal component analysis. *Chemical engineering science*, 59(1):223–234, 2004.

[84] James E Land. Electron scattering cross sections for momentum transfer and inelastic excitation in carbon monoxide. *Journal of Applied Physics*, 49(12):5716–5721, 1978.

[85] OJ Orient and SK Strivastava. Electron impact ionisation of H_2O, CO, CO_2 and CH_4. *Journal of Physics B: Atomic and Molecular Physics*, 20(15):3923, 1987.

[86] RK Janev, I Murakami, T Kato, and JG Wang. Cross sections and rate coefficients for electron-impact ionization of hydrocarbon molecules. Technical report, National Inst. for Fusion Science, 2001.

[87] E Krishnakumar and SK Srivastava. Cross-sections for electron impact ionization of O_2. *International journal of mass spectrometry and ion processes*, 113(1):1–12, 1992.

[88] Hirokazu Hokazono and Haruo Fujimoto. Theoretical analysis of the CO_2 molecule decomposition and contaminants yield in transversely excited atmospheric CO_2 laser discharge. *Journal of applied physics*, 62(5):1585–1594, 1987.

[89] RE Beverly. Kinetic modelling of a fast-axial-flow CO_2 laser. *Optical and Quantum Electronics*, 14(1):25–40, 1982.

[90] LE Khvorostovskaya and VA Yankovsky. Negative ions, ozone, and metastable components in dc oxygen glow discharge. *Contributions to Plasma Physics*, 31(1):71–88, 1991.

[91] IA Kossyi, A Yu Kostinsky, AA Matveyev, and VP Silakov. Kinetic scheme of the non-equilibrium discharge in nitrogen-oxygen mixtures. *Plasma Sources Science and Technology*, 1(3):207, 1992.

[92] AV Eremin, VS Ziborov, VV Shumova, D Voiki, and P Roth. Formation of O(^{1}D) atoms in thermal decomposition of CO_2. *Kinetics and catalysis*, 38(1):1–7, 1997.

[93] JA Manion, RE Huie, RD Levin, DR Burgess Jr, VL Orkin, W Tsang, WS McGivern, JW Hudgens, VD Knyazev, DB Atkinson, et al. NIST chemical kinetics database, NIST standard reference database 17, version 7.0 (web version), release 1.4. 3, data version 2008.12, national institute of standards and technology, gaithersburg, maryland, 20899-8320. *Web address: http://kinetics.nist.gov*, 2008.

[94] W Tsang and RF Hampson. Chemical kinetic data base for combustion chemistry. part i. methane and related compounds. *Journal of Physical and Chemical Reference Data*, 15(3):1087–1279, 1986.

[95] D Husain and RJ Donovan. Electronically excited halogen atoms. *Advances in Photochemistry, Volume 8*, pages 1–75, 1971.

[96] R Atkinson, DL Baulch, RA Cox, RF Hampson Jr, JA Kerr, MJ Rossi, and J Troe. Evaluated kinetic, photochemical and heterogeneous data for atmospheric chemistry: Supplement v. IUPAC subcommittee on gas kinetic data evaluation for atmospheric chemistry. *Journal of Physical and Chemical Reference Data*, 26(3):521–1011, 1997.

[97] H Hippler, R Rahn, and J Troe. Temperature and pressure dependence of ozone formation rates in the range 1–1000 bar and 90–370 k. *The Journal of chemical physics*, 93(9):6560–6569, 1990.

[98] DoL Albritton. Ion-neutral reaction-rate constants measured in flow reactors through 1977. *Atomic data and nuclear data tables*, 22(1):1–89, 1978.

[99] J Woodall, M Agúndez, AJ Markwick-Kemper, and TJ Millar. The UMIST database for astrochemistry 2006. *Astronomy & Astrophysics*, 466(3):1197–1204, 2007.

[100] AA Ionin, IV Kochetov, AP Napartovich, and NN Yuryshev. Physics and engineering of singlet delta oxygen production in low-temperature plasma. *Journal of Physics D: Applied Physics*, 40(2):R25, 2007.

[101] Baldur Eliasson. Basic data for modelling of electrical discharges in gases: oxygen. *Asea Brown Boveri Corporate Research Report*, pages KLR–86, 1986.

[102] Jay A Blauer and Gary R Nickerson. A survey of vibrational relaxation rate data for processes important to CO_2-N_2-H_2O infrared plume radiation. Technical report, ULTRASYSTEMS INC IRVINE CA, 1973.

[103] M Capitelli, C Gorse, S Longo, and D Giordano. Collision integrals of high-temperature air species. *Journal of thermophysics and heat transfer*, 14(2):259–268, 2000.

[104] Thomas G Kreutz, James A O'Neill, and George W Flynn. Diode laser absorption probe of vibration-vibration energy transfer in carbon dioxide. *Journal of Physical Chemistry*, 91(22):5540–5543, 1987.

[105] S Rahimi, M Jimenez-Diaz, S Hübner, EH Kemaneci, JJAM Van der Mullen, and J Van Dijk. A two-dimensional modelling study of a coaxial plasma waveguide. *Journal of Physics D: Applied Physics*, 47(12):125204, 2014.

Acknowledgements

First, I would like to thank Dr. Gianluigi Serianni and Prof. Ursel Fantz for the opportunity they gave me for doing this thesis in IPP-Garching. I would like to thank also Dr. Emile Carbone for introducing me into the new world of CO_2 conversion and for lots of useful comments and discussions. Moreover, I would like to thank the other members of the P4G group: Dr. Ante Hecimovic and Federico D'Isa, for supporting me and sharing their work and experiences. In general, feeling of being part of a research group in this period was really important for my personal growth in the scientific point of view. In addition, I would like to thank all people in TU Eindhoven that gave me the possibility to use PLASIMO, in particular Prof. Jan van Dijk and Dr. Diana Mihailova. A special thank goes to Stef Bardoel and Peter Koelman who patiently supported the development of nonlinear PCA and shared lots of ideas and opinions about numerical reduction techniques.

In this Erasmus experience I had also the opportunity to meet wonderful people and friends. In particular, I would like to thank Maurizio for being a real friend sharing good moments and difficulties. Moreover, a special thanks to Clara for being the exceptional person you are, sustaining me every time with your laughs and joy. I would like to mention and thank even all other friends: Maria, Deimos, Natalia and all the people who contributed to good moments during this Erasmus period. Lastly, my deepest thanks belongs to my parents. Thank you for being the calm and steady rock in my life.